Metal Ion Sensors using Tunable Resistive Pulse Sensing

by

Laura Jennifer Mayne

A Doctoral Thesis

Submitted in partial fulfilment of the requirements for

the award of Doctor of Philosophy of Loughborough

University

Acknowledgments

I could have never completed this work without the help, support, guidance and efforts from a lot of people. Firstly, thank you to my supervisors, Dr Mark Platt and Dr Steve Christie. I am extremely grateful for the opportunity to complete this work. Your support, guidance and advice over the years has been key to the success of the project.

Throughout my PhD, my friends have kept me sane and motivated. A thank you goes to my fellow Platt group, you helped me through the most stressful times and were a pleasure to work with. A very special thank you goes to Matthew Healey, having you in the lab each day provided me with so many laughs. To Lloyd Davis, Richard Wilson and Beth McMurchie, I am extremely grateful for your support and friendship. Lunch with you guys was the highlight of my day. I miss seeing you each working day and I truly believe I have made friends for life. To those friends outside Loughborough, I am grateful for the weekends of fun we have had and without each one of you, I couldn't have got through the tough times.

Finally, a huge big thank you to all my family, your continued support over the years has made this work possible. To my Mum, your love, encouragement and endless support has made completing this work possible. Thank you for all you do for me. Lastly, I dedicate this thesis to my Grandparents, Shirley Chapman and Arnie Chapman. They were not able to see me complete the work and are truly missed.

Table of Contents

List of Figures

List of Tables

List of Schemes

List of Abbreviations

APTES - (3-aminopropyl)triethoxysilane

BSA – Bovine Serum Albumin

CNCC - Carbon Nanotube Coulter Counter

CPC – Carboxylated Polystyrene Calibration (particles)

DLS – Dynamic Light Scattering

DNA – Deoxyribonucleic Acid

EDC - N-(3-Dimethylaminopropyl)-N’-ethylcarbodiimide hydrochloride

EDX - Energy Dispersive X-ray Spectroscopy

EOF - Electroosmotic Flow

FWHM – Full Width Half Maximum

HSAB - Hard Soft Acid Base Theory

ICP - OES - Inductively Coupled Plasma - Optical Emission Spectroscopy

ICR - Ionic Current Rectification

L/HMW – Low/High Molecular Weight

LbL – Layer-by-Layer

MES - 2-(N-Morpholino)ethanesulfonic acid

MSPE - Magnetic Solid Phase Extraction

NHS - N-Hydroxysulfosuccinimide

NTA – Nanoparticle Tracking Analysis

PAAMA – Poly(acrylic acid co-maleic-acid)

PALS – Phase Analysis Light Scattering

PBS – Phosphate buffered Saline

PEI – Poly(ethyleneimine)

RNA – Ribonucleic Acid

RPS – Resistive Pulse Sensing

SEM - Scanning Electron Microscopy

Si-APTES -APTES modified silica nanoparticles

SiNPs - Silica Nanoparticles

SIOS – Scanning Ion Occlusion Spectroscopy

TBA - Thrombin Binding Aptamer

TBAA - Modified Thrombin Binding Aptamer

TEM – Transmission Electron Microscopy

TPU – Thermoplastic Polyurethane

TRPS – Tunable Resistive Pulse Sensing

VEGF – Vascular Endothelial Growth Factor

VPM – Variable pressure Module

α-HL - α-Haemolysin

β-CD - β-Cyclodextrin

Abstract

There is a drive to develop rapid, portable and simple methods for detecting heavy metal ions. Due to their toxic nature, heavy metal ions are monitored in aqueous solutions such as drinking water. Standard methods for metal detection rely on instrumentation such as atomic absorption/emission and mass spectrometry. These are often costly and do not allow for rapid on-site or real-time measurements.

The aim of this PhD was to develop and optimise tunable resistive pulse sensing (TRPS) for sensing metal ions. This combines nanomaterials, dual molecular recognition with an emerging nanopore technology. TRPS is a label-free portable sensor that allows characterisation of particles based on their size, concentration and charge. Monitoring changes upon the particle surface via changes to the particle charge could be a powerful analytical tool for studying metal ion binding and new sensors. Tuning functional groups on the nanoparticle surface will allow for an array of metal ions to be detected. Nanoparticles will be modified with functional groups that bind to metal ions in solution, in turn this will change the charge on the nanoparticle which will be studied using TRPS. Particle velocity through the pore is dependent on particle charge so changes on the nanoparticle surface can be monitored.

The literature review in Chapter 1 focuses on the use of different ligands for the detection of metals focusing on aptamers and modified nanoparticles. The application of the theory of resistive pulse sensors (RPS), which is the main sensing platform within the thesis is covered in detail however these sensors to date have little use in metal ion detection. The theory behind RPS follows the literature review. This covers the theory of transport through a conical nanopore, a brief introduction to zeta potential and particle surface charge and ion current rectification.

Before developing a metal ion sensor, the translocation of a particle through the pore, focusing on its relative velocity needed to be understood. Chapter 3 demonstrates how changes in the double layer can affect the measured particle velocity. Understanding how the double layer changes with ionic strength and pH is essential in designing a metal ion sensor where the velocity of the particle through the pore is being measured. The work presented in Chapter 3 gave confidence that TRPS could be used to monitor metal ion binding to the surface of nanoparticles. The nanoparticles were modified with

a ligand (APTES) and DNA. The subsequent particle velocities differ to those of the unmodified particles, making TRPS a suitable platform for monitoring changes upon a nanoparticle surface. Building on the knowledge gained from Chapter 3, particle translocation velocities were used for the detection of copper (II) on the surface of modified nanoparticles, Chapter 4. Changes in particle velocity through the nanopore allows for detection of copper (II) as low as 1 ppm and at 10 ppm with competing metal ions present. Chapter 4 also presents the first use of studying pulse waveshape for the detection of an analyte. At low ionic strengths, particles passing through the conical pore generated a biphasic pulse containing a conductive pulse and resistive pulse. The biphasic pulse behaviour was used to monitor changes on the nanoparticle surface, and infer the presence of ions within the particles double layer. The method can be easily adapted to different analytes by altering the ligand used.

As an alternative to a particle-based assay, a pore-based assay was developed which exploited the current rectification properties of the conical pores used in TRPS. Chapter 5 presents the use of Layer-by-Layer (LbL) assembly of polyelectrolytes onto the surface of the polyurethane pore for the modification of the pore wall, a DNA aptamer was then easily immobilized onto the pore wall. Vascular Endothelial Growth Factor (VEGF) was chosen as the analyte prior to developing a metal ion assay as it was a system studied in more detail in the literature and within the group.

An advantage of TRPS is the particle-by-particle analysis. This allows for simple multiplex detection by using particles of two different sizes to detect two different analytes. In Chapter 6 the methodology and techniques from Chapter 4 is applied to the multiplexed detection of lead (II) and mercury (II) using particle translocation velocities to detect the metal ion binding to DNA aptamers. The method is applicable over a large range of ionic strengths with little interference from a high salt content. Finally, to advance the multiplexed concept, the two independent aptamer sequences used in Chapter 6 are merged together. While both aptamer halves retain their initial functionality and bind to the respective metals, the location of the binding and change in DNA structure with respect to the particles surface is the dominating factor in determining the sensitivity of the RPS technology.

1. Literature Review

1.1 Introduction

Within biological systems metal ions play key functional and structural roles.[1] The understanding of the distribution and concentrations of metal ions in biology is a central topic in bioanalytical chemistry with applications in enzyme catalysis, cell signalling and medicine development.[1] Metal ions are also an important environmental problem as, industrial activities have created large quantities of metal species through mining, discharging industrial water, corrosion, coal burning and waste dumping. These activities have led to serious environmental and health problems. Therefore, metal detection has become an important task for biological and environmental problems.[2] Standard methods for metal detection rely on instrumentation such as atomic absorption/emission and mass spectrometry. While these techniques are highly accurate and sensitive, they are costly and disallow for on-site, real-time or *in situ* measurements. To complement larger instrument analysis, a vast array of small, portable and rapid metal ion sensors has been developed. Many of these sensors incorporate fluorescent probes[3] and colorimetric probes,[4–6] many use electrochemical sensors[7–9] for the detection of the metal ions. The following section will briefly review the development of sensors for metal ions using nanoparticles and aptamers, with a focus on mercury, lead and copper. This review also covers nanopore sensors which to date have little use in metal sensors but will be the sensing platform in this thesis.

1.1.1 Nanoparticles

Nanoparticles offer a high surface area-to-volume ratio which results in high extraction capacity and high extraction efficiency, making them an ideal basis for a metal ion sensor.[10] The nanoparticles are often modified with a probe/ligand which binds to the metal ion and then generates a signal.[11–13] The use of inorganic material and specifically, functionalised nanoparticles for the extraction and detection of metal ions has been reviewed previously.[10] A wide variety of particle modifications and detection techniques have been employed. The use of fluorescent micelle nanoparticles was explored for the detection of Hg^{2+} , however the sensor was designed around a turn "off" probe which often leads to false positives.[11] Fluorescent based assays often use gold nanoparticles (AuNPs). When using a fluorescence based assay AuNPs are also more advantageous than other nanoparticles or organic quenchers because of the strong quenching capability of the AuNPs over a wide range of wavelengths.[14] This was demonstrated by Chung et al. for the detection of Hg^{2+} and Pb^{2+}.[14] AuNPs are also commonly used due to the ease of detection by the naked eye even a low metal ion concentrations.[15] AuNPs aggregating change colour and this aggregation can be induced by the binding of a metal ion is shown by Nath et al. when detecting Pb^{2+} and Cu^{2+}.[16] AuNPs are beneficial as they allow for both colorimetric and fluorometric analysis.[16,17]

Magnetic nanoparticles are often used to bind to metal due to the ease in which they can be removed from solution using a magnet.[18–20] The first use of magnetic solid phase extraction, (MSPE), was reported in 1973 for biotechnological purposes,[21] and has been used extensively since. The magnetic core is often coated with silica. The silica surface can easily be modified with a variety of ligands to become specific to a chosen metal ion such as copper or mercury.[22–24] Table 1.1 gives examples of ligands used with magnetic nanoparticles for the extraction and detection of various metal ions.

Table 1.1 *Examples of modified nanoparticles for the magnetic extraction of heavy metals. ICP-MS: Inductively coupled plasma-mass spectrometry. ICP-AES: Inductively coupled plasma-atomic emission spectrometry. ICP-OES: Inductively coupled plasma-optical emission spectrometry. AFS: Atomic fluorescence spectroscopy. FAAS: Flame atomic absorption spectrometry. AAS: Atomic absorption spectrometry.*

Ligand	Analyte	Detection Technique	Reference
Dimercaptosuccinic acid	Hg(II),Ag(II),Pb(II),Cd(II),Tl(I)	ICP-MS	[25]
Maghemite Nanoparticles	Cr(VI)	ICP-AES	[26]
Decanoic acid	Cd(II),Co(II),Cr(III),Ni(II),Pb(II),Zn(II)	ICP-OES	[27]
(3-aminopropyl) trimethoxy silane	Cu(II),Pb(II),Cd(II)	AAS	[28]
Amino-functionalised magnesium silicate	Pb(II)	ICP-AES	[29]
Phosphorus containing polymer	Pb(II),Cd(II)	FAAS	[30]
γ-mercaptopropyltrimethoxysilane	Cd(II),Cu(II),Hg(II),Pb(II)	ICP-MS	[31]
Dithiocarbamate	Hg(II)	AFS	[24]
4-bromo-3-(thiazol-2-ylimino)methylphenol	Pb(II)	FAAS	[32]
Dithizone	Pb(II), Cu(II), Cr(II)	ICP-OES	[33]

1.1.2 Aptamers

Whilst many ligands are available for metal ion binding, this thesis will use biological DNA ligands. Here is a short review on aptamer technology. Aptamers are single stranded nucleic acids (RNA and DNA). Aptamers with high affinity and high specificity have been selected against a variety of target analytes including peptides, proteins, cells, viruses and metal ions.[34–36] Recently, DNA functionalised nanomaterials have been used for the detection of these analytes.[35,36] This review will focus on the use of nanoparticles conjugated with DNA to detect metal ions. Two main class of DNA have been used to bind metal ions, aptamers and DNAzymes. DNAzymes refer to DNA-based catalyst and those which cleave RNA are commonly used in metal ion sensing.[37] In the past five years, there has been a surge in developing DNA sequences for metal ion detection, due to their high binding affinities and specificity towards metal ions.[37]

The development of metal-binding nucleic acids started in the 1990s, however they did not catch attention for the detection of metal ions until 2000, and have since been developing rapidly. Over the past two decades, many DNA sequences have been reported with high binding affinities and specificity towards metal ions.[37] Nucleic acid based sensors have been developed for a wide range of metal ions and have been covered in detailed in other reviews,[37] therefore this section of the review will focus solely on DNA sensors for mercury and lead which was a focus for work in this thesis.

Lead is a highly toxic heavy metal, causing developmental disorders in children and mental illness. Lead poisoning has been a serious concern due to historic reasons of lead in petrol, pipes and paint. Mercury, like lead, is a highly toxic heavy metal. Mercury contamination is widespread and occurs from a range of sources, and is found in many products such as paints, electronic equipment and batteries. Mercury can accumulate in the human body through the food chain and can affect the brain and nervous system, alter genetics and enzyme systems. Therefore, developing sensors for both mercury and lead has been a long standing focus in research.

1.1.2.1 Lead

G-quadruplex DNA has commonly been used for Pb^{2+} detection, Figure 1.1. The DNA folds forming two guanine quartets (G4) which binds Pb^{2+}. The strong and specific binding between Pb^{2+} and G4 structures has been recorded for a long time. Many other metals such as Na^+ and K^+ stabilise G4 DNA, but Pb^{2+} is the most effective. Usually it would require mM concentrations of K^+ and Na^+ to fold G4 DNAs, while low μM Pb^{2+} is sufficient. A single Pb^{2+} ion can fully fold the thrombin binding aptamer (TBA) into two quartets stacked over each other, whereas the same conformational change requires two K^+ ions. By exploiting this conformational change, multiple Pb^{2+} sensors have been developed. The development of lead sensors using aptamers has been reviewed previously.[38]

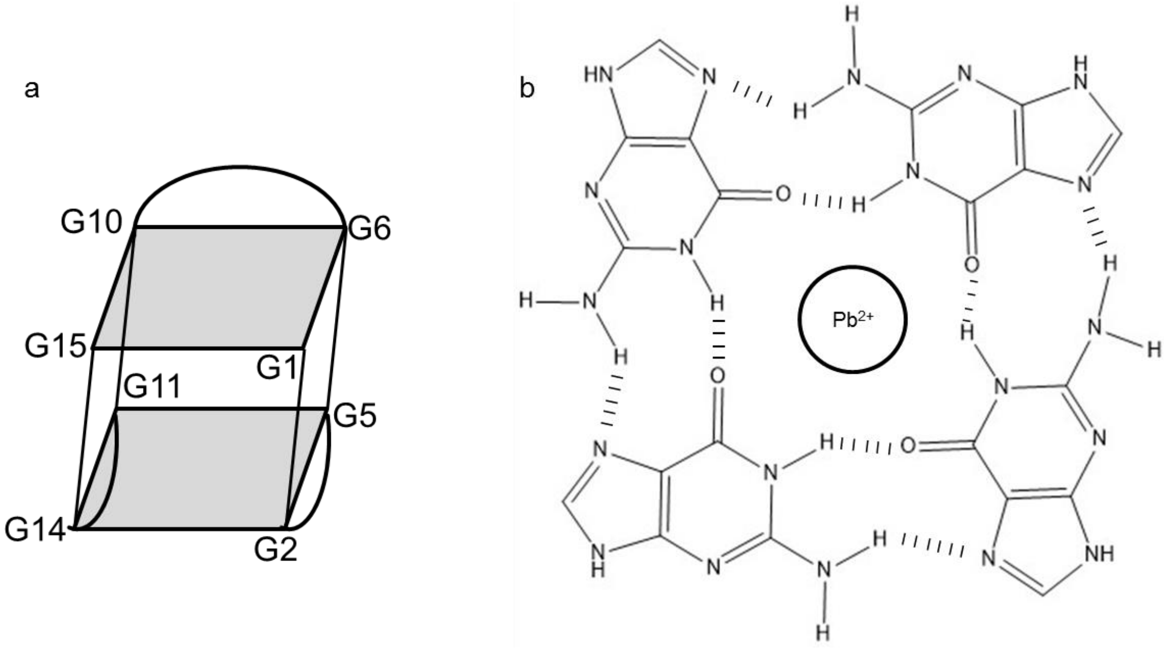

Figure 1.1 a) The folding of G4 aptamer into the G-quadruplex structure with two guanine quartets formed. b) A guanine quartet formed with Pb^{2+} bound in the centre of the two quartets.

1.1.2.2 Mercury

The reported use of DNA to sense mercury has grown considerably due to the simplicity and specificity of the thymine rich DNA binding to Hg^{2+}. The interaction was first noticed in the 1950s from UV-Vis studies.[39] A simple DNA aptamer was reported utilising the thymine-Hg^{2+}-thymine mismatch, Figure 1.2, and has been used in sensors for the detection of mercury.[40] A K_d of 1 µM Hg^{2+} towards each T-T mismatch was recorded using isothermal titration calorimetry (ITC). The simplicity of the binding has led to the development of many sensors utilizing a Hg^{2+} aptamer.[13,23–27]

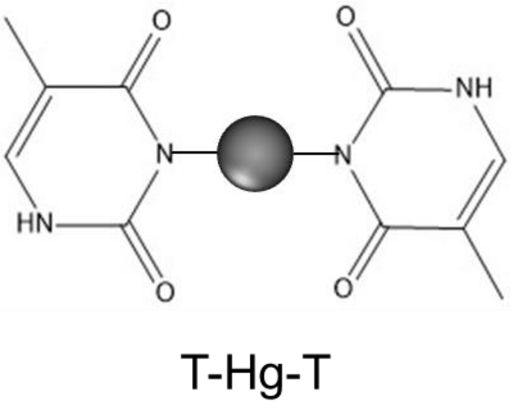

Figure 1.2 Thymine base pairs stabilised through binding with Mercury (Hg^{2+}) ions.

1.2 Particle Characterisation

Assays that are “on-bead”, i.e. those that detect analytes on a particle, require a particle characterisation technique. The aim of the PhD is to develop a rapid “on-bead” assay, where the binding does not generate a colour or redox probe, but a change in the nanoparticle properties. Commonly used techniques include scanning electron microscopy (SEM), transmission electron microscopy (TEM), nanoparticle tracking analysis (NTA) and dynamic light scattering (DLS). While each technique has it merits there are limitations associated with them. For each method the instrumentation used are often costly with low throughput. SEM/TEM do not offer *in situ* analysis of nanoparticles and require extensive preparation of samples before analysis. These techniques often measure an average over the nanoparticle population and DLS is not suitable for polydisperse samples. DLS provides an average of all the particles which are measured simultaneously. Smaller particles can be hidden behind the scattered light from larger particles, therefore the results can be biased by the presence of large particles or aggregates.

The next section will focus on a technique known collectively as resistive pulse sensing (RPS), which has been used to measure nanoparticles and biological materials.

1.3 Resistive Pulse Sensors

Resistive pulse counters have been developed and scaled down to nm dimensions over the last fifty years due to the developments in nanotechnology such as nanoscale fabrication methods. A resistive pulse sensor (RPS) is made of two fluid reservoirs which are filled with conducting electrolyte solution, the two reservoirs are connected by a small aperture or pore, Figure 1.3a. When a voltage is applied across the pore, particles and molecules can be detected in the pore by a change in resistance. [46] This is usually measured as a change in voltage or ionic current, Figure 1.3b.

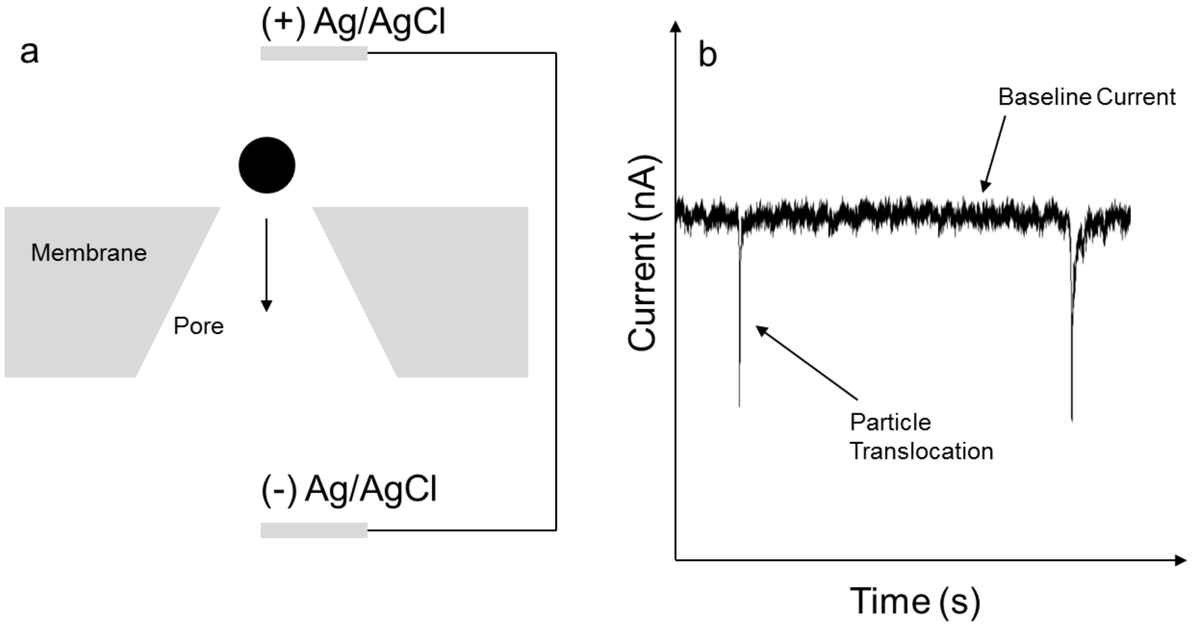

Figure 1.3 a) Schematic of a particle traversing through a nanopore, separating two fluid cells with an Ag/AgCl electrode in each. b) Current time recording of particles traversing the pore and creating blockade events.

The original RPS, the Coulter counter, had a fixed pore which was used for measuring the concentration and size of large particles.[47] Since then target analytes have become smaller thus needing smaller pores. Biological pores such as α-haemolysin (α-HL) were first used to detect differences in base pairs on single-stranded genomic DNA and RNA.[48,49] The development of solid-state nanopores was driven by the advances in nanoscale fabrication methods and thus eliminating the disadvantages that biological nanopores held.[48,50] Fabricating nanopores in various membranes allows for the size, shape and length to be controlled whereas biological nanopores can become unstable under certain parameters. To date there have been numerous synthetic nanopores reported with varying fabrication methods which include etching[50,51], ion-beam sculpting[52–54] and lithography[55]. More recently size-tunable pores have been developed; these allow the pore size to be altered which holds many advantages over pores with a fixed size.[56,57] Resistive pulse sensors have developed from particle counters to single molecule detection systems, Figure 1.4 below is a summary of what developments have occurred in the past five decades.

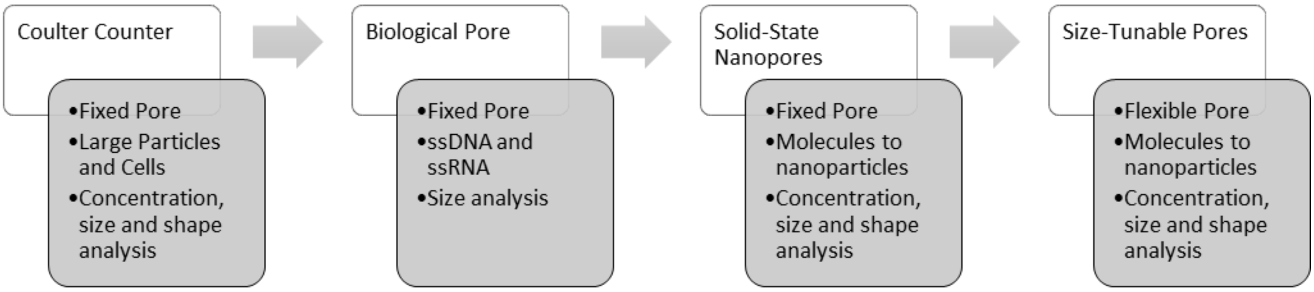

Figure 1.4 The development of resistive pulse sensors

1.3.1 The Coulter Counter

The Coulter counter is the original resistive pulse sensor, it was introduced in the 1950s by Wallace H. Coulter, and is based on passing cells through a sensing aperture.[47] The sensing aperture was used for counting and sizing red blood cells, which was usually done under a microscope, taking a substantial amount of time for each sample and results were rarely reproducible. Coulter's aperture-based resistive counter method was patented in 1953.[47] The frequency of the resistive pulses is related to the total amount of cells or particles presents in the sample and the height of the pulses is proportional to the volume of the cell or particle in the aperture.[46] Thus allowing the determination of the size of the cells in a sample and also their concentration. Coulter counters are used in hospitals today, the accuracy and speed in which cells are analysed cannot be matched by traditional methods. The Coulter counter has been refined and scaled down to nanometre dimensions over the past five decades. The target analytes have become ions, small molecules and biomolecules.[58] This section of the introduction will look closer at various nanopores, their applications and how resistive pulse sensing is being applied to detect various analytes such as viruses, DNA, RNA and proteins with a focus on metal ion sensing.

1.3.2 Biological Nanopore

Natural nanopores exist in biological cells, these are responsible for controlling ions and molecules entering and leaving the cell. Ion channels conduct ions across the cell surface, nuclear membrane pores control the passage of messenger-RNA (mRNA) and proteins are secreted across membranes of cell organelles.[59] In the early 1990s it was suggested that nanopores could be used as sensors for DNA,[49] with the first experimental results being published in 1996 using the biological pore α-haemolysin (α-HL).[48,49] α-HL is a protein secreted by *Staphylococcus aurues.* The protein self-assembles in lipid membranes to form a channel inside of a mushroom-shaped homo-oligomeric heptamer.[48,60] The channel is 100 Å in length and runs along the sevenfold axis. At a neutral pH the channel remains open and α-HL passes a steady current of 100 pA with an applied voltage of 100 mV. The opening of the channel measures 2.6 nm with an internal pore diameter of 2.2 nm.[60] The size of the diameter allows single-stranded DNA and RNA, but not double-stranded DNA and RNA, to translocate through the pore.

Initial experiments were focused on the sequencing of DNA.[48,49] The electric field can drive a single nucleic acid molecule through the pore in a linear sequence, which creates a distinctive electrical signal. When a molecule enters the pore, the ionic current is reduced because part of the liquid that carries the current is being occupied by a molecule such as DNA. This allows the length of a DNA or RNA molecule to be measured.[61] The length is measured by the speed in which the strand travels through the pore, as the strand decreases in length the velocity increases. The duration of the pulse is relative to the velocity of a molecule.[61] The basis of being able to sequence a strand of DNA depends on the individual bases producing a unique signal as it passes through the pore. Initial experiments were promising, and produced interesting results which highlighted the properties of the molecules being passed through the channels.[49] These initial experiments determined the speed in which DNA and RNA translocate, indicating the chain length altered dynamics.[62] It was also found that the blockades by homopolymers of polycytidylic acid (Poly C), polyadenylic acid (Poly A) and polyuridylic acid (Poly U) can be distinguished from one another based on the blockade kinetics.[61] However, even though these initial experiments showed promising results, single-base resolution has not been achieved by simple DNA translocation through the α-HL channel.

Biological nanopores have a great advantage in that they can be engineered to alter the channel allowing for modifications for sensing analytes. Through mutagenesis of a channel it is possible to make well defined changes to the structure such as the incorporation of amino acids,[46] and adding organic molecules at a specific site.[63] α-HL has several features which make it suitable for engineering; the protein is robust, it can be obtained in abundance from bacteria,[46] the channel remains open and has a high conductance[48]. Thus a variety of stochastic sensors have been developed around chemically engineered α- HL channels which have involved fitting the channel with a chiral adapter β-cyclodextrin[63] (β-CD). The β-CD which is bound to the inside of the channel produces a cavity for binding various organic molecules.[63,64] The β-CD alters the selectivity and magnitude of ion conduction in the membrane potential.[60] Engineering the α-HL channel leads the way in improving the channels discrimination among organic molecules, metal ions[65] and nucleotides.

Due to their biological components, these pores have a limited pH and ionic strength operating range. Biological nanopores have fixed size and can become unstable under certain parameters such as changes of temperature.[59] The disadvantages of biological pores have led the way for solid-state nanopores to be fabricated. As more analytes are being targeted for detection, the fabrication of solid-state nanopores allows control during the process to specifically design a pore for a particular analyte. To design a pore the fabrication process can allow control over the size and channel length of the pore.

1.3.3 Solid State Nanopores

Solid-state nanopores exhibit many advantages over biological nanopores. They are very stable and during fabrication the diameter and channel length can be controlled, unlike biological nanopores. This section will review the methods of fabricating solid-state nanopores and their applications.

1.3.3.1 Fabrication of Solid State Nanopores

There have been many different approaches to fabricating nanopores in membranes including etching[50,51], ion beam sculpting[52–54] and lithography[55]. Each method can create pores with nanometre dimensions.

Etching a hole into an insulating layer can create a pore. A track etching technique can be used, this technique is based on the irradiation of the substrate material followed by chemical etching.[51] The technique uses a high-energy single ion to create an etchable track which can then guide the subsequent chemical etching. The current is measured across the membrane during etching so provides a feedback mechanism for when the etching should be stopped, this enables nanopores to be created.[51]

Ion-beam sculpting techniques uses low-energy ion beams, whereas etching uses high-energy ion beams. This technique removes atoms from the surface of the insulating membrane in a process called sputtering.[53] Often the materials being worked with are SiN and SiO_2 because they hold the advantage that they have been well-developed[66] and are commonly used in electronic devices.[52,54] The ion beam sculpting process involves material being removed from the surface which contains a cavity on the opposite surface, eventually the flat surface will intercept the cavity creating a nanopore. Creating a nanopore requires the knowledge of when to stop the erosion process; the apparatus used usually has a feedback system to ensure the erosion process stops at the correct time.[53,54] However, at room temperature, the low-energy ion beam can cause the pore to shrink so temperature, ion beam duty cycle and the ion beam flux need to be controlled.[53] The phenomenon of pores shrinking was taken advantage of and initial pores were created in the membrane using a focused ion beam (FIB) machine. Ion beam sculpting then closes the pore, like the initial ion beam sculpting method[53,54], the ion beam apparatus has feedback control. It was recorded that at low temperatures the removal of material by the sputtering process outweighs pore formation, thus using a technique known as cold ion beam sculpting removes the need for an initial pore.[52] The main problem with the ion beam sculpting technique is that the material consistency and internal geometry of the pore are hard to control.[52]

Another technique uses electron beam lithography with subsequent etching to create a pore. After thermal oxidation of an initial pore the pore size can then be reduced when exposed to a high-energy electron beam.[55] A commercial transmission electron microscope (TEM) is used to fine-tune the pore size with nanometre precision. The changes in the pore can be monitored through the microscope and the process can be stopped within seconds.[55] The advantage of this method is that modifications are possible with direct visual feedback from the microscope.

Using the resistive pulse method with solid-state nanopores makes it possible to study and analyse various analytes such as individual proteins, protein-protein interactions such as antibody-antigen complexes, DNA and viruses.[67] Two of the researched analytes are DNA and protein[26,27] molecules which will be discussed further in the next section.

1.3.4 Applications of Solid State Nanopores

The prospect of being able to eventually sequence DNA using solid-state nanopores has opened the doors for various research into other molecules such as proteins and viruses.[67-69] These applications have allowed protein concentrations to be measured quickly and accurately without the need for labels like in traditional immunoassays and to investigate protein-protein interactions.[68] This section will look further into the applications of resistive pulse sensing with solid-state nanopores.

1.3.4.1 Proteins

The properties and interactions of proteins in solution can be analysed using resistive pulse sensing with synthetic nanopores. The interactions with the pore as the protein passes through can be used to measure protein concentration accurately.[67] The first label-free assays investigated compared advantageously to classic immunoassays. [67] There was no need to label or immobilize the analyte, the instrumental set up is simple and allows real-time detection of the analyte. It it was determined that individual proteins could be detected using nanopores, protein-protein interactions were investigated.[67,68] The antigen-antibody complex such as anti-BSA-Fab is larger than the original analyte, in this case bovine serum albumin (BSA), and thus longer duration pulses are observed.[68] Because of the longer duration pulses, it was assumed that when a protein passes through a nanopore it engages in adsorption/desorption to and from the nanopore wall as it translocates through the detection system.[70] A disadvantage of the initial experiments found that the label-free antibody-antigen complexes moved through the pore too quickly to be detected unless at low pH,[67] which then disrupted the antibody-antigen interactions.

1.3.4.2 DNA

DNA has been investigated thoroughly with promising outcomes in quantifying DNA and slowing DNA translocation for sequencing. Like biological nanopores, solid-state nanopores are being used in the hope of being able to sequence DNA at low-cost and high-throughput.[69] Solid-state nanopores have also been applied to measure DNA hybridisation,[70] folding[71] and length.[72,73]

The main problem with sequencing DNA is that the strands move too quickly through the nanopore when being driven by an electric filed. Various methods have been explored to slow down the translocation of the DNA molecule. The DNA molecule can be driven through the pore using magnetic tweezers[74] or optical tweezers.[75] However, using tweezers can make the translocation too slow, which in practice would make it difficult to scale up the experiment in order to sequence DNA.[69] Another method has been to use a viscous solvent such as aqueous glycerol which has been shown experimentally to slow down the velocity of translocation by a factor of 5.5.[69,76] Increasing ion concentration and decreasing temperature also slow down the translocation velocity by increasing the friction coefficient of DNA in an electrolyte which can increase the resolution.[76,77]

Solid-state nanopores have been used to determine the length of DNA fragments; this leads the way for quantitative techniques using nanopores.[72] Fragments of double-stranded DNA with sizes ranging from 6.5 kbp to 24 kbp were separated by length, the longer the DNA strand, the longer the translocation time.[72] However compared with the gel electrophoresis the resolving power did not meet the same standards. It is also possible to determine if the DNA is single-stranded or double-stranded due to a difference in blockade currents.[78] It has been suggested to gain higher resolution the DNA needs to translocate at a slower speed,[77] changing the parameters to do so are mentioned above.

Proteins and DNA can also be analysed together.[77] Proteins are constantly binding to DNA in events to replicate genetic information. Examples of DNA-binding proteins include transcription factors and nucleases.[77] The ability to study proteins binding to DNA strands is important in genetic screening. The changes in ionic current can be used to distinguish protein covered patches along the DNA strand. RecA protein was used as a DNA-binding protein, RecA-dsDNA complexes are known to be very stable making them suitable for analysis.[77] The blockade for RecA-dsDNA was found to be 12 times larger than ordinary dsDNA, thus making it possible to distinguish between the two.

The capabilities of solid-state nanopores to analysis DNA is providing promising results for future high-speed, high resolution, low cost and direct read out of genetic information. This includes DNA sequencing and the ability to quantify DNA by distinguishing chain length.[69,72,73] The ability to slow down the DNA translocation speed to achieve single base pair resolution is an important factor in achieving the desired outcome.

1.3.5 Carbon Nanotubes

Carbon nanotube-based coulter counters (CNCCs) provide a way to measure concentration, size and surface charge of nanoparticles.[79] Using CNCCs eliminates the need for standards, calibrations or labelling.[73,79] CNCCs are based on multiwall carbon nanotube (MWNT) channels which range in diameter from 130-150 nm used to determine the size of nanoparticles ranging from 28-100 nm.[79] MWNTs have material properties which are desirable to the analysis of nanoparticles. The varying diameters on the channels are available commercially and the size range is suitable for a wide variety of analytes. Also, the channel diameters are precise, uniform and stable,[38] which makes carbon nanotubes suitable for accurate particle sizing. The signal height and width measurements allow determination of size and electrophoretic mobility, respectively. These measurements do not require a calibration and remove the need to label the analyte. Particle sizes calculated from the current pulse height were comparable to those measurements gained from TEM.[80,81] However, CNCCs are limited to particle range (28-100 nm) and often require a high concentration of electrolyte solution. The main disadvantage is that the nanotube could become blocked by aggregates which would reduce the lifetime of a CNCC to a couple of hours.[79]

The ability to determine size, concentration and surface charge without the need for calibration or labelling makes CNCCs favourable over traditional analytical techniques such as DLS, TEM and phase analysis light scattering (PALS).[73] In addition to sizing nanoparticles, efforts are being directed towards detecting and characterising biological materials such as viruses, proteins and DNA.[71]

1.3.6 Tunable Resistive Pulse Sensing

The ability to tune the pore size to the analyte of interest has allowed the RPS technique to detect analytes that range from the molecule, DNA, proteins, cellular vesicles and viruses to whole cells, and again detailed reviews on the types of analytes and applications can be found elsewhere.[82,83] One property that all solid state and biological pores share is the fixed nature of the pore size. Once prepared and assembled the pore size cannot be changed.

An elegant and novel adaptation to RPS was to use a tunable elastomeric pore, which allows for further versatility as the pore can be stretched in real time to suit the sample.

The pores used in TRPS are manufactured in thermoplastic polyurethane membranes, the process has been described in detail previously.[57] Briefly, the tunable pores are fabricated by mechanically puncturing a ~0.25 mm thick thermoplastic polyurethane membrane with a polycrystalline tungsten rod.[57,84-86] The pore is conical in shape which can then be stretched in a controlled bi-axial, reversible manner to change the pore geometry. The fluid cell incorporates electrodes which are used to apply an electric field and to monitor the current through the membrane. The membranes can be stretched and relaxed multiple times making the pores suitable to be used over several experiments. The pore shape was found not to deviate significantly upon stretching.[57,84] Experiments carried out on the fabricated the pores were carried out at higher stretches than would be performed in an experimental set up within this thesis.[57] The technique is currently referred to as Tunable Resistive Pulse Sensing, (TRPS) but its name evolved from that of Scanning Ion Occlusion Spectroscopy, SIOS,[85] and still variants such as size-tunable pore sensors, or tunable elastomeric pore sensors are found in the literature. TRPS have been developed to accurately determine the concentration, size and surface charge of dispersed inorganic particles and biological analytes.[56,86-90]

TRPS is much more versatile than solid state pore equivalents, but there are limitations to how much each pore can be stretches, thus users typically match a membrane to the sample of interest. Passing complex biological samples through a small aperture often leads to blockages, and if the blockage is not removed the pore is unable to perform any further analysis. Along with its versatility to change the pore size to match the analyte, the tunable pore also allows the user to pause experiments if a blockage occurs, stretch and open the pore dislodging the trapped analyte, and then reduce the pore size and carry on the data capture. The company Izon supplies tunable pores in a range of sizes, Table 1.2. Each pore has the ability to measure a range of particle sizes and Table 1,2 can help the user choose a pore depending on the particle size.The ability to match a pore to a specific sample, and the fact they are relatively inexpensive has enabled laboratories from different disciplines a chance to develop methods of analysis using RPS without the worry of synthesising/ breaking or blocking the pores.

Table 1.2 Description of analysis size ranges of each nanopore ID supplied by Izon Science Ltd.

Nanopore	Analysis Size Range (nm)
NP80	40-255
NP100	50-330
NP150	70-420
NP200	85-500
NP250	110-630
NP300	150-900
NP400	185-1100
NP600	270-1570
NP800	385-2050
NP1000	490-2900
NP2000	935-5700
NP4000	1990-11300

1.3.7 Metal Ion Detection

Nanopores are commonly used as methods for characterising biological material such as DNA, proteins and viruses. This section of the review will focus on the limited work carried out on metal ion detection using nanopores. Modification of nanopores is a common approach when detecting analytes such as proteins and has been used for metal ions, summarised in Table 1.3. The binding of the metal ion to the surface of the pore, results in a change of ion flow through the pore and the resulting current-voltage curve is recorded.[45,91,94] The process of modifying the pore interior is often lengthy and time consuming.[45]

Metal ion sensing with the α-hemolysin pore has been realised by mutating the protein to construct binding sites in the lumen of α-HL. Choi *et al*. used a mutant α-HL pore with four cysteine mutations to detect Ag^+ and Cd^{2+}.[92] An engineered pore containing histidine residues was used for the detection of Zn^{2+}, Co^{2+} and Cd^{2+} by Braha *et al*.[64] Polyamine decorated cyclodextrins were used as a recognition element in a α-HL pore for the detection of Cu^{2+} with no need to mutate the proteins to construct binding sites.[65] However, it is difficult to modifying the pore's interior due to the complexity of mutagenesis and separation of the protein nanopore. Often strong background disturbances exist that limit the sensitivity when detecting metal ions via protein pores.

Table 1.3 Summary of modified nanopores for metal ion sensing.

Pore Type	Metal Ion	Mechanism	Ref.
α-HL	Ag^+ & Cd^{2+}	Stochastic Sensing	[92]
α-HL	Zn^{2+}, Co^{2+} & Cd^{2+}	Stochastic Sensing	[64]
α-HL	Cu^{2+}	Stochastic Sensing	[65,93]
Glass nanopore	Hg^{2+}	Ionic Current Rectification	[94]
Alumina nanochannels	Hg^{2+} & Ag^{2+}	Ionic Current Rectification	[45]
Carbon Nanotubes	Hg^{2+}	Ionic Current Rectification	[95]

1.4 Summary

Onsite analysis requires a portable, easy to use platform which offers rapid and sensitive metal ion sensing. The work presented in this thesis attempts to deisgn and fabricate sensors for metal ions such as copper, mercury and lead by combining nanoparticles, TRPS and aptamers. Nanoparticles are becoming a powerful tool in analytical chemistry and are used to bind metal ions in solution. Aptamers are short stranded oligonucleotide sequences which have been used to bind metal ions with high affinity and specificity. RPS technologies have currently been used for the measurement of inorganic and biological material. The work in the thesis combines these three topics to develop metal ion sensors by binding ligands to nanoparticles and using a pore-based technique to monitor changes on the particles surface.

In this work, nanoparticles will have ligands attached to their surfaces. These ligands will bind to metal ions in solution and here we study copper (II), lead (II) and mercury (II). The hypothesis is that TRPS will be used to characterise the nanoparticles before and after modification and differences in particle mobility will be detected. The metal binding to the chosen ligand will lead to change in charge on the nanoparticles surface and this will change the particles mobility through the pore. Different ionic strengths and pH will be used throughout the thesis to determine the best electrolyte for the detection of the metal ion.

Alongside the particle-based assay, a pore-based assay will be developed. Pores used in TRPS exhibit rectification behaviour. Modification of the pore will allow DNA aptamers to be immobilised on the pore wall and a change in current will be recorded when the analyte binds. While each assay has the same aims, differences and benefits of each assay will be explored within this thesis.

1.5 References

1. Yannone, S. M., Hartung, S., Menon, A. L., Adams, M. W. W. & Tainer, J. A. Metals in biology: Defining metalloproteomes. *Curr. Opin. Biotechnol.* **23,** 89–95 (2012).

2. Järup, L. Hazards of heavy metal contamination. *British Medical Bulletin* **68,** 167–182 (2003).

3. Liu, S., Zhang, L. & Liu, X. A highly sensitive and selective fluorescent probe for Fe^{3+} based on 2- (2- hydroxyphenyl) benzothiazole. *RSC Adv.* **6,** 100696–100699 (2013).

4. Jang, H. J., Jo, T. G. & Kim, C. A single colorimetric sensor for multiple targets: the sequential detection of Co^{2+} and cyanide and the selective detection of Cu^{2+} in aqueous solution. *RSC Adv.* **7,** 17650–17659 (2017).

5. Wang, Y. *et al.* Colorimetric probe for copper(II) ion detection based on cost-effective aminoquinoline derivative. *Anal. Methods* **9,** 1727–1731 (2017).

6. Lin, Q. *et al.* A novel water soluble chemosensor based on carboxyl functionalized NDI derivatives for selective detection and facile removal of mercury(II). *RSC Adv.* **7,** 11206–11210 (2017).

7. Cui, L., Wu, J. & Ju, H. Electrochemical sensing of heavy metal ions with inorganic, organic and bio-materials. *Biosens. Bioelectron.* **63,** 276–286 (2015).

8. Yang, L. *et al.* An electrochemical sensor for highly sensitive detection of copper ions based on a new molecular probe Pi-A decorated on graphene. *Anal. Methods* **9,** 618–624 (2017).

9. Kumar, S., Mittal, S. K., Singh, J. & Kaur, N. MWCNT incorporated imine–amine ionophore for electrochemical sensing of copper ions. *Anal. Methods* **8,** 7472–7481 (2016).

10. Ray, P. Z. & Shipley, H. J. Inorganic nano-adsorbents for the removal of heavy metals and arsenic: a review. *RSC Adv.* **5,** 29885–29907 (2015).

11. Nie, K., Dong, B., Shi, H., Liu, Z. & Liang, B. Diketopyrrolopyrrole Amphiphile-Based Micelle-Like Fluorescent Nanoparticles for Selective and Sensitive Detection of Mercury(II) Ions in Water. *Anal. Chem.* **89,** 2928–2936 (2017).

12. Chen, G. *et al.* Gold nanoparticles and the corresponding filter membrane as chemosensors and adsorbents for dual signal amplification detection and fast removal of mercury(II). *Nanoscale* **9,** 3315–3321 (2017).

13. Liu, C. W., Huang, C. C. & Chang, H. T. Control over surface DNA density on gold nanoparticles allows selective and sensitive detection of mercury(II). *Langmuir* **24,** 8346–8350 (2008).

14. Chung, C. H., Kim, J. H., Jung, J. & Chung, B. H. Nuclease-resistant DNA aptamer on gold nanoparticles for the simultaneous detection of Pb^{2+} and Hg^{2+} in human serum. *Biosens. Bioelectron.* **41,** 827–832 (2013).

15. Zhang, M., Liu, Y.-Q. & Ye, B.-C. Colorimetric assay for parallel detection of Cd^{2+}, Ni^{2+} and Co^{2+} using peptide-modified gold nanoparticles. *Analyst* **137,** 601–7 (2012).

16. Nath, P., Arun, R. K. & Chanda, N. Smart gold nanosensor for easy sensing of lead and copper ions in solution and using paper strips. *RSC Adv.* **5,** 69024–69031 (2015).

17. Ye, Y., Lv, M., Zhang, X. & Zhang, Y. Colorimetric determination of copper(II) ions using gold nanoparticles as a probe. *RSC Adv.* **5,** 102311–102317 (2015).

18. Zhai, Y., He, Q., Han, Q. & Duan, S. Solid-phase extraction of trace metal ions with magnetic nanoparticles modified with 2,6-diaminopyridine. *Microchim. Acta* **178,** 405–412 (2012).

19. Yan, P., He, M., Chen, B. & Hu, B. Restricted accessed nanoparticles for direct magnetic solid phase extraction of trace metal ions from human fluids followed by inductively coupled plasma mass spectrometry detection. *Analyst* **140,** 4298–4306 (2015).

20. Babazadeh, M., Hosseinzadeh-Khanmiri, R., Abolhasani, J., Ghorbani-Kalhor, E. & Hassanpour, A. Solid phase extraction of heavy metal ions from agricultural samples with the aid of a novel functionalized magnetic metal–organic framework. *RSC Adv.* **5,** 19884–19892 (2015).

21. Robinson, P., Dunnill, P. & Lilly, M. The properties of magnetic supports in relation to immobilized enzyme reactors. *Biotechnol. Bioeng.* **XV,** 603–606

(1973).

22. Ren, C. *et al.* Core–shell superparamagnetic monodisperse nanospheres based on amino-functionalized $CoFe_2O_4@SiO_2$ for removal of heavy metals from aqueous solutions. *RSC Adv.* **7,** 6911–6921 (2017).

23. Li, Y. *et al.* Preconcentration of ultra-trace Cu(II) and Cd(II) using SPE based on an alizarin complexone modified silica gel with detection using FAAS and determination of ultra-trace Cu(II) by the naked eye. *Anal. Methods* **7,** 3876–3882 (2015).

24. Girginova, P. I. *et al.* Silica coated magnetite particles for magnetic removal of Hg2+ from water. *J. Colloid Interface Sci.* **345,** 234–40 (2010).

25. Yantasee, W. *et al.* Removal of Heavy Metals from Aqueous Systems with Thiol Functionalized Superparamagnetic Nanoparticles. *Environ. Sci. Technol.* **41,** 5114–5119 (2007).

26. Hu, J., Chen, G. & Lo, I. M. C. Removal and recovery of Cr(VI) from wastewater by maghemite nanoparticles. *Water Res.* **39,** 4528–4536 (2005).

27. Faraji, M. *et al.* A nanoparticle-based solid-phase extraction procedure followed by flow injection inductively coupled plasma-optical emission spectrometry to determine some heavy metal ions in water samples. *Anal. Chim. Acta* **659,** 172–177 (2010).

28. Wang, J. *et al.* Amino-functionalized $Fe_3O_4@SiO_2$ core-shell magnetic nanomaterial as a novel adsorbent for aqueous heavy metals removal. *J. Colloid Interface Sci.* **349,** 293–299 (2010).

29. Zou, B., Chen, K., Wang, Y., Niu, C. & Zhou, S. Amino-functionalized magnetic magnesium silicate double-shelled hollow microspheres for enhanced removal of lead ions. *RSC Adv.* **5,** 22973–22979 (2015).

30. Yilmaz, E., Alosmanov, R. M. & Soylak, M. Magnetic solid phase extraction of lead(II) and cadmium(II) on a magnetic phosphorus-containing polymer (M-PhCP) for their microsampling flame atomic absorption spectrometric determinations. *RSC Adv.* **5,** 33801–33808 (2015).

31. Huang, C. & Hu, B. Silica-coated magnetic nanoparticles modified with γ-

mercaptopropyltrimethoxysilane for fast and selective solid phase extraction of trace amounts of Cd, Cu, Hg, and Pb in environmental and biological samples prior to their determination by inductively co. *Spectrochim. Acta - Part B At. Spectrosc.* **63,** 437–444 (2008).

32. Bayat, M., Shemirani, F. & Beyki, M. H. Utilization of facile synthesized Fe3O4 nanoparticles as a selective support for preconcentration of lead ions from food and environmental samples. *Anal. Methods* **6,** 5345 (2014).

33. Zhang, L. *et al.* Preparation of dithizone grafted poly(allyl chloride) core–shell–shell magnetic composite microspheres for solid-phase extraction of ultra-trace levels of Pb(II), Cu(II) and Cr(III) ions. *RSC Adv.* **5,** 58873–58879 (2015).

34. Cho, E. J., Lee, J.-W. & Ellington, A. D. Applications of Aptamers as Sensors. *Annu. Rev. Anal. Chem.* **2,** 241–264 (2009).

35. Chiu, T. C. & Huang, C. C. Aptamer-functionalized nano-biosensors. *Sensors* **9,** 10356-10388 (2009).

36. Samanta, A. & Medintz, I. L. Nanoparticles and DNA - a powerful and growing functional combination in bionanotechnology. *Nanoscale* **8**, 9037–9095 (2016).

37. Zhou, W., Saran, R. & Liu, J. Metal Sensing by DNA. *Chem. Rev.* **117**, 8272−8325 (2017).

38. Yang, D. *et al.* Aptamer-based biosensors for detection of lead(ii) ion: a review. *Anal. Methods* **9,** 1976–1990 (2017).

39. Katz, S. The Reversible Reaction of Sodium Thymonucleate and Mercuric Chloride. *J. Am. Chem. Soc.* **74,** 2238–2245 (1952).

40. Ono, A. & Togashi, H. Highly selective oligonucleotide-based sensor for mercury(II) in aqueous solutions. *Angew. Chemie - Int. Ed.* **43,** 4300–4302 (2004).

41. Cai, S., Lao, K., Lau, C. & Lu, J. "Turn-On” Chemiluminescence Sensor for the Highly Selective and Ultrasensitive Detection of Hg^{2+} Ions Based on Interstrand Cooperative Coordination and Catalytic Formation of Gold Nanoparticles. *Anal. Chem.* **83,** 9702–9708 (2011).

42. Torigoe, H., Ono, A. & Kozasa, T. HgII ion specifically binds with T:T mismatched base pair in duplex DNA. *Chem. - A Eur. J.* **16,** 13218–13225 (2010).

43. Liu, C. W., Hsieh, Y. T., Huang, C. C., Lin, Z. H. & Chang, H. T. Detection of mercury(II) based on Hg^{2+} -DNA complexes inducing the aggregation of gold nanoparticles. *Chem Commun* 2242–2244 (2008). doi:10.1039/b719856f

44. Zhang, W. *et al.* A photoelectrochemical DNA sensor for the detection of Hg $^{2+}$ based on Hg^{2+} -mediated oligonucleotide switching. *Anal. Methods* **8,** 7762–7766 (2016).

45. Wang, H. *et al.* Dual-response for Hg^{2+} and Ag^{+} ions based on biomimetic funnel-shaped alumina nanochannels. *J. Mater. Chem. B* **3,** 1699–1705 (2015).

46. Bayley, H. & Martin, C. R. Resistive-pulse sensing - from microbes to molecules. *Chem. Rev.* **100,** 2575–2594 (2000).

47. Graham, M. D. The Coulter Principle: Foundation of an industry. *JALA - J. Assoc. Lab. Autom.* **8,** 72–81 (2003).

48. Deamer, D. W. & Akeson, M. Nanopores and nucleic acids: Prospects for ultrarapid sequencing. *Trends Biotechnol.* **18,** 147–151 (2000).

49. Kasianowicz, J. J., Brandin, E., Branton, D. & Deamer, D. W. Characterization of individual polynucleotide molecules using a membrane channel. *Proc. Natl. Acad. Sci.* **93,** 13770–13773 (1996).

50. Fertig, N., Blick, R. H. & Behrends, J. C. Whole Cell Patch Clamp Recording Performed on a Planar Glass Chip. *Biophys. J.* **82,** 3056–3062 (2002).

51. Siwy, Z. & Fuliński, A. Fabrication of a Synthetic Nanopore Ion Pump. *Phys. Rev. Lett.* **89,** 198103 (2002).

52. Kuan, A. T. & Golovchenko, J. A. Nanometer-thin solid-state nanopores by cold ion beam sculpting. *Appl. Phys. Lett.* **100,** 1–5 (2012).

53. Li, J. *et al.* Ion-beam sculpting at nanometre length scales. *Nature* **412,** 166–169 (2001).

54. Hoogerheide, D. P., George, H. B., Golovchenko, J. A. & Aziz, M. J. Thermal

activation and saturation of ion beam sculpting. *J. Appl. Phys.* **109,** 1–4 (2011).

55. Storm, A. J., Chen, J. H., Ling, X. S., Zandbergen, H. W. & Dekker, C. Fabrication of solid-state nanopores with single-nanometre precision. *Nat. Mater.* **2,** 537–540 (2003).

56. Roberts, G. S. *et al.* Tunable pores for measuring concentrations of synthetic and biological nanoparticle dispersions. *Biosens. Bioelectron.* **31,** 17–25 (2012).

57. Sowerby, S. J., Broom, M. F. & Petersen, G. B. Dynamically resizable nanometre-scale apertures for molecular sensing. *Sensors Actuators, B Chem.* **123,** 325–330 (2007).

58. Willmott, G. R., Platt, M. & Lee, G. U. Resistive pulse sensing of magnetic beads and supraparticle structures using tunable pores. *Biomicrofluidics* **6,** 1–15 (2012).

59. Dekker, C. Solid-state nanopores. *Nat. Nanotechnol.* **2,** 209–215 (2007).

60. Song, L. *et al.* Structure of staphylococcal alpha-hemolysin, a heptameric transmembrane pore. *Science (80-.).* **274,** 1859–1866. (1996).

61. Akeson, M., Branton, D., Kasianowicz, J. J., Brandin, E. & Deamer, D. W. Microsecond Time-Scale Discrimination Among Polycytidylic Acid, Polyadenylic Acid, and Polyuridylic Acid as Homopolymers or as Segments Within Single RNA Molecules. *Biophys. J.* **77,** 3227–3233 (1999).

62. Meller, A., Nivon, L. & Branton, D. Voltage-driven DNA translocations through a nanopore. *Phys. Rev. Lett.* **86,** 3435–3438 (2001).

63. Gu, L. Q., Braha, O., Conlan, S., Cheley, S. & Bayley, H. Stochastic sensing of organic analytes by a pore-forming protein containing a molecular adapter. *Nature* **398,** 686–690 (1999).

64. Braha, O. *et al.* Simultaneous stochastic sensing of divalent metal ions. *Nat. Biotechnol.* **18,** 1005–1007 (2000).

65. Guo, Y., Jian, F. & Kang, X. Nanopore sensor for copper ion detection using a polyamine decorated β-cyclodextrin as the recognition element. *RSC Adv.* **7,** 15315–15320 (2017).

66. Willmott, G. R., Platt, M. & Lee, G. U. Resistive pulse sensing of magnetic beads and supraparticle structures using tunable pores. *Biomicrofluidics* **6,** 014103-014115 (2012).

67. Han, A. *et al.* Label-free detection of single protein molecules and protein−protein interactions using synthetic nanopores. *Anal. Chem.* **80,** 4651–4658 (2008).

68. Sexton, L. T. *et al.* Resistive-pulse studies of proteins and protein/antibody complexes using a conical nanotube sensor. *J. Am. Chem. Soc.* **129,** 13144–13152 (2007).

69. Luan, B., Stolovitzky, G. & Martyna, G. Slowing and controlling the translocation of DNA in a solid-state nanopore. *Nanoscale* **4,** 1068–1077 (2012).

70. Sexton, L. T. *et al.* An adsorption-based model for pulse duration in resistive-pulse protein sensing. *J. Am. Chem. Soc.* **132,** 6755–6763 (2010).

71. Steinbock, L. J., Otto, O., Chimerel, C., Gornall, J. & Keyser, U. F. Detecting DNA folding with nanocapillaries. *Nano Lett.* **10,** 2493–2497 (2010).

72. Storm, A. J., Chen, J. H., Zandbergen, H. W. & Dekker, C. Translocation of double-strand DNA through a silicon oxide nanopore. *Phys. Rev. E - Stat. Nonlinear, Soft Matter Phys.* **71,** 1–10 (2005).

73. Storm, A. J. *et al.* Fast DNA translocation through a solid-state nanopore. *Nano Lett.* **5,** 1193–1197 (2005).

74. Peng, H. & Ling, X. S. Reverse DNA translocation through a solid-state nanopore by magnetic tweezers. *Nanotechnology* **20,** 185101 (2009).

75. Keyser, U. F., Van Der Does, J., Dekker, C. & Dekker, N. H. Optical tweezers for force measurements on DNA in nanopores. *Rev. Sci. Instrum.* **77,** 105105 (2006).

76. Fologea, D., Uplinger, J., Thomas, B., McNabb, D. S. & Li, J. Slowing DNA translocation in a solid-state nanopore. *Nano Lett.* **5,** 1734–1737 (2005).

77. Kowalczyk, S. W., Hall, A. R. & Dekker, C. Detection of local protein structures along DNA using solid-state nanopores. *Nano Lett.* **10,** 324–328 (2010).

78. Skinner, G. M. *et al.* Distinguishing Single- and Double-Stranded Nucleic Acid Molecules Using Solid-State Nanopores. *Nano Lett.* **9,** 2953–2960 (2009).

79. Takashi Ito, Li Sun, Ronald R. Henriquez, & Crooks, R. M. A Carbon Nanotube-Based Coulter Nanoparticle Counter. *Acc. Chem. Res.* **37,** 937–945 (2004).

80. Ito, T., Sun, L. & Crooks, R. M. Simultaneous determination of the size and surface charge of individual nanoparticles using a carbon nanotube-based coulter counter. *Anal. Chem.* **75,** 2399–2406 (2003).

81. Ito, T., Sun, L., Bevan, M. A. & Crooks, R. M. Comparison of nanoparticle size and electrophoretic mobility measurements using a carbon-nanotube-based coulter counter, dynamic light scattering, transmission electron microscopy, and phase analysis light scattering. *Langmuir* **20,** 6940–6945 (2004).

82. Blundell, E. L. C. J., Mayne, L. J., Billinge, E. R. & Platt, M. Emergence of tunable resistive pulse sensing as a biosensor. *Anal. Methods* **7**, 7055–7066 (2015).

83. Weatherall, E. & Willmott, G. R. Applications of tunable resistive pulse sensing. *Analyst* **140,** 3318 (2015).

84. Willmott, G. R. & Moore, P. W. Reversible mechanical actuation of elastomeric nanopore, *Nanotechnology* **19,** 475504 (2008)

85. Roberts, G. S. *et al.* Tunable nano/micropores for particle detection and discrimination: Scanning ion occlusion spectroscopy. *Small* **6,** 2653–2658 (2010).

86. Vogel, R., Anderson, W., Eldridge, J., Glossop, B. & Willmott, G. A variable pressure method for characterizing nanoparticle surface charge using pore sensors. *Anal. Chem.* **84,** 3125–3131 (2012).

87. Kozak, D. *et al.* Simultaneous size and ζ-potential measurements of individual nanoparticles in dispersion using size-tunable pore sensors. *ACS Nano* **6,** 6990–6997 (2012).

88. Blundell, E. L. C. J., Vogel, R. & Platt, M. Particle-by-Particle Charge Analysis of DNA-Modified Nanoparticles Using Tunable Resistive Pulse Sensing. *Langmuir* **32,** 1082–1090 (2016).

89. Willmott, G. R. *et al.* Use of tunable nanopore blockade rates to investigate colloidal dispersions. *J. Phys. Condens. Matter* **22,** 454116 (2010).

90. Willmott, G. R., Yu, S. S. C. & Vogel, R. Pressure dependence of particle transport through resizable nanopores. *ICONN 2010 - Proc. 2010 Int. Conf. Nanosci. Nanotechnol.* 128–131 (2010). doi:10.1109/ICONN.2010.6045207

91. Ali, M. *et al.* Metal ion affinity-based biomolecular recognition and conjugation inside synthetic polymer nanopores modified with iron-terpyridine complexes. *J. Am. Chem. Soc.* **133,** 17307–17314 (2011).

92. Choi, L., Mach, T. & Bayley, H. Rates and Stoichiometries of Metal Ion Probes of Cysteine Residues within Ion Channels. *Biophysj* **105,** 356–364 (2013).

93. Wang, G., Wang, L., Han, Y., Zhou, S. & Guan, X. Nanopore detection of copper ions using a polyhistidine probe. *Biosens. Bioelectron.* **53,** 453–458 (2014).

94. Gao, R. *et al.* Ultrasensitive determination of mercury(II) using glass nanopores functionalized with macrocyclic dioxotetraamines. *Microchim. Acta* **183,** 491–495 (2016).

95. Zhai, Q. *et al.* Biomimetic nanopore for sensitive and selective detection of Hg(II) in conjunction with single-walled carbon nanotubes. *J. Mater. Chem. B* **2,** 6371 (2014).

2 Theory

2.1 Introduction

This chapter provides the common theory which is used throughout the thesis. The theory of the technique Tunable Resistive Pulse Sensing, which is applicable to all chapters covers the theory of transport through a conical nanopore, brief introduction to zeta potential and particle surface charge and ion current rectification. Where required additional detailed theory is included in each chapter.

2.2 Tunable Resistive Pulse Sensing

Resistive pulse sensing, RPS, can be used to determine the size, concentration and charge of particles in an electrolyte solution.[1] In RPS, two fluid cells are separated by a pore in a nonconductive membrane. The fluid chambers are filled with a conducting electrolyte solution and electrodes are placed in each cell, a potential difference is applied across the pore and a current is established,[1] Figure 2.1. A recent adaptation of RPS is tunable resistive pulse sensing (TRPS).[2,3]

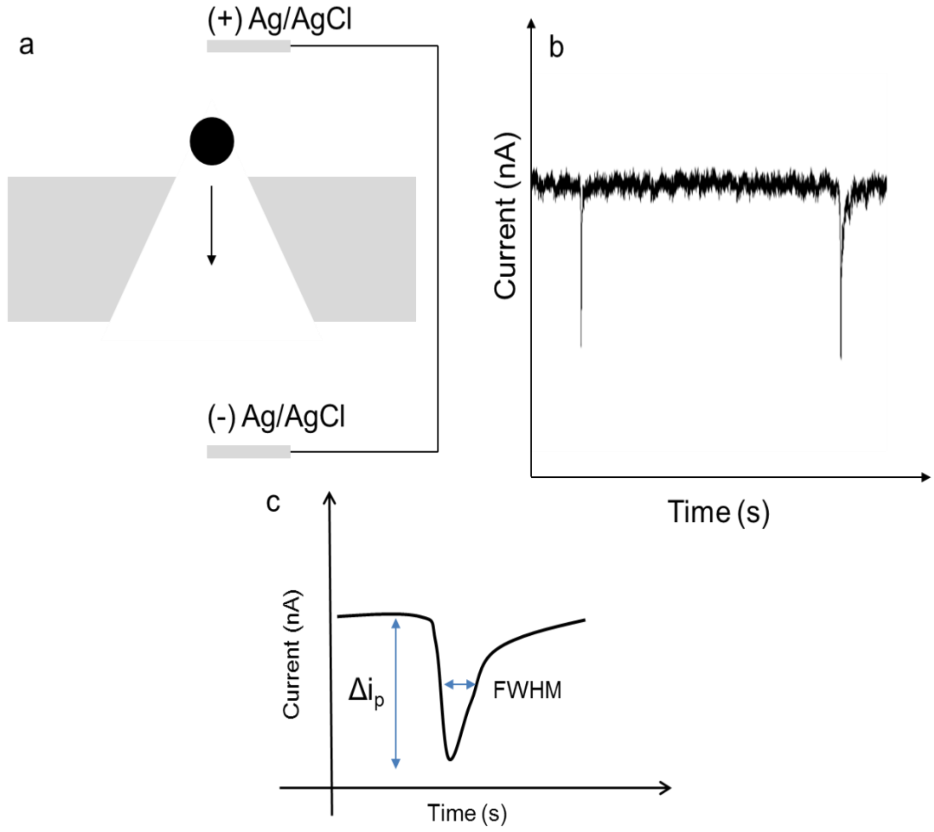

Figure 2.1 a) Schematic of a particle traversing through a nanopore, separating two fluid cells with an Ag/AgCl electrode in each. b) Current time recording of a particles traversing the pore and creating blockade events. c) Schematic of particle blockade event, Δi_p shows the blockade magnitude and FWHM is in indication of the particle translocation.

TRPS incorporates an elastomeric pore which can be stretched in real time. The ability to adjust the pore size is advantageous, allowing the pore to be tuned to suit the analyte being detected, Figure 2.2.[4]

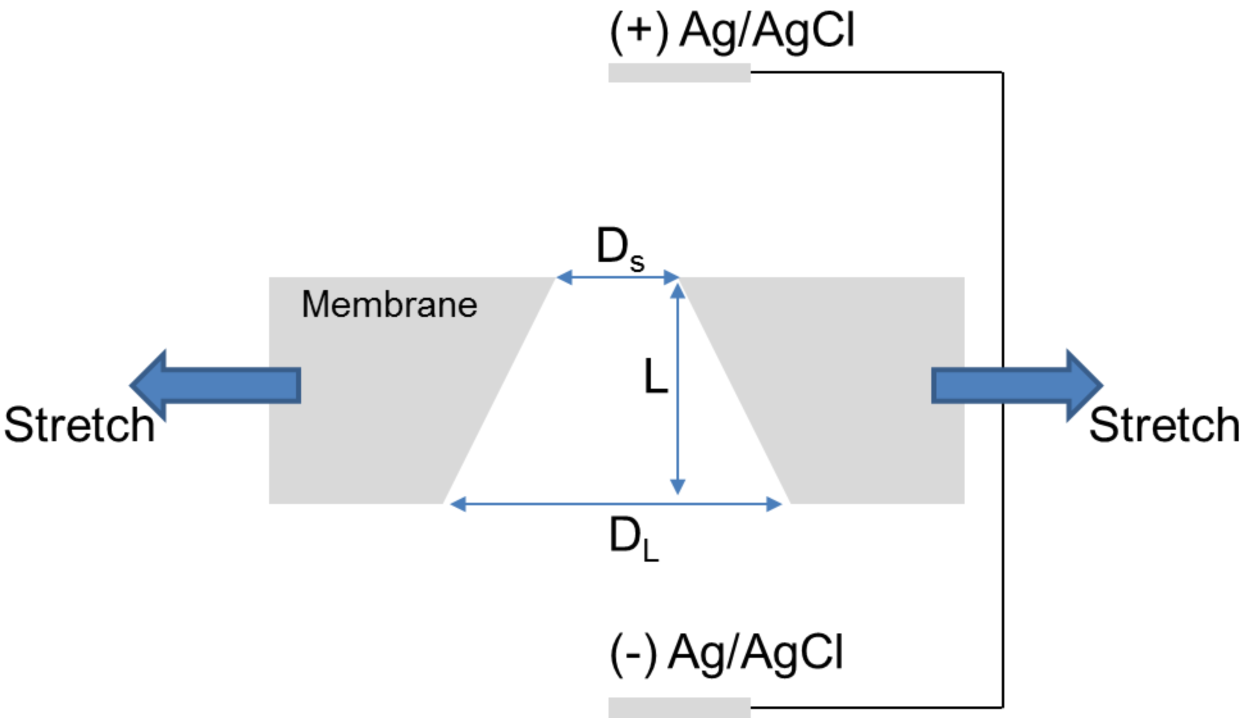

Figure 2.2 Schematic of a tunable nanopore used in TRPS, stretching the pore changes the size of the pore. D_L and D_S are the large and small diameters of the pore. L is the length of the pore.

The instrument associated with TRPS is the qNano, which is manufactured by Izon Sciences, Christchurch (NZ). The pore is mounted on teeth, with the fluid cells above and below the membrane. The membranes used are penetrated with a tungsten needle to create the conical pore.[3] The size of the pore can be modified by using different sized needles which allows for the detection of particles ranging from 50 nm to 10 µm over the range of pores manufactured by Izon Science. The pore is mounted on teeth which can be altered to stretch the pore.

Figure 2.3 a) The lower fluid cell and teeth for mounting the nanopore. b) The pore is placed onto the teeth and upper fluid cell twisted into place. c) Faraday places over the fluid cell.

The lower fluid cell is filled with an electrolyte and the pore mounted onto the teeth above, Figure 2.3a. The teeth are then altered to the desired stretch, which is dependent on the sample being analysed.The upper fluid cell attached on top and twisted into position, Figure 2.3b. The same electrolyte is placed in the upper fluid cell. A Faraday cage is placed over the fluid cells to reduce background noise, Figure 2.3c. A potential difference is applied across the membrane. A baseline current is established. The current is dependent on the pore size, applied voltage and ionic strength of the electrolyte and is shown in equation 2.1 describing Ohm's law.

$$I = \frac{V}{R} \tag{2.1}$$

Where, I is the current and V the potential difference and,

$$\text{where, } R = \frac{4L\rho}{\pi D_L D_S} \tag{2.2}$$

where, D_L and D_S are the large and small diameters of the pore, ρ is the resistivity of the electrolyte, and L is the length of the pore. [7] The electrolyte is removed from the upper fluid cell and replaced with a sample suspended in electrolyte. TRPS can complete particle-by-particle analysis of complex mixtures and solutions. The technology enables accurate monitoring of a particle's electrophoretic mobility, as well as particle characteristics such as particle size and surface charge.

Pores used in TRPS have unknown dimensions unlike solid state pores. The tunable pore must be calibrated to determine the samples size and concentration. A calibration particle of known size and concentration is analysed under the same conditions as the sample. The theory involved in size and concentration analysis is presented in more detail below.

2.2.1 Size Analysis

Samples, suspended in electrolyte, are introduced into the upper fluid cell. When a particle traverses the pore, a volume of electrolyte is displaced. This creates a blockade event, Δi_p, Figure 2.1c. The blockade event, referred to as a pulse, provides information on the velocity at which the particle is travelling through the pore and the size of the particle.

The conical pore gives rise to an asymmetric current pulse with resistance being highest at the pore entrance, which results in a large drop in current which tails back to the original baseline as the particle travels through the pore.[5] The change in resistance, ΔR, across the length of the pore, L, is given in equation 2.3.[6]

$$\Delta R = \rho \int_0^L \frac{dz}{A(z)} - R \tag{2.3}$$

where ρ is the resistivity of the electrolyte, $A(z)$ is the cross-sectional area perpendicular to the pore axis z and R is the pore resistance. The blockade magnitude can be used to determine the size of the particle as the change in resistance is directly related to the volume of the analyte.

2.2.2 Concentration Analysis

The frequency of the pulses, J, is related to the concentration of the particle, C_s,[8] and the velocity, V_P of the traversing particle.

$$J = C_s \, x \, V_P \tag{2.4}$$

The velocity of the particle is a sum of fluidic, V_F, electrophoretic, V_E, and electroosmotic, V_O, velocities, Figure 2.4.[9] Although present, diffusion, D, is ignored due to having a negligible contribution in comparison to the magnitude of the other forces. Diffusion in TRPS is less than 5 % of the electrophoretic velocity.[10,11]

$$V_p = V_F + V_E + V_O + D \tag{2.5}$$

V_p, can be written as,

$$V_p = \varepsilon \frac{\zeta_{particle} - \zeta_{pore}}{\eta} E + \frac{Q_p}{A} \tag{2.6}$$

Where, ε and η are the permittivity of the solution and the viscosity of the solution respectively, $\zeta_{particle}$ and ζ_{pore} are the zeta potentials of the particle and the pore surface respectively and E is the electric field. Q_p is the pressure driven volumetric fluid flow rate and A is the cross-sectional area of the pore.

The pulse frequency is also related to the pressure applied across the pore. In the TRPS set-up an inherent pressure head of 28 Pa is always present due to gravity, which corresponds to a fluid height of 0.28 cm, when 40 µL of sample is added.[9] External pressure can be applied to the system by using the variable pressure module (VPM). Applying a pressure to the system is advantageous when measuring sample concentrations.

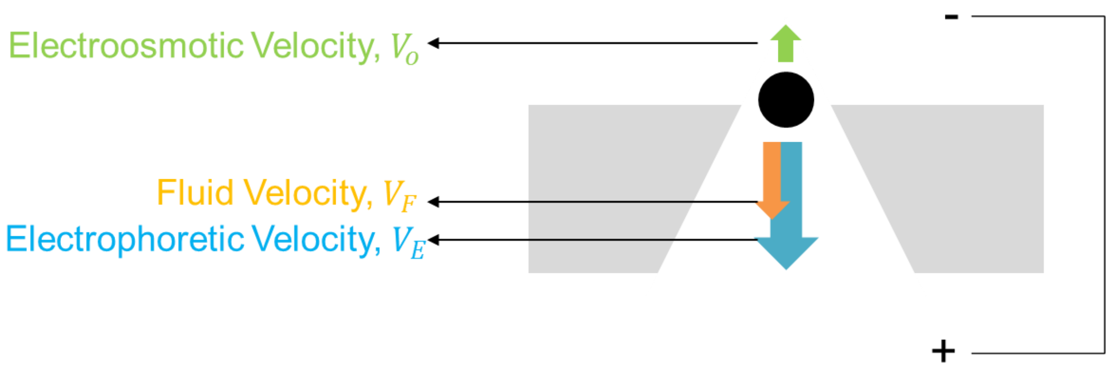

Figure 2.4 Schematic of the three forces acting on a particle as it translocates through the nanopore.

Figure 2.4 shows the three forces acting on the particle as it traverses the pore. Fluidic and electrophorectic mobility contribute the most to the particle's velocity. The electroosmotic flow is dependent on the charge of the nanopore, in the traditional TRPS set up, the pore on the charge is negative. In TRPS, electrophoresis is typically made to be the dominant force.

2.2.3 Electroosmosis

When an electric field is applied across the nanopore, bulk fluid motion is observed. Electroosmosis stems from the electrical forces on the ions within the double layer on the nanopore wall. The electroosmotic velocity is proportional to the applied electric field and is dependent on the pore wall charge and the electrolyte in contact with the pore. Electroosmotic velocity, $V_o,$ is defined in equation 2.7.

$$V_o = \frac{\varepsilon \zeta_{pore}}{\eta} E \tag{2.7}$$

2.2.4 Electrophoretic Mobility

The velocity of which a particle moves in the presence of an electric field, is related to the strength of the electric field, E and its electrophoretic mobility, μ. For a spherical particle this can be presented as

$$V_E = \mu E \tag{2.8}$$

Where, V_E is the particle velocity.[12]The particles electrophoretic mobility is described by the Henry equation, 2.9,

$$\mu = \frac{2\varepsilon \zeta_{particle} f(ka)}{3\eta} \tag{2.9}$$

Where, ε and η are the dielectric constant and viscosity and $f(ka)$ is Henry's function. k is the reciprocal length of the electrical double layer (the Debye length) and a is the particles radius. Two values are usually used for the Henry function, for particles in polar media the maximum value of $f(ka)$ is 1.5 (Smoluchowski approximation) and for particles in non-polar media the minimum value of $f(ka)$ is 1 (Hückel approximation).

The electrophoretic mobility is determined by the balance between electrical and viscous forces which act on the particle and is affected by the concentration of the electrolyte. The counterions associated with the particle oppose the movement of the particle, which results in electrophoretic retardation.[12]

2.2.5 Translocation Velocity

The relative velocity of the particle can be calculated from the pulse width, calculated by the software automatically. Multiple time points are recorded along the pulse and are denoted $T_{0.90}$, $T_{0.80}$, $T_{0.70}$ *etc.*, and the reciprocal of the average time from each point can be used to calculate the relative particle velocity.[13]

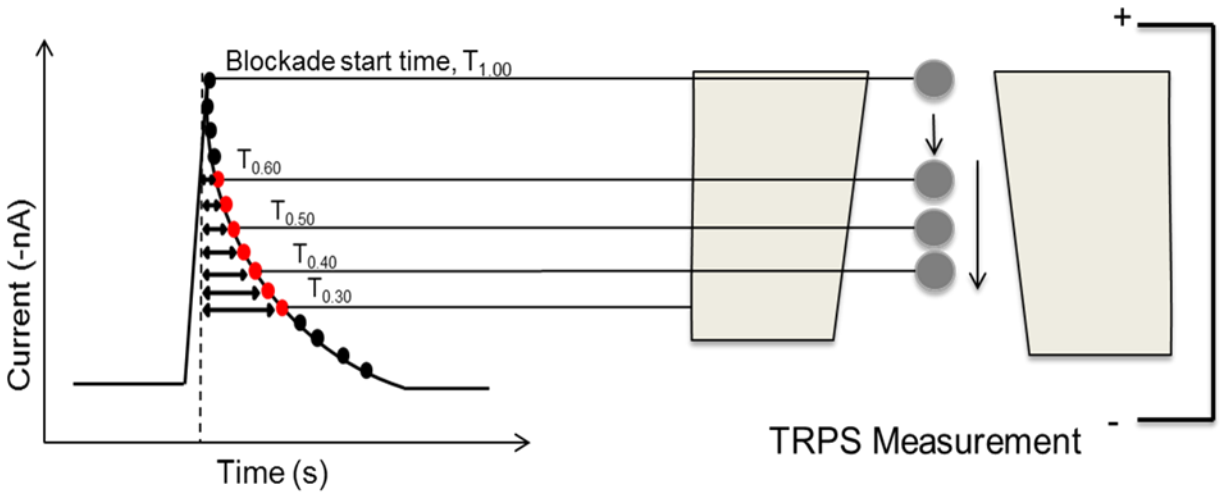

Figure 2.5 Schematic of the blockade times, T0.3, T0.4, T0.5…, and the position of the particle in the pore (not to scale). Plotting 1/T gives the particles velocity through the pore.

For each blockade, the time at which the peak occurs is defined as $T_{1.0}$ (time at 100% of peak magnitude) and the maximum magnitude of the pulse (relative to the local baseline resistance) is recorded as the blockade start time, $T_{1.00}$. In the example shown in Figure 2.5, 4 sections, 60%, 50%, 40%, and 30% of $T_{1.00}$ are displayed. The proportional blockade magnitude is equal for any given particle (small or large). The relative magnitude is an indicator of the particle's position within the pore. The duration from $T_{1.0}$ to each of these sections is defined at $T_{0.60}$, $T_{0.50}$, $T_{0.40}$ and $T_{0.30}$. TRPS strategies have shown how the velocity of the particle can be used to determine its zeta potential. In this work, we stop short of calculating the actual zeta potential of samples.[13]

2.2.5.1 Ionic Strength

Changing the electrolyte concentration changes the ionic strength, I, of the system. The relationship between ionic strength and ions is shown in equation 2.10

$$I = \frac{1}{2}\sum C_i z_i^2 \tag{2.10}$$

Where, C_i is the concentration of ion i, Z_i is the charge on the ion and the sum is taken for all ions in the solution. The change in ionic strength changes the double layer thickness surrounding the silica nanoparticle. The relationship between particle mobility and double layer thickness is described using the Henry equation, (2.9) Figure 2.6 shows how the potential drop across the double layer changes with ionic strength and the measured ζ potential is greater at lower ionic strengths.

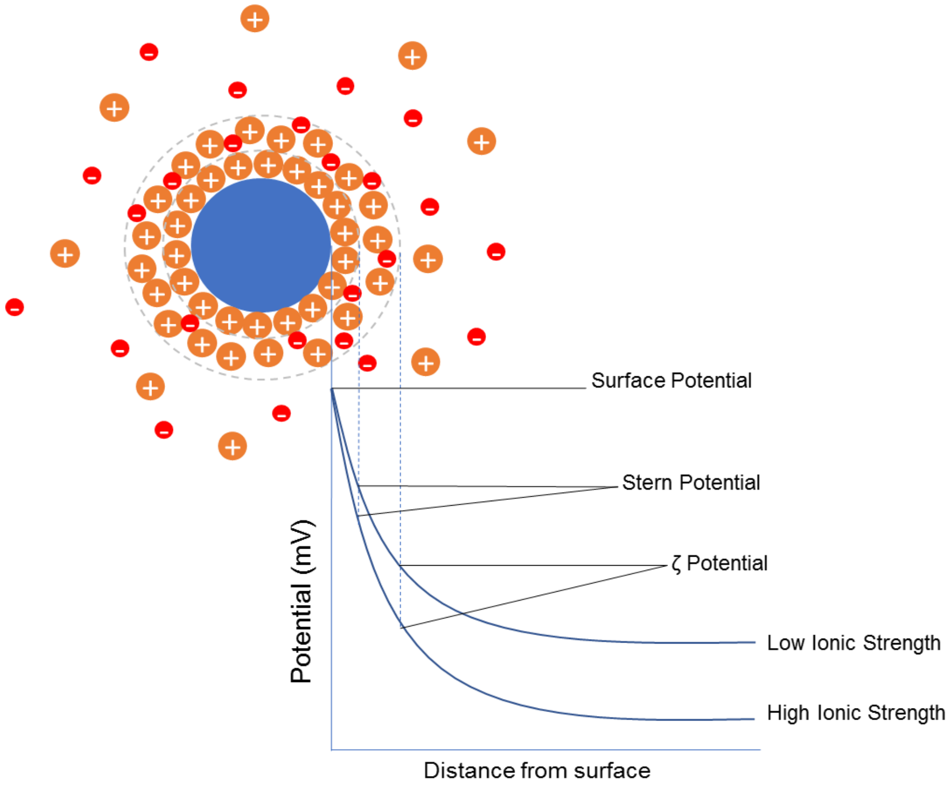

Figure 2.6 The potential drop across the double layer changes with ionic strength. At low electrolyte concentration, the potential drop is less so therefore the ζ-potential is greater.

2.2.6 Zeta Potential

Although zeta potential values are not used in this thesis, the theory is still relevant to particle translocation through the nanopore. $\zeta_{particle}$ can be calculated by measuring the electrophoretic mobility, μ, of the particle and then applying the Smoluchowski approximation. The Smoluchowski approximation defines zeta potential as

$$\zeta_{particle} = \frac{\eta \mu}{\epsilon} \tag{2.11}$$

The translocation mobility, μ_{Tr}, is proportional to the electrophoretic mobility of the particles and can be defined as[15]

$$\mu_{Tr} = \frac{\epsilon_r \epsilon_o \zeta_{particle}}{\eta} \tag{2.12}$$

Where $\epsilon_r \epsilon_o$ and η are the solution permittivity and viscosity inside the nanopore.

2.2.7 Ionic Current Rectification

Under most RPS measurements, the ionic strength is high, therefore the base current is predictable. However, at low ionic strength, conical nanopores exhibit ionic current rectification (ICR) properties.[16–23] The charge on the pore wall creates areas of ion accumulation and depletion within the pore depending on the applied voltage.[15] This leads to the recorded current being higher at one voltage compared to the recorded current at the voltage of opposite polarity. The ion accumulation/depletion arises from the surface charge of the nanopore and the asymmetry in the pore geometry.[15,21]

For a conical nanopore with a uniform negative surface, the recorded current at negative potentials is higher than the current at a positive potential with equal magnitude. When a negative potential is applied to the Ag/AgCl electrode inside the nanopore, using KCl electrolyte, the K^+ flux is directed from the external bulk solution to the pore interior, while Cl^- moves in the opposite direction. As the pore is negatively charged, the Cl^- ions are rejected from the pore surface and their translocation through the pore is reduced. The Cl^- rejection leads to the accumulation of K^+ and Cl^- within the pore interior resulting in a higher conductivity within the nanopore. When a positive potential is applied, the transport of Cl^- from the bulk into the pore interior is hindered by the nanopore's negative charge and thus Cl^- is depleted within the pore interior. The nanopore conductivity decreases and the recorded current is lower.[22]

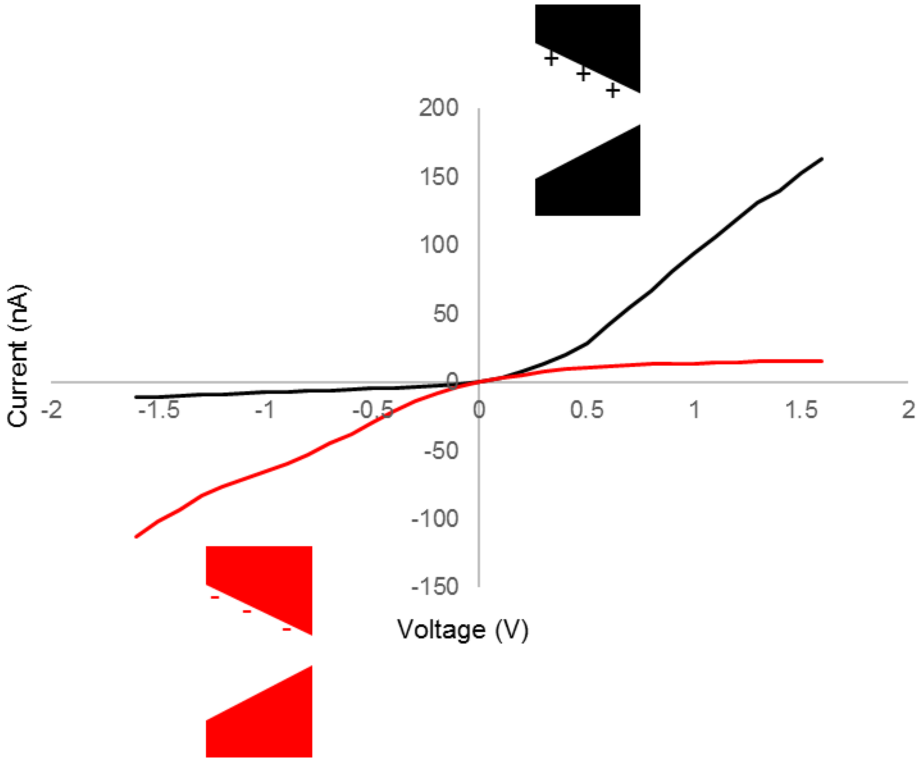

Figure 2.7 Typical current-voltage (I-V) response through a conical nanopore with a postive surface charge (Black line) and a conical nanopore with a negative surface charge (Red line).

Figure 2.7 shows the resulting currents from a negative and positively charged nanopore. The black line represents a typical current-voltage (*I*-*V)* curve generated from a positively charged nanopore, the current recorded at positive voltages is higher than at negative voltages. The red line, a negatively charged pore, shows the opposite. Recording the current flow through the nanopore provides information on the surface charge of the nanopore.

2.3 References

1. Ito, T., Sun, L. & Crooks, R. M. Simultaneous determination of the size and surface charge of individual nanoparticles using a carbon nanotube-based coulter counter. *Anal. Chem.* **75,** 2399–2406 (2003).

2. Roberts, G. S. *et al.* Tunable nano/micropores for particle detection and discrimination: Scanning ion occlusion spectroscopy. *Small* **6,** 2653–2658 (2010).

3. Sowerby, S. J., Broom, M. F. & Petersen, G. B. Dynamically resizable nanometre-scale apertures for molecular sensing. *Sensors Actuators, B Chem.* **123,** 325–330 (2007).

4. Kozak, D., Anderson, W. & Trau, M. Tuning Particle Velocity and Measurement Sensitivity by Changing Pore Sensor Dimensions. *Chem. Lett.* **41,** 1134–1136 (2012).

5. Willmott, G. R. & Parry, B. E. T. Resistive pulse asymmetry for nanospheres passing through tunable submicron pores. *J. Appl. Phys.* **109,** (2011).

6. Vogel, R. *et al.* Quantitative sizing of nano/microparticles with a tunable elastomeric pore sensor. *Anal. Chem.* **83,** 3499–3506 (2011).

7. Heins, E. A., Siwy, Z. S., Baker, L. A. & Martin, C. R. Detecting single porphyrin molecules in a conically shaped synthetic nanopore. *Nano Lett.* **5,** 1824–1829 (2005).

8. DeBlois, R. W., Bean, C. P. & Wesley, R. K. A. Electrokinetic measurements with submicron particles and pores by the resistive pulse technique. *J. Colloid Interface Sci.* **61,** 323–335 (1977).

9. Kozak, D. *et al.* Simultaneous size and ζ-potential measurements of individual nanoparticles in dispersion using size-tunable pore sensors. *ACS Nano* **6,** 6990–6997 (2012).

10. Willmott, G. R. & Parry, B. E. T. Resistive pulse asymmetry for nanospheres passing through tunable submicron pores. *J. Appl. Phys*. **109**, 094307 (2011)

11. Willmott, G. R. *et al.* Use of tunable nanopore blockade rates to investigate colloidal dispersions. *J. Phys.: Condens. Matter* **22,** 454116 (2010)

12. O’Brien, R. W. & White, L. R. Electrophoretic mobility of a spherical colloidal particle. *J. Chem. Soc. Faraday Trans. 2 Mol. Chem. Phys.* **74,** 1607–1626 (1978).

13. Blundell, E. L. C. J., Vogel, R. & Platt, M. Particle-by-Particle Charge Analysis of DNA-Modified Nanoparticles Using Tunable Resistive Pulse Sensing. *Langmuir* **32,** 1082–1090 (2016).

14. Makino, K. & Ohshima, H. Electrophoretic mobility of a colloidal particle with constant surface charge density. *Langmuir* **26,** 18016–18019 (2010).

15. Arjmandi, N., Van Roy, W., Lagae, L. & Borghs, G. Measuring the electric charge and zeta potential of nanometer-sized objects using pyramidal-shaped nanopores. *Anal. Chem.* **84,** 8490–8496 (2012).

16. Woermann, D. Electrochemical transport properties of a cone-shaped nanopore: high and low electrical conductivity states depending on the sign of an applied electrical potential difference. *Phys. Chem. Chem. Phys.* **5,** 1853–1858 (2003).

17. Lan, W. J., Holden, D. A. & White, H. S. Pressure-dependent ion current rectification in conical-shaped glass nanopores. *J. Am. Chem. Soc.* **133,** 13300–13303 (2011).

18. Siwy, Z. S. Ion-current rectification in nanopores and nanotubes with broken symmetry. *Adv. Funct. Mater.* **16,** 735–746 (2006).

19. Siwy, Z., Heins, E., Harrell, C. C., Kohli, P. & Martin, C. R. Conical-nanotube ion-current rectifiers: The role of surface charge. *J. Am. Chem. Soc.* **126,** 10850–10851 (2004).

20. Gamble, T. *et al.* Rectification of ion current in nanopores depends on the type of monovalent cations: Experiments and modeling. *J. Phys. Chem. C* **118,** 9809–9819 (2014).

21. Siwy, Z. *et al.* Rectification and voltage gating of ion currents in a nanofabricated pore. *Europhys. Lett.* **60,** 349–355 (2002).

22. Lan, W. J. *et al.* Voltage-Rectified Current and Fluid Flow in Conical Nanopores. *Acc. Chem. Res.* **49,** 2605–2613 (2016).

23. Siwy, Z. *et al.* Ion transport through asymmetric nanopores prepared by ion track etching. *Nucl. Instruments Methods Phys. Res. Sect. B Beam Interact. with Mater. Atoms* **208,** 143–148 (2003).

3 Effect of surface charge on particle velocity

This chapter presents the results of particle translocation velocity and how particle velocity is affected by ionic strength and pH. The work presented shows how ionic strength changes the shielding of charge around the particle and the how that is related to the particles mobility through the pore. Functional groups, such as carboxyl and amines, can be protonated/deprotonated by decreasing or increasing the pH. The changes in pH in turn alter the charge on the particles surface and is shown by a change in particle mobility through the nanopore. The particles translocation velocity can be used to monitor changes on the particles surface when modifying the particles with either a ligand or DNA. Here, the transport of silica nanoparticles and carboxyl coated nanoparticles through a nanopore were studied. The velocity of the particles increases with decreasing ionic strength as described by double layer theory presented in Chapter 2. The nanoparticles were modified with a ligand (APTES) and DNA. The subsequent particle velocities differ to those of the unmodified particles, making TRPS a suitable platform for monitoring changes upon a nanoparticle surface.

3.1 Aims and Objectives

The main objective from this work was to demonstrate how particle velocity through the nanopore can be tuned by changing the concentration and pH of the electrolyte surrounding the electron. By changing the environment that the particle is suspended in, the velocity of that particle will changed as described in Chapter 2. A subsequent aim was to study the modification of the particles surface via particle velocity in a range of electrolytes.

3.2 Introduction

To understand how the particle translocation velocity relates to the particles surface charge. The nanoparticles used were characterised in a wide range of ionic strengths and pH, which is often varied in environmental samples. To develop a sensor for the detection of heavy metal ions using TRPS it is necessary to modify the surface of nanoparticles with a variety of ligands. To develop the sensor using TRPS, the particle translocation velocity will be measured. By modifying particles with a ligand and using double layer theory, we aimed to create a particle were the velocity changed in the presence of a specific metal ion.

Two different particles were looked at which represent the surface chemistry used throughout the thesis. Firstly, commercially available silica nanoparticles were modified with a ligand which was known to bind to a heavy metal ion.[1] Upon modification with the ligand, the charge of the particle was altered. This resulted in different translocation velocities, which also changed as pH and ionic strength were altered. Secondly, commercially available carboxyl coated superparamagnetic particles were modified with DNA apatmers. The DNA sequence was functionalised with an amine linker which can be easily grafted to the nanoparticle via EDC coupling chemistry. Again, analysing the particles velocity in a range of ionic strengths and pH allowed the changes to the particles surface chemistry to be monitored.

3.3 Experimental

3.3.1 Methods and Materials

The following chemicals were purchased from Sigma Aldrich, UK, (3-aminopropyl)triethoxysilane (APTES, ≥ 98 %, A3648), tetraethyl orthosilicate (TEOS, 98 %), poly(ethyleneimine), PEI, (Mw 750 000 g mol^{-1}, analytical standard, 50 % wt., P3143), poly(acrylic acid-co-maleic acid) (PAAMA, Mw ~3000 g mol^{-1} 50 % wt., 416053), sodium hydroxide (NaOH, reagent grade, ≥98 %, S5881), (2-(N-morpholino)ethanesulfonic acid hydrate (MES hydrate, ≥99.5 %, M2933) and *N*-hydroxysulfosuccinimide sodium salt (NHS, ≥98.5 %, 56485).The following chemicals were purchased from Fisher Scientific, UK, potassium chloride (KCl, >99 %, P/4240/60), potassium hydroxide (KOH, 0.1M, >85%, P/5600/60), and sodium chloride (NaCl, analytical grade, S/3160/60).. The following chemicals were purchased from VWR, UK, hydrochloric acid (HCl, 0.5 M, 37%), ethanol (EtOH, 100 %v/v) and ammonium hydroxide (NH_4OH, 28%). Tunable conical pores (NP200s) were purchased from Izon Science, Christchurch, NZ. 1-ethyl-3-(3-dimethylaminopropyl)carbodiimide hydrochloride (EDC, 22980) was purchased from Thermo Scientific, UK.

All reagents were used without further purification and all solutions were prepared in deionised water with a resistivity of 18.2 MΩ cm (Maxima). Prior to analysis the pH of the solution was measured using a Mettler Toledo easy five pH meter with a Mettler Toledo InLab micro electrode.

3.3.2 Particles

Silica nanoparticles, SiNPs, (150 nm in diameter, 5 % wt, 56799) were purchased from Sigma Aldrich, UK. Superparamagnetic particles were purchased from Ademtech, France (125 nm in diameter, 0211). The particles were modified using PEI and PAAMA to ensure carboxyl groups were present on the particles.(reference) Particles were taken from stock (50 µL) and suspended in PEI (1 mL, 5% in H_2O). The solution was placed on the rotary wheel for 30 minutes. The solution was vortexed for 5 minutes at 10 000 rpm, the PEI solution removed from the particles and replaced with water. The sample was vortexed and sonicated until the particles were fully dispersed. This wash step was repeated twice to ensure all excess PEI had been removed. The PEI coated particles were suspended in PAAMA (5% in 50 mM NaCl) for 30 minutes and placed on the rotary wheel. The same process for removing the excess PEI was used to remove PAAMA. The particles were then stored at 2 – 4ºC in DI water with a concentration of 1 x 10^{11} particle/ mL. The concentration of particles was measured using TRPS and calibrated against a sample of known concentration.

Calibrations particles (CPCs) were purchased from Izon Science, Christchurch, NZ. The calibration particles were carboxylated polystyrene particles (210 nm in diameter, denoted CPC200 and 400 nm in diameter denoted CPC400). The NP200 pores used have an analysis range of 85 – 500 nM, therefore when measuring the larger particle sizes, the calibration was performed using CPC400s.

Table 3.1 Summary of particles and sizes used within Chapter 3.

Particle	Size (nm)
Silica NPs	150
Carboxyl Particles	125
CPC200	210
CPC400	400

3.3.3 Custom DNA Oligonucleotides

The oligonucleotides used in this study were purchased as lyophilised powders from Sigma Aldrich, UK. The sequence was synthesised with an amine functional group at the 3’ end: 5’-GGAAGGTGTGGAAGG-3’ (lead binding aptamer, TBAA).

3.3.4 Silica Nanoparticle Synthesis

EtOH (10.85 ml), NH_4OH (3.5 ml, 14.5 M) and deionised water (10 ml) added in a conical flask and the solution mixed continuously. TEOS (0.65 ml) was added rapidly and the solution stirred for 30 minutes at room temperature. The SiO_2 suspension was washed three times with EtOH by repeated centrifugation (5000 rpm for 5 min). The samples were stored in EtOH until analysis.

3.3.5 Silica Nanoparticle Modification

The modification of the SiNPs followed a preparation reported previously.[1] The SiNPs (5 mL) were centrifuged for 10 minutes at 10 000 rpm and washed with acetone (5 mL). The wash step was repeated and the particles were suspended in acetone (5 mL). The SiNP solution was heated to 60°C in a round bottom flask and APTES (1 mL) added to the reaction and then refluxed for 2 hr. The solution was filtered under vacuum using a sintered glass crucible and the nanoparticles were washed with excess acetone before being left to air dry. This yielded APTES modified silica nanoparticles, Si-APTES. The presence of the APTES on the surface was confirmed using FT-IR (PerkinElmer).

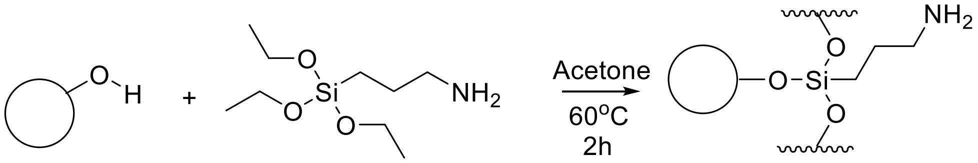

Scheme 3.1 Modification of silica nanoparticles with APTES.

3.3.6 DNA Modification

The DNA sequence was dissolved in 100 mM MES buffer (pH 5.7) containing 1 mg ml-1 EDC and 1 x 10^{10} carboxylated particles/ mL. The final concentration of DNA was 410 nM. The solution containing the particles was placed on the rotary wheel for 1 hour. To remove excess DNA, the solutions containing the magnetic carboxyl particles 150 nm particles were placed in a MagRack (Life Sciences). After 5 minutes, the particles had formed a visible cluster and the solution was removed and replaced with an equal volume of PBS (10 – 100%).

3.3.7 TRPS Set-Up

All measurements were conducted using the qNano (Izon Sciences Ltd, NZ) combining tunable nanopores with data capture and analysis software, Izon Control Suite v.3.1. Analysis of the conductive pulses generated was performed using Clampfit 10 software. The lower fluid cell always contains the electrolyte (75 µL) that the particle is suspended in and the upper fluid cell contains 40 µL of sample. Prior to TRPS analysis, all samples were vortexed for 30 s and sonicated for 2 minutes. During each sample run, the system was washed by placing 40 µL of the run electrolyte into the upper fluid cell several times with various pressures applied to ensure there were no residual particles remaining and therefore no cross contamination between samples. Calibration particles CPC400s and CPC200s were used in the experiments depending on the pore stretch.

The relative velocity of the particle is calculated from the pulse width, calculated by the software automatically. Multiple time points are recorded along the pulse and are denoted $T_{0.90}$, $T_{0.80}$, $T_{0.70}$ *etc.*, and the reciprocal of the average time from each point can be used to calculate the relative particle velocity. Data presented in this chapter report relative particle velocity at $1/T_{0.5}$.[2]

3.3.7.1 Silica Nanoparticles

Silica nanoparticles were washed twice with the desired electrolyte by centrifugation (10 000 rpm for 10 min). The silica nanoparticles were re-suspended in electrolyte and diluted by 500 for analysis, resulting in a concentration of ~1 x 10^9 particle/mL. The nanoparticles were run on a NP200 pore with a measurable size range of 85 – 500 nm particles. No pressure was applied to the system, unless calibrating the sample for size and concentration.

3.3.7.2 Carboxyl Nanoparticles

The nanoparticles were diluted to ~1 x 10^9 particle/mL in the electrolyte that the particles would be analysed in. The particles were run on a NP200 pore with no pressure, unless calibrating the sample for size and concentration.

3.4 Results and Discussion

3.4.1 Silica Nanoparticles Synthesis

The Stöber synthesis is a reaction which is known to produce monodisperse silica nanoparticles.[3] The TEOS reaction with water and ethanol is catalysed by ammonia.[3] The first reaction step gives the singly hydrolysed TEOS monomer.

$$Si(OR)_4 + H_2O \rightarrow (OR)_3Si(OH) + ROH \tag{3.1}$$

The intermediate product condenses to form silica.

$$(OR)_3Si(OH) + H_2O \rightarrow SiO_2 + 3ROH \tag{3.2}$$

Varying the concentrations, volumes of reactants and temperature will vary the silica growth and thus determine the nanoparticle size.[4]

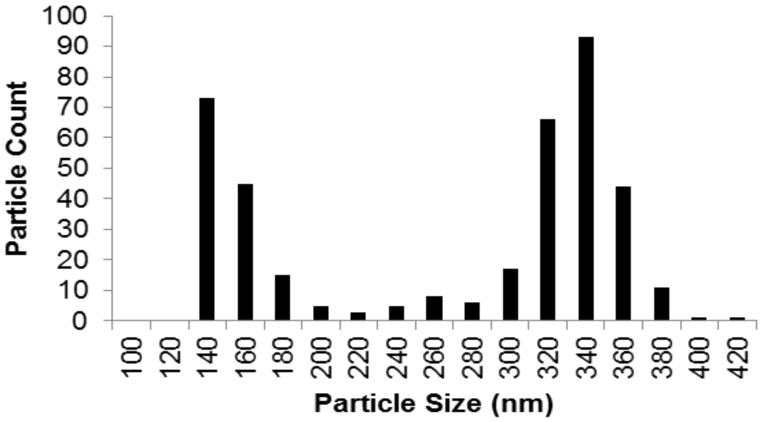

Figure 3.1 Size distribution of synthesised nanoparticles run on a NP200 pore, 44.50 mm stretch and 0.46 V.

The silica nanoparticles synthesised were characterised using TRPS and the pore was calibrated using CPC400. Figure 3.1 shows the size distribution of the synthesised particles. The sample was found to be bimodal and not monodisperse as desired. Two sizes of the particles can be clearly seen at circa 150 nm and 340 nm.

3.4.2 Surface Modification with APTES

Although the silica nanoparticles synthesised were bimodal, the silica was modified with APTES and used to demonstrate that analysing the samples with TRPS could distinguish between and characterise the two sets of nanoparticles. The modification of silica surfaces with APTES has been studied extensively previously.[5-9] The amine group allows provides a reactive end group and can be easily modified for further modification. The synthesised silica nanoparticles were modified with APTES, shown in Scheme 3.2.

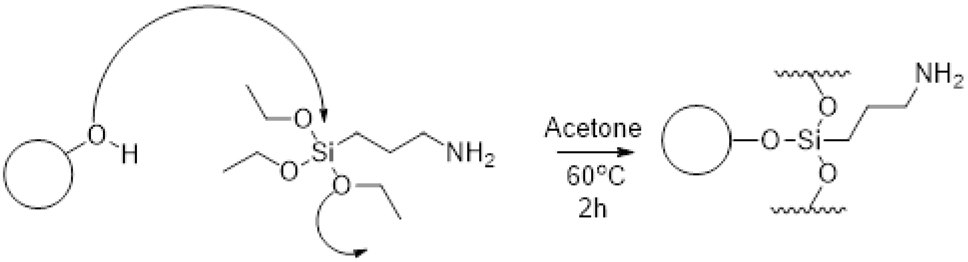

Scheme 3.2 Mechanism and conditions needed for the modification of silica nanoparticles with APTES

The APTES binding to the silica nanoparticles was confirmed by infrared spectroscopy (IR). An absorption peak at 1560 cm^{-1} can be ascribed to the NH_2 bending mode of free NH_2 group and this confirms the presence of the NH_2 group from the APTES,[7,9] shown in Figure 3.2. For comparison the IR for the unmodified silica nanoparticles is shown in Figure 3.3.

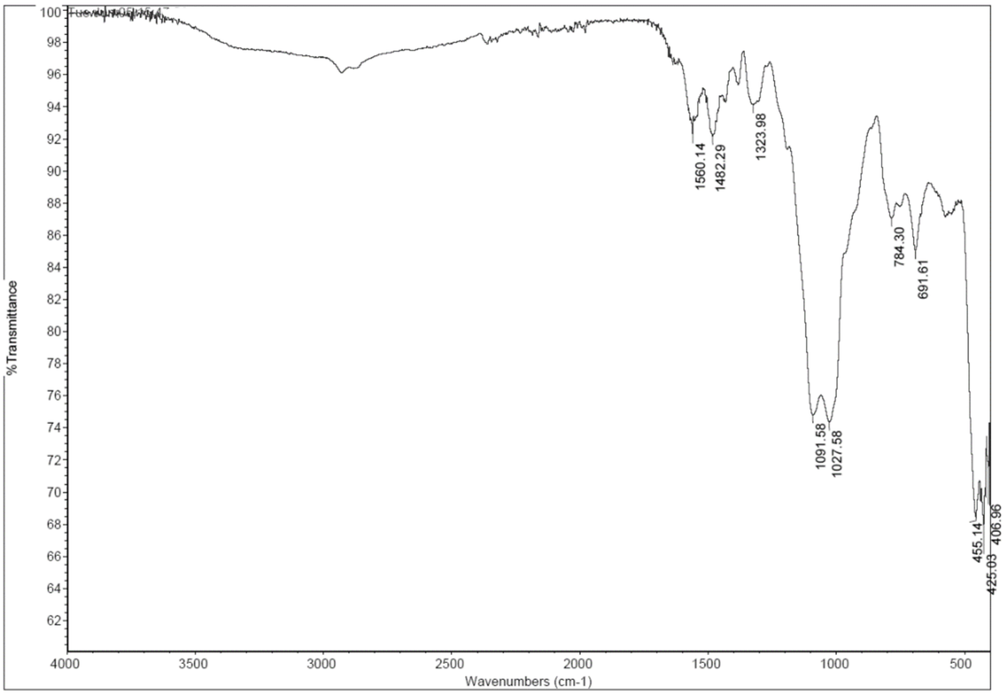

Figure 3.2 IR spectrum of modified silica nanoparticles.

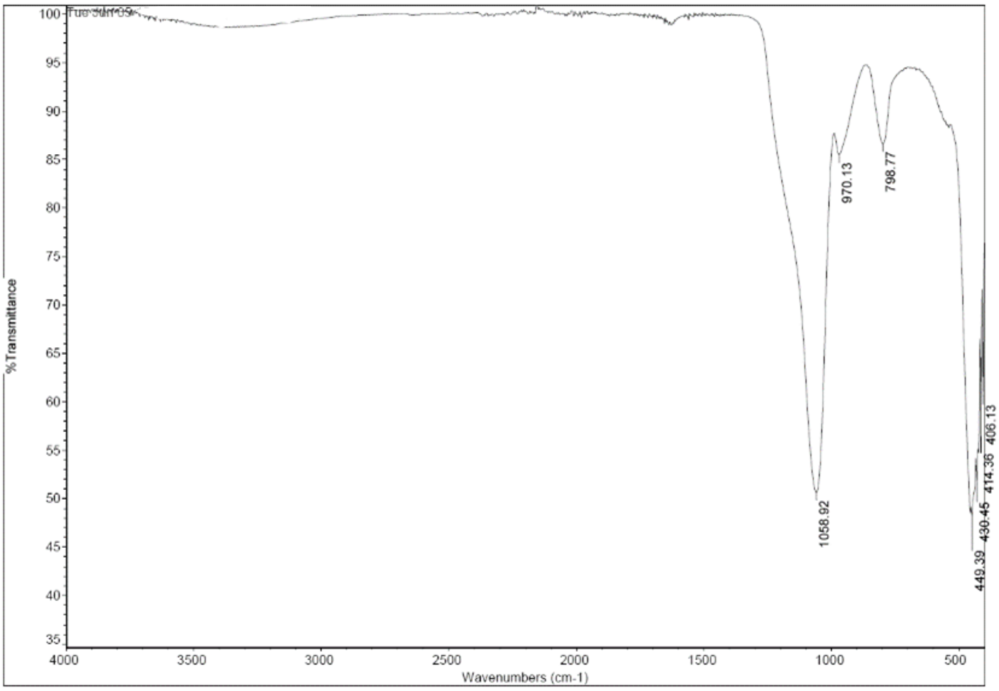

Figure 3.3 IR spectrum of silica nanoparticles.

The samples were then analysed using TRPS. The particle velocities were recorded for the silica and APTES modified silica particles, Figure 3.4. A decrease in particle velocity was recorded upon modification. The potential bias that the particles were analysed on was a clear indication that the particle modification was successful. The bare silica, ran on a positive bias. Upon having the silica surfaces modified, no translocation events were observed on the positive bias, Figure 3.5. The changes to the particles surface chemistry had changed the particles charge. A negative bias was then applied and translocation events were recorded. This change in experimental conditions was also used to confirm that the surfaces had been modified with APTES. Following this work, more detailed studies of particle velocities was carried out using commercially bought silica nanoparticles, as these had a uniform size.

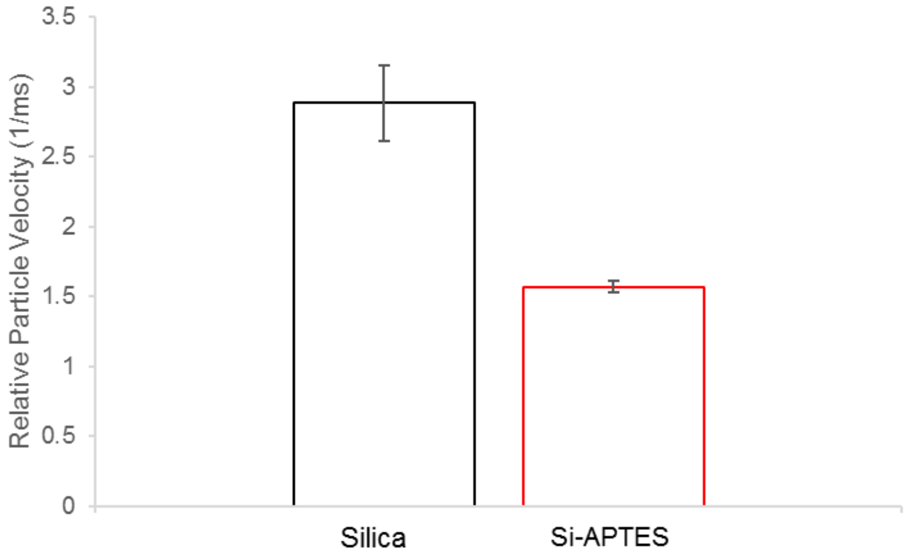

Figure 3.4 Change in translocation velocity for silica nanoparticles modified with APTES. Solution ~pH 7, 50 mM KCl. using a NP200 pore, 47 mm stretch. Error bars represent the standard deviation from three experiments.

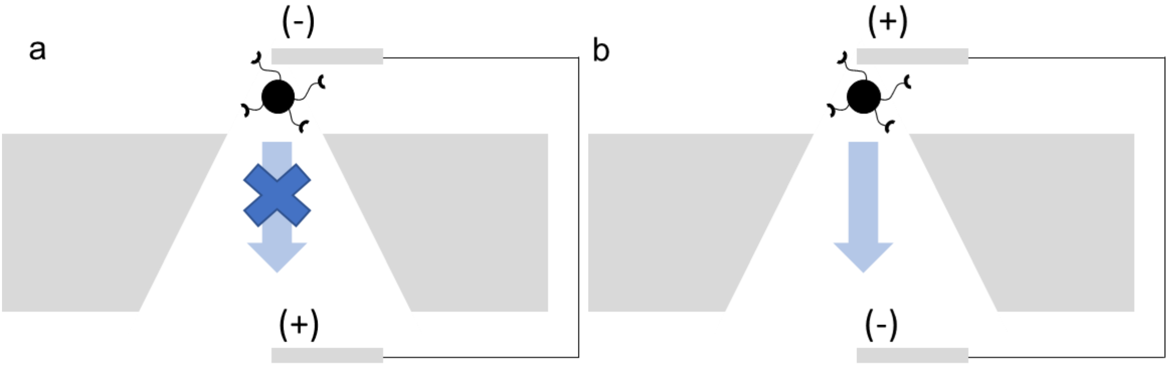

Figure 3.5 Schematic of silica NPs modified with APTES a) no translocation events are recorded with a positive bias. b) Bias changed to negative and translocation events recorded.

3.4.3 Silica Nanoparticle Velocity

The speed at which the particles traverse the pore can be related to the surface charge.[2] As above, this is dominated by the negative silica surface; or in later experiments by the amine terminated ligand. The purchased silica was analysed using TRPS. The particles have a net negative charge at pH 7 and travel towards the anode with a positive potential applied to the system. The particle velocity is denoted as ms^{-1} and is the time taken for the particle to travel 50 % of the way through the sensing zone of the pore.

3.4.3.1 Ionic Strength

Changing the electrolyte concentration, changes the ionic strength, I, of the system. The measured velocity is related to the particles electrophoretic mobility which is a function of the double layer fluctuation, see equation 2.9 in chapter 2. Table 3.2 shows how the Debye length changes with the ionic strength of potassium chloride.

Table 3.2 Debye lengths for the potassium chloride concentrations used for silica nanoparticle analysis.

Debye Length (nm)	Ionic Strength (mM)
6.79	2
4.29	5
1.35	50
0.99	100

Table 3.3 Ionic strength with conductivity values of electrolytes used.

Electrolyte	Ionic Strength (mM)	Conductivity (mS)
2 mM KCl	2	0.72
5 mM KCl	5	1.32
50 mM KCl	50	6.45
100 mM KCl	100	11.34

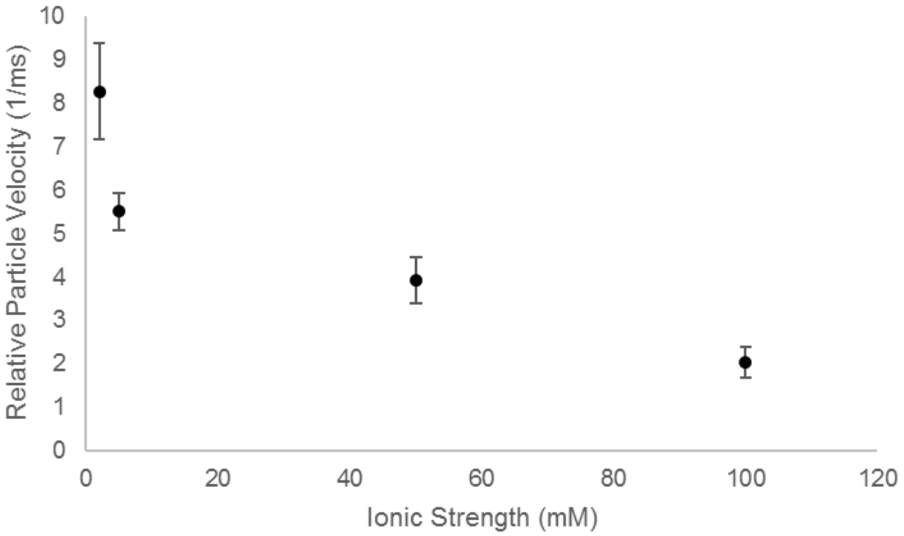

Figure 3.6 Change in translocation velocity for silica nanoparticles with increasing ionic strength. Solution ~pH 7, using a NP200 pore, 47 mm stretch. Error bars represent the standard deviation from three experiments.

Figure 3.6 shows the average velocities for silica particles across a range of different electrolyte concentrations. As the concentration of the supporting electrolyte is lowered the particle velocity for the bare silica particles increases from 2 ms^{-1} to

~8.2 ms^{-1} in 100 mM and 2 mM KCl respectively. As the double layer increases, there is less shielding around the particles charge.

3.4.3.2 pH

Changes in pH can change the surface charge of a particle by protonating or deprotonating groups on the nanoparticle surface. Silica nanoparticles were analysed over a pH range ~ 3-7, Figure 3.7. pH above 7 was not explored further due to objective of sensing copper, which would precipitate out of solution above this pH.[10] Varying the pH had little effect on the silica nanoparticles and remains negative over the pH range 3-7. Silica nanoparticles have a negative zeta potential over a wide range of pH due to the deprotonated silanol groups.[6] This agrees with the result shown in Figure 3.6, relative particle velocity is directly related to the particles zeta potential.[2]

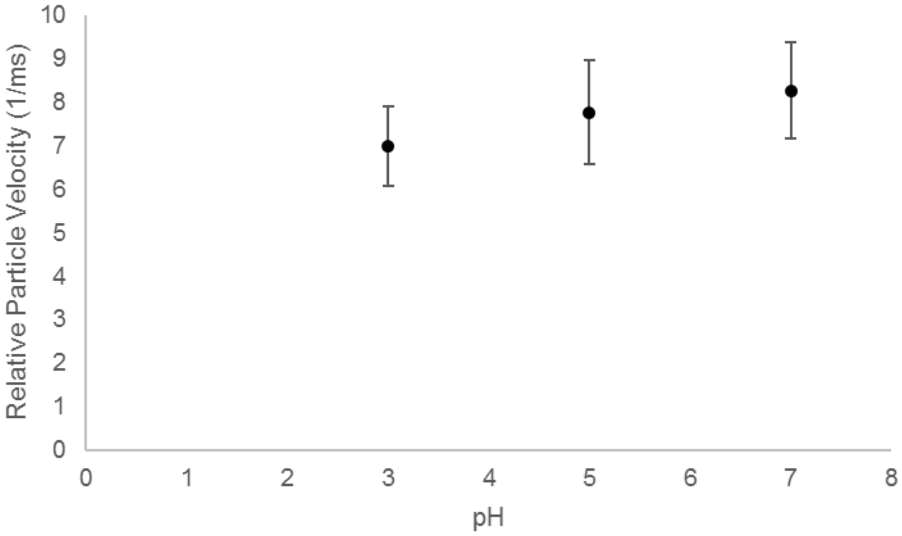

Figure 3.7 Change in silica nanoparticle speed with changing pH, in 2mM KCl. Analysed on a NP200 pore, 47 mm stretch, 1.60 V. Error bars represent the standard deviation from three experiments.

3.4.4 Silica-APTES Nanoparticles

3.4.4.1 Ionic Strength

Upon having their surfaces changed with the APTES the particles appear to have a small net positive surface charge at pH 7, likely to be due to the protonation of the amine, and travel to the cathode. When a positive potential was applied, and the anode was placed inside the pore no translocation events were observed. In contrast to the bare silica beads, the velocity of the APTES modified beads remains unchanged across the different ionic strengths going from 2 ms^{-1} to 2.8 ms^{-1} in 100 mM and 2 mM KCl respectively, again attributed to the low charge on the APTES ligand, Figure 3.8.

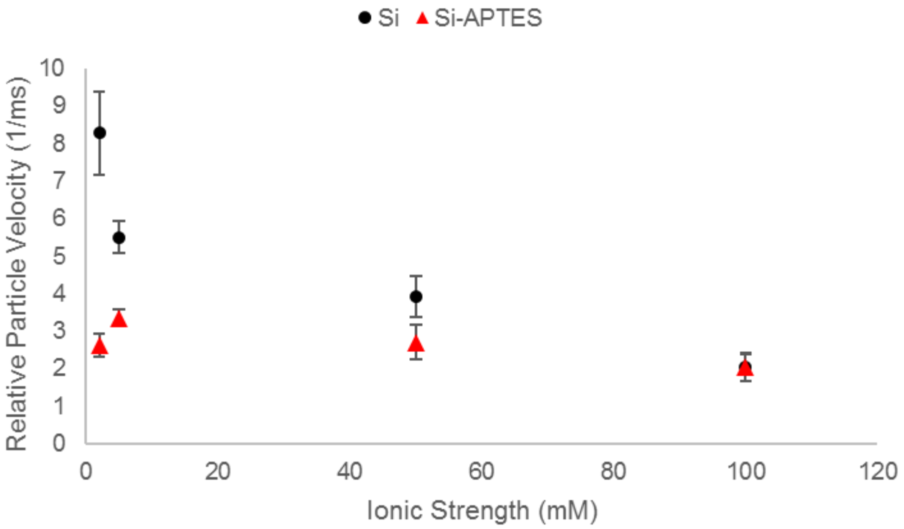

Figure 3.8 Change in translocation velocity for silica-APTES nanoparticles (red triangles) with increasing KCl concentration. The silica nanoparticles (black circles) are repeated for comparison. Solution pH ~7 using a NP200 pore, 47 mm stretch. Error bars represent the standard deviation from three experiments.

3.4.4.2 pH

As expected the charge on the primary amine can be controlled by varying the pH, shown in Figure 3.9. The pKa of APTES has been reported to be between 3.9-6.5 therefore at an acidic pH, the number of protonated amines increases, Scheme 3.3, increasing the velocity of the particle. The Si-APTES particles have $-NH_2$ surface groups which may bear a net positive, neutral or negative charge, depending on pH. The overall net charge of the particle increases as pH decreases due to the formation of $-NH_3^+$ groups present on the particles surface which is seen as an increase in particle velocity through the nanopore, Figure 3.8. Zeta potential measurements of APTES modified silica show the zeta potential decreasing considerably between pH 5 and 7 from ~25 mV to ~-25 mV,[9,11] this corresponds with data shown in Figure 3.9, the velocity of the particle decreases from ~13 ms^{-1} to ~2 ms^{-1} over the same pH range. The velocity of the particles recorded are related to the particles zeta potential and demonstrates the use of TRPS to analyse changes on the nanoparticles surface.

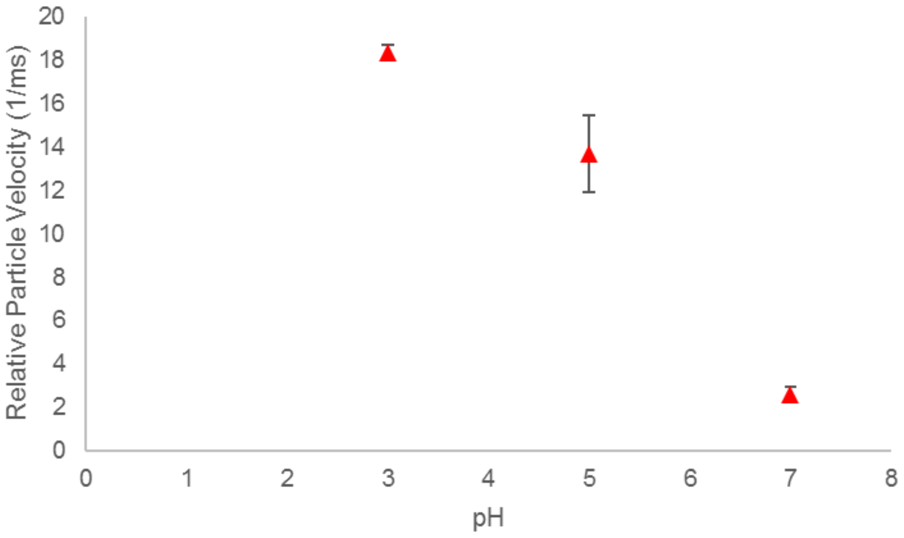

Figure 3.9 Change in translocation velocity of Si-APTES nanoparticles with increasing pH. Measured in 2 mM KCl, NP200 pore, 47 mm stretch and -3.18 V. Error bars represent the standard deviation from three experiments.

Scheme 3.3 Protonation of the amine group present on the nanoparticles surface.

A benefit of the TRPS system is the Particle-by-Particle analysis. Figure 3.10provides the distribution of velocities for the APTES modified particles. As well as observing a shift in the mean velocity from 2 ms^{-1} to 18 ms^{-1} in solution pH 7 and 3 respectively, a broadening and change in the distribution is also observed with median skewness going from 0.57, 0.33 and -0.05 for pH 7, 5 and 3 respectively. This distribution of the data set represents the ability to resolve the difference in velocities of the particles that arise from the non-uniform distribution of APTES ligands on the particles surface, i.e. it is not expected that each particle will have the same number of APTES ligands on their surface and therefore the same velocity.

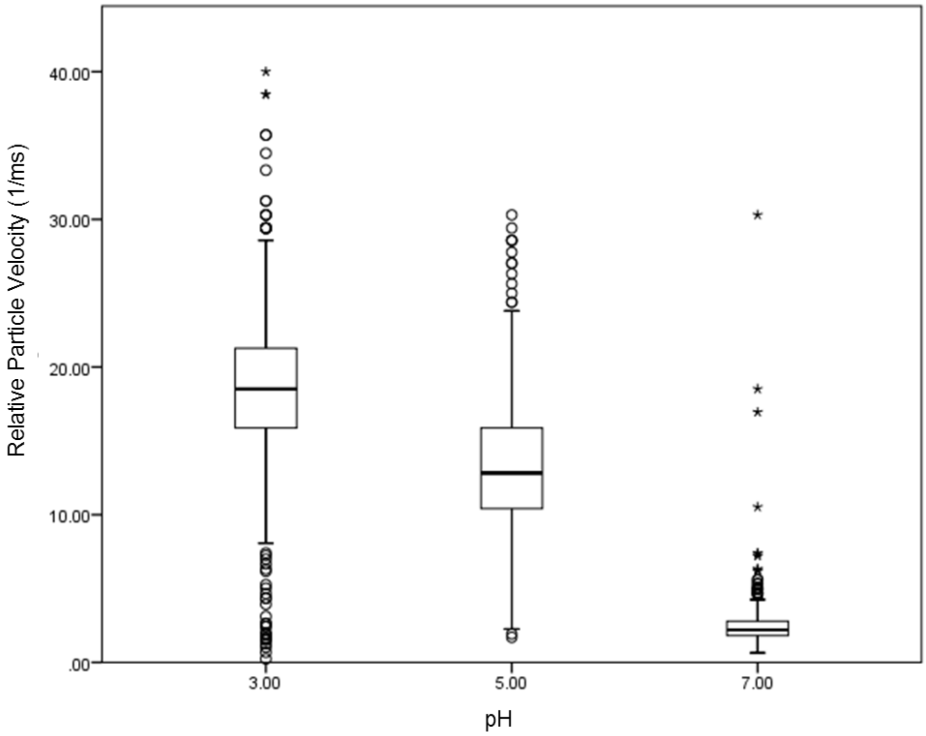

Figure 3.10 Boxplot of Silica-APTES particle velocity as a function of pH. Measured in 2 mM KCl, NP200 pore, 47 mm stretch and -3.18 V.

3.4.5 Carboxyl Nanoparticles

Carboxyl nanoparticles were used to immobilise DNA on to the surface of the nanoparticle via EDC coupling chemistry. Superparamagnetic particles were purchased with carboxyl groups on the surface. Using magnetic particles in the assay allows for easy separation of the particles from the solution by using a magnet.[2,12-14]

3.4.5.1 Ionic Strength

For EDC coupling chemistry to work, carboxyl groups are needed on the particles surface. To ensure a high density of carboxy groups the particles were modified with polyelectrolytes. To introduce a facile method for modifying the surface chemistry of the particles a layer-by-layer (LbL), assembly using PAAMA/ PEI was investigated. This system is well studied having been previously used to modify a range of materials.[14-19] The nanoparticles were coated with two polyelectrolytes, PEI and followed with PAAMA, shown in Figure 3.11.[15]

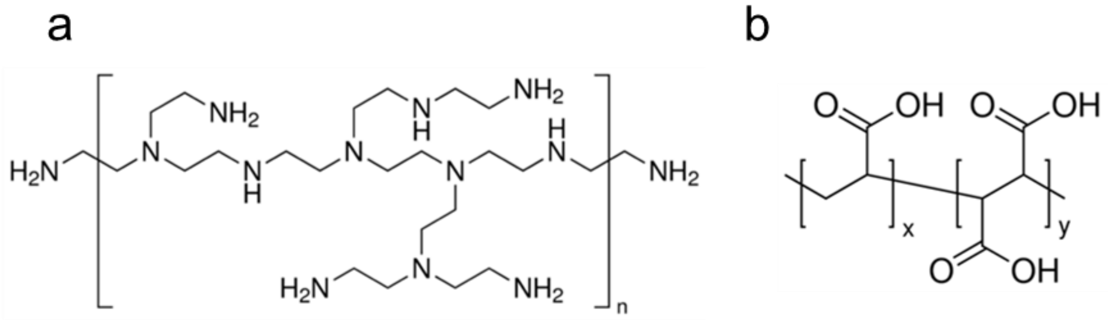

Figure 3.11 Polyelectrolytes a) poly(ethyleneimine) (PEI) and b) poly(acrylic acid-co-maleic acid) (PAAMA).[8]

After being modified with the both the PEI and PAAMA, the particles were analysed by TRPS in the same electrolytes as the previous experiments. The carboxylated particles were placed in the instrument and a positive potential applied. Blockade events were recorded, and the particles translocation velocities were recorded, Figure 3.12, across the range of ionic strengths. The particle velocities increase with decreasing ionic strength, this indicates the particles have a negative surface charge which is due to the presence of carboxyl groups.

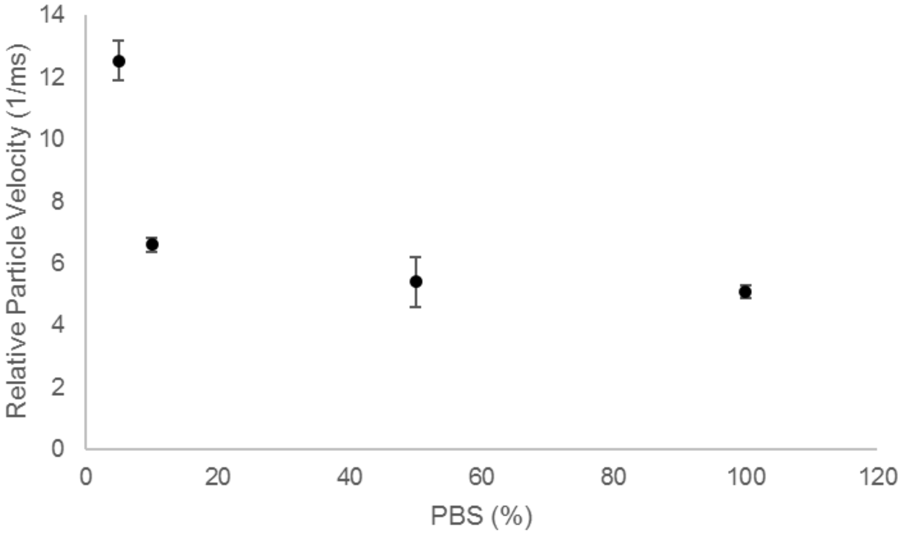

Figure 3.12 Change in translocation velocity of polyelectrolyte coated nanoparticles with decreasing ionic strength. Measured in pH 7.4 using a NP200 pore at 45.26 mm. Error bars represent one standard deviation from the mean of three samples.

The modified carboxyl nanoparticles are used in all following experiments, unless stated otherwise. The carboxyl particles were analysed in a range of ionic strengths, listed in Table 3.4.

Table 3.4 Ionic strengths with conductivity values of electrolytes used to analyse carboxyl nanoparticles.

Electrolyte	Ionic Strength (mM)	Conductivity (mS)
PBS	171.5	13.24
50 % PBS	85.75	7.22
10 % PBS	42.88	2.83
5 % PBS	21.44	1.72

3.4.5.2 DNA Modification

Following the modification of the nanoparticles, amine tagged DNA can be grafted to the particles via EDC coupling chemistry, shown in Scheme 3.4

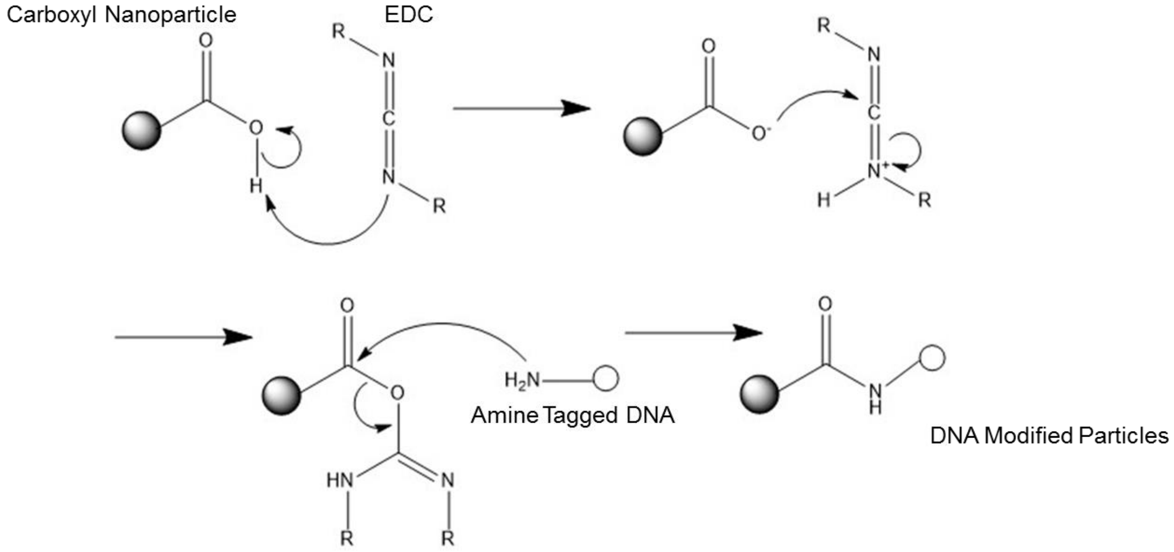

Scheme 3.4 Mechanism for EDC coupling chemistry used for the modification of carboxyl nanoparticles with DNA.

The particles were modified with the amine modified DNA sequence and the particles were analysed in the range of ionic strengths. An excess of DNA was added to ensure the beads were fully covered. The conditions of TRPS were matched to the previous experiments, any changes in velocity can then be attributed to changes in the particles electrophoretic mobility.

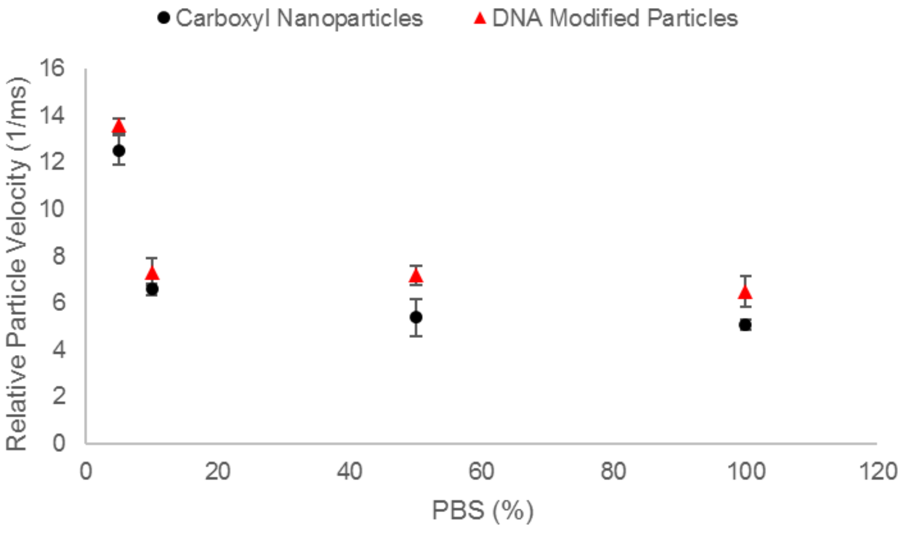

Figure 3.13 Change in translocation velocity of DNA modified particles (red triangles) compared with carboxyl particles (black circles). Measured in pH 7.4 using a NP200 pore at 45.26 mm. Error bars represent one standard deviation from the mean of three samples.

The particles with DNA attached were compared to those without (blank particle). The particles modified with DNA increased in velocity compared to the blank run under the same conditions, Figure 3.13. The changes in the particle velocity can be attributed to the change in the particles charge. This is due to the charge from the negative phosphate backbone on the DNA, therefore the charge density around the particle has increased and the particle traverses the pore at a greater velocity. The increase in velocity is only small and it would be expected that the particles with DNA would traverse the pore at a considerably higher velocity due to the contribution from the negative phosphate backbone. Low mobility of highly charge particles though nanopores has been reported previously.[20] The highly charged nature of the particle can lead to polarisation of the double layer when traversing the pore which may slow the particle translocation through the pore.[20] The small increase in particle velocity can be used to confirm the modification of the carboxyl nanoparticles with DNA.

3.4.5.3 pH

The carboxyl groups on the surface of the nanoparticle can be protonated or deprotonated depending on the pH of the solution. The carboxyl groups present will dissociate depending on the pH of solution. This will change the charge on the particle and will change the particles velocity through the pore. Figure 3.14 shows the lowering the pH of the electrolyte, slows the translocation of the particle. The -COOH group will dissociate to form -COO$^-$ as the pH of the electrolyte is increased, the particles will therefore have an overall negative net charge. Decreasing the pH will protonate the carboxyl groups on the particles surface and reducing the overall net charge on the particle. Zeta potential measurements of PEI/PAAMA coated particle have previously been reported with particles displaying a high negative zeta potential across a range of pH.[15] The change in pH changes the charge on the particle and thus its zeta potential and particle velocity, Figure 3.14.

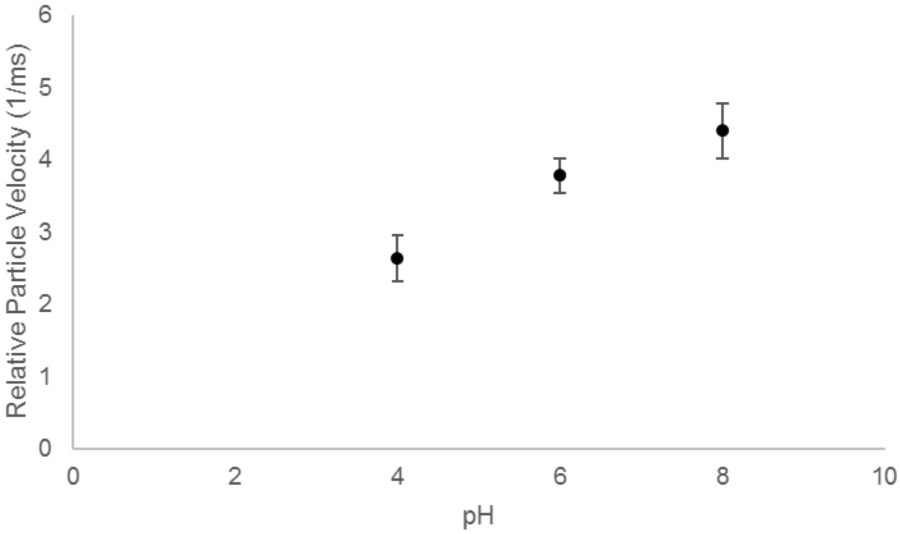

Figure 3.14 Change in translocation velocity of carboxyl nanoparticles as a function of pH. Measured on a NP200 pore in 500 mM NaCl at 0.08V and 45.50 mm stretch.

The same trend is observed for DNA modified particles, Figure 3.15. As the pH is lowered the DNA base pairs can become protonated which will change the charge on the particles surface. Lowering the pH, slows the particles translocation through the pore which is an indication of groups becoming protonated. When altering the pH, the charge on the pore also needs to be considered. The translocation of the particles through the pore is also dependent upon the surface charge of the pore. As the pH of the electrolyte is changed the charge of the pore will change. This in turn will alter the electroosmotic flow through the pore, equation 2.7 Chapter 2, and alter the particles velocity.

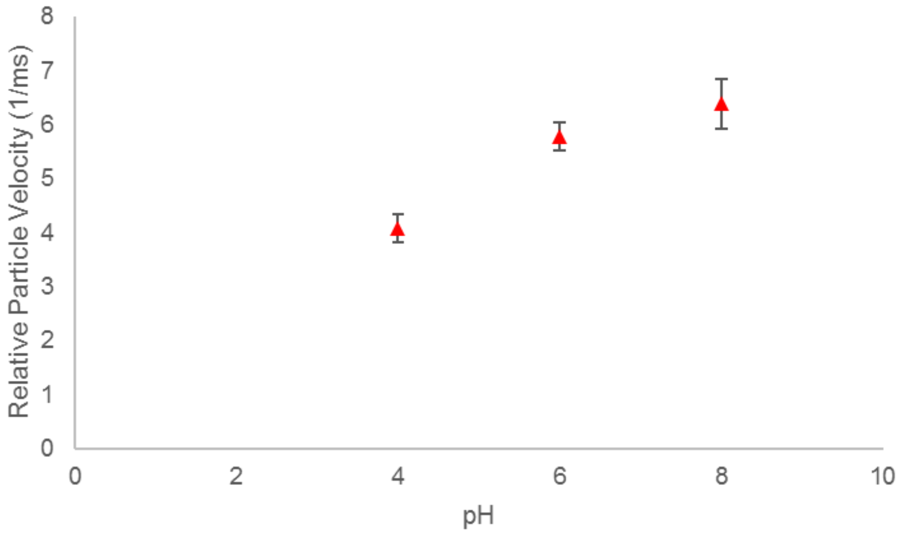

Figure 3.15 Change in translocation velocity of DNA modified nanoparticles as a function of pH. Measured on a NP200 pore in 500 mM NaCl at 0.08 V and 45.50 mm stretch.

3.5 Conclusions

The work presented in this chapter demonstrates how double layer theory can be applied to measuring changes on a particles surface via particle velocity through a nanopore. The nanoparticles used in this chapter are used throughout the thesis and this chapter demonstrates that TRPS can be used to characterise the nanoparticles prior to a metal ion sensing assay. The work presented shows how ionic strength and pH can be tuned to alter the particle's velocity. Silica nanoparticles and carboxyl coated nanoparticles velocities were shown to increase by reducing the ionic strength. Upon having their surfaces modified the resulting particle velocities differed and this signal can be used to confirm a successful modification. The silica nanoparticles and APTES modified particles were easily distinguished due to the polarity in which the particles traversed the pore. Carboxyl and DNA modified particles were then distinguished by an increase in velocity upon DNA being attached to the particles surface. , The particles in this chapter have functional groups, -COOH and $–NH_2$, that can be protonated/deprotonated. The subsequentnet net charge of the particle changed, which resulted in changes in particle velocity. Understanding how the double layer changes with ionic strength and pH is essential in designing a metal ion sensor based on the velocity of the particle through the pore. This chapter demonstrates the ability for TRPS to detect changes on a nanoparticles surface via particle velocity and we now have confidence that TRPS could be used to monitor metal ion binding to the surface of nanoparticles.

3.6 References

1. Holt, J. D. *PhD Thesis,* Loughborough University (2014)

2. Blundell, E. L. C. J., Vogel, R. & Platt, M. Particle-by-Particle Charge Analysis of DNA-Modified Nanoparticles Using Tunable Resistive Pulse Sensing. *Langmuir* **32,** 1082–1090 (2016).

3. Stöber, W. & Fink, A., Controlled Growth of Monodisperse Silica Spheres in the Micron Size Range. *J. Colloid Interface Sci.***26,** 62-69 (1968)

4. Nozawa, K. *et al.* Smart control of monodisperse stober silica particles: Effect of reactant addition rate on growth process. *Langmuir* **21,** 1516–1523 (2005).

5. Soto-Cantu, E., Cueto, R., Koch, J. & Russo, P. S. Synthesis and rapid characterization of amine-functionalized silica. *Langmuir* **28,** 5562–5569 (2012).

6. Kim, K. M. *et al.* Surface treatment of silica nanoparticles for stable and charge-controlled colloidal silica. *Int. J. Nanomedicine* **9,** 29–40 (2014).

7. Yamaura, M. *et al.* Preparation and characterization of (3-aminopropyl)triethoxysilane-coated magnetite nanoparticles. *J. Magn. Magn. Mater.* **279,** 210–217 (2004).

8. Haller, I. Covalently attached organic monolayers on semiconductor surfaces. *J. Am. Chem. Soc.* **100,** 8050–8055 (1978).

9. Bini, R. A., Marques, R. F. C., Santos, F. J., Chaker, J. A. & Jafelicci, M. Synthesis and functionalization of magnetite nanoparticles with different amino-functional alkoxysilanes. *J. Magn. Magn. Mater.* **324,** 534–539 (2012).

10. Hidmi, L. & Edwards, M. Role of temperature and pH in $Cu(OH)_2$ solubility. *Environ. Sci. Technol.* **33,** 2607–2610 (1999).

11. Römhildt, L., Gang, A., Baraban, L., Opitz, J. & Cuniberti, G. High yield formation of lipid bilayer shells around silicon nanowires in aqueous solution. *Nanotechnology* **24,** 355601 (2013).

12. Billinge, E. R. & Platt, M. Multiplexed, label-free detection of biomarkers using aptamers and Tunable Resistive Pulse Sensing (AptaTRPS). *Biosens. Bioelectron.* **68,** 741–748 (2015).

13. Billinge, E. R., Broom, M. & Platt, M. Monitoring Aptamer − Protein Interactions Using Tunable Resistive Pulse Sensing. *Anal. Chem.* **86,** 1030–1037 (2014).

14. Steitz, B. *et al.* Characterization of PEI-coated superparamagnetic iron oxide nanoparticles for transfection: Size distribution, colloidal properties and DNA interaction. *J. Magn. Magn. Mater.* **311,** 300–305 (2007).

15. O'Mahony, J. J., Platt, M., Kilinc, D. & Lee, G. Synthesis of Superparamagnetic Particles with Tunable Morphologies: The Role of Nanoparticle–Nanoparticle Interactions. *Langmuir* **29,** 2546–2553 (2013).

16. Yang, Y.-H., Haile, M., Park, Y. T., Malek, F. A. & Grunlan, J. C. Super Gas Barrier of All-Polymer Multilayer Thin Films. *Macromolecules* **44,** 1450–1459 (2011).

17. Fu, J. *et al.* pH-Amplified Exponential Growth Multilayers: A Facile Method to Develop Hierarchical Micro- and Nanostructured Surfaces. *Langmuir* **25,** 672–675 (2009).

18. Yang, Y.-H., Bolling, L., Haile, M. & Grunlan, J. C. Improving oxygen barrier and reducing moisture sensitivity of weak polyelectrolyte multilayer thin films with crosslinking. *RSC Adv.* **2,** 12355–12363 (2012).

19. Podsiadlo, P. *et al.* Exponential Growth of LBL Films with Incorporated Inorganic Sheets. *Nano Lett.* **8,** 1762–1770 (2008).

20. Qiu, Y., Yang, C., Hinkle, P., Vlassiouk, I. V. & Siwy, Z. S. Anomalous Mobility of Highly Charged Particles in Pores. *Anal. Chem.* **87,** 8517–8523 (2015).

4 Modification of particle charge: Applications in heavy metal detection

Work presented in this chapter demonstrates that the translocation speed, conductive and resistive pulse magnitude, can be used to infer the surface charge of a nanoparticle, and act as a specific transduction signal for the binding of metal ions to ligands on the particle surface. The modified silica nanoparticles characterised in Chapter 3 were used to extract copper (II) ions ($Cu^{2+)}$ from solution. By tuning the pH and ionic strength of the solution, a biphasic pulse, a conductive followed by a resistive pulse is recorded. Biphasic pulses are becoming a powerful means to characterise materials, and provide insight into the translocation mechanism, and the work demonstrates their first use to detect the presence of metal ions in solution. THE combinations of translocation speed and/or biphasic pulse behaviour are used to detect Cu^{2+} with quantitative responses across a range of pH and ionic strengths. Using a generic ligand this assay allows a clear signal for Cu^{2+} as low as 1 ppm with a short 5-minute incubation time, and is capable of measuring 10 ppm Cu^{2+} in the presence of 5 other ions. The method has potential for monitoring heavy metals in environmental samples. Parts of this chapter were published "A tunable nanopore sensor for the detection of metal ions using translocation velocity and biphasic pulses", *Nanoscale*, 2016, **8**, 19139.

4.1 Aims and Objectives

This chapter aims to develop work presented in Chapter 3 further by studying the binding on a metal ion to the surface of the nanoparticle. Chapter 3 demonstrated the ability to use TRPS to study changes on the nanoparticle surface via particle velocity, and this chapter aims to use the same technique to detect the metal ion binding to APTES modified silica nanoparticles. Experiments were carried out to detect Cu^{2+} over a range of pH, ionic strength and with competing metal ions present.

4.2 Introduction

Nanomaterials designed for the extraction and/or detection of heavy metal ions in solution have gained considerable interest in recent years. Such materials can include carbon nanotubes,[1,2] nanorods[3] and nanoparticles of copper[4], gold,[5] magnetic,[6] and silica.[7] These systems can be designed to produce a signal upon binding to the metal ion or integrated into detection platforms such as atomic adsorption,[8–11] electrochemical assays,[1,12,13] fluorescence[4,14] and colorimetric sensors[15,16]. Whilst each technology platform has its merits, not all are portable, simple to use/interpret and can require expensive equipment and/or additional gas/carrier liquids.

Conical nanopores, as used within TRPS, exhibit ionic rectification properties.[17–20] The charge on the pore wall creates areas of ion accumulation and depletion within the pore depending on the applied polarity.[19,21–23] This leads to the current being higher at one voltage compared to the voltage of opposite polarity, often expressed as the rectification ratio. In the simplest setup, i.e. the absence of any nanoparticles, the rectification ratio has been used to measure the concentration of metal ions as they interact with the pore wall itself.[24] However these assays are limited to one analyte and longer assay times. The use of nanoparticle based systems may allow for multiplexed assays and faster reaction times.[25,26] The addition of charged particles into a pore exhibiting rectification behaviour is however more complex. White and co-workers demonstrated that a negatively charged particle passing through a pore with a negative surface charge can create a conductive pulse prior to the resistive pulse at a negative polarity.[27] Conversely a positive particle under the same conditions will only generate a resistive pulse, due to an increased ion depletion effect. Other groups study this by demonstrating how the resistive pulse magnitude is also dependent on particle surface charge.[28,29]

This Chapter demonstrates that the waveshape and the velocity of the particle can be related to the particles surface charge and is used to detect the metal ion on the surface of the nanoparticle, Figure 4.1. This chapter focuses on copper which is a heavy metal monitored in drinking water, and set at a 2 ppm limit by the World Health Organisation (WHO).[30] Copper is an essential transition metal in biology, from cofactors in metabolic reactions,[31] free radical scavengers, to cell receptors and reporters. Its poor regulation can affect liver damage and be a biomarker for dementia.[32]

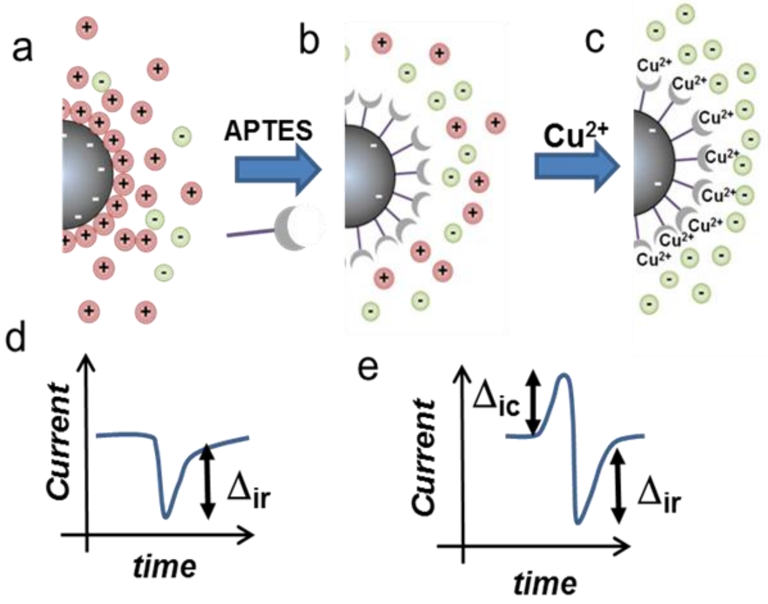

Figure 4.1 a) Schematic of the double layer around a 150 nm silica nanoparticles. b) A modified nanoparticle with APTES, c) Modified nanoparticle with Cu^{2+} copper bound to APTES. d) Representation of a resistive pulse, Δ_{ir}, e) Schematic of a double pulse, a conductive, Δ_{ic}, followed by resistive pulse.

4.3 Experimental

4.3.1 Method and Materials

The following chemicals were purchased from Sigma Aldrich, UK, silica nanoparticles, SiNPs, (150 nm in diameter, 5 % wt, 56799), (3-aminopropyl)triethoxysilane (APTES, ≥ 98 %, A3648), magnesium (II) chloride ($MgCl_2$, powder, <200 μm, 208337), copper (II) chloride dehydrate ($CuCl_2.2H_2O$, reagent grade, 221783), iron (II) chloride tetrahydrate ($FeCl_2$. $4H_2O$, 98 %, 220299). The following chemicals were purchased from Fisher Scientific, UK, Potassium chloride (KCl, >99%, P/4240/60), potassium hydroxide (KOH, 0.1 M, >85%, P/5600/60), calcium chloride ($CaCl_2$, general purpose grade, C/1400/60) and sodium chloride (NaCl, analytical grade, S/3160/60). Hydrochloric acid (HCl, 0.5 M, 37%) was purchased from VWR, UK. All reagents were used without further purification and all solutions were prepared in deionised water with a resisitivity of 18.2 MΩ cm (Maxima). Prior to analysis the pH of the solution was measured using a Mettler Toledo easy five pH meter with a Mettler Toledo InLab micro electrode.

4.3.2 Metal Ion Extraction

A copper (II) solution (1000 ppm) was prepared from $CuCl_2.H_2O$. The solution was diluted further to give a range of copper concentrations (0.1 – 100 ppm). A range of metal ion solutions were prepared from $MgCl_2$, $FeCl_2.4H_2O$, $CaCl_2$ and NaCl at a 10 ppm concentration. A solution containing magnesium (II), iron (II), calcium (II), sodium (I) and copper (II), with each metal ion at a 10 ppm concentration, was prepared. To the solutions, Si-APTES particles were added to give an end concentration of the particles in the solution of 1 $mgmL^{-1}$. The solutions were vortexed and sonicated to ensure the particles were fully dispersed and left for 24 hr before analysis. The pH of copper solutions (10 ppm) were altered to 3.4, 5.2 and 7.0, the modified particles were incubated in the three solutions for 24 hr before analysis. To a range of copper (II) solutions, the modified particles were incubated for a shorter period and analysed after 5 min. pH measurements on each solution were taken before and after the metal extraction.

4.3.3 Tunable Resistive Pulse Sensing

All measurements were conducted using the qNano (Izon Sciences Ltd, NZ) combining tunable nanopores with data capture and analysis software, Izon Control Suite v.3.1. Analysis of the conductive pulses generated was performed using Clampfit

10 software. The lower fluid cell always contains the electrolyte (75 µL) that the particle is suspended in and the upper fluid cell contains 40 µL of sample. Prior to TRPS analysis, all samples were vortexed for 30 s and sonicated for 2 minutes. During each sample run, the system was washed by placing 40 µL of the run electrolyte into the upper fluid cell several times with various pressures applied to ensure there were no residual particles remaining and therefore no cross contamination between samples.

4.3.4 ICP-OES Analysis

Inductively coupled plasma- optical emission spectroscopy (ICP-OES, Thermo Scientific iCAP 6000 series) was used to determine the copper concentrations in each solution. Eight copper calibration standards (0-100 ppm) were made using a 1000 ppm Cu standard solution and acidified with nitric acid (HNO_3, 0.2%). A calibration graph was completed before the samples were run.

The concentration of copper in solution was measured before and after the silica-APTES incubation. The copper solutions (10 mL) were filtered using a 0.22 µm membrane filter and acidified (0.2% HNO_3), three repeats were measured of each solution.

4.3.5 SEM Analysis

Scanning electron microscopy- energy dispersive X-ray spectroscopy (SEM-EDX) analysis was performed on the nanoparticles. Samples were placed on aluminium stubs and the electrolyte evaporated to leave a solid. EDX analysis was performed using a JOEL 7100F Field Emission Scanning Electron Microscope.

4.4 Results and Discussion

Silica nanoparticles were modified with APTES, shown in Chapter 3. From previous work carried out at Loughborough University by James Holt, silica modified with APTES has been shown to be able to extract Cu^{2+} from aqueous solutions.[33-36] We used to same process to first extract the Cu^{2+} ions from solution. The hypothesis being that the binding of the metal ion could be analysed by TRPS.

4.4.1 Ionic Strength

The translocation velocities of the particles were measured using TRPS before and after the incubation with Cu^{2+} ions. All velocities reported are recorded at $1/T_{0.5}$. The Si-APTES nanoparticles were incubated with 10 ppm Cu^{2+} for 24 hrs at pH ~7 and analysed in a range of electrolyte concentrations, Figure 4.2. The Si-APTES data from Figure 3.8 is replicated here, Experiments with and without copper were conducted in parallel to each other. The TRPS was set up so a negative potential was applied, and the particles travel towards the cathode underneath the pore. In high electrolyte concentrations (50 – 100 mM) the change in the velocity are negligible, this is attributed to the high shielding of the particles charge arising from a small Debye length. As the ionic strength is lowered, the double layer thickness increases therefore the shielding decreases around the particles charge and the particles with Cu^{2+} traverse the pore with a greater velocity, shown in Figure 4.2. The velocity of the particle increases with decreasing ionic strength, suggesting the Cu^{2+} ions have added charge to the particles surface and are no longer neutral at pH ~7. The Cu^{2+} was being extracted by the Si-APTES nanoparticles and the concentration analysis of the Cu^{2+} was measured using Inductively coupled plasma- optical emission spectroscopy (ICP-OES). The starting SiNPs before modification with the APTES were incubated with Cu^{2+} at pH 7, Figure 4.3. There was no change in velocity for the particles after incubation with Cu^{2+}. The change in velocity in Figure 4.2 is due to the binding of Cu^{2+} to the APTES ligands.

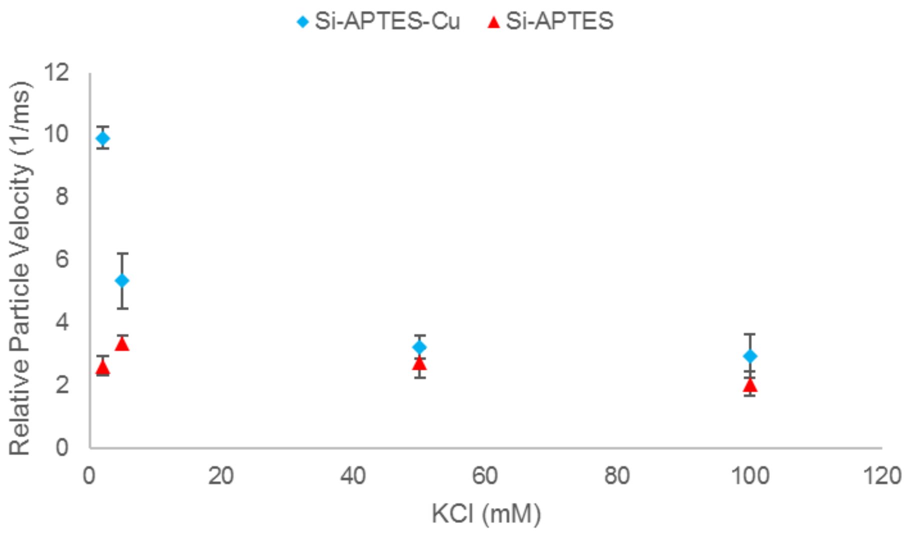

Figure 4.2 Silica-APTES nanoparticles (red triangles) incubated with 10 ppm Cu (II) for 24 hr (blue diamonds). Samples run on a NP200 pore, pH ~ 7, stretch 46.50 mm. Error bars represent the standard deviation of three experiments.

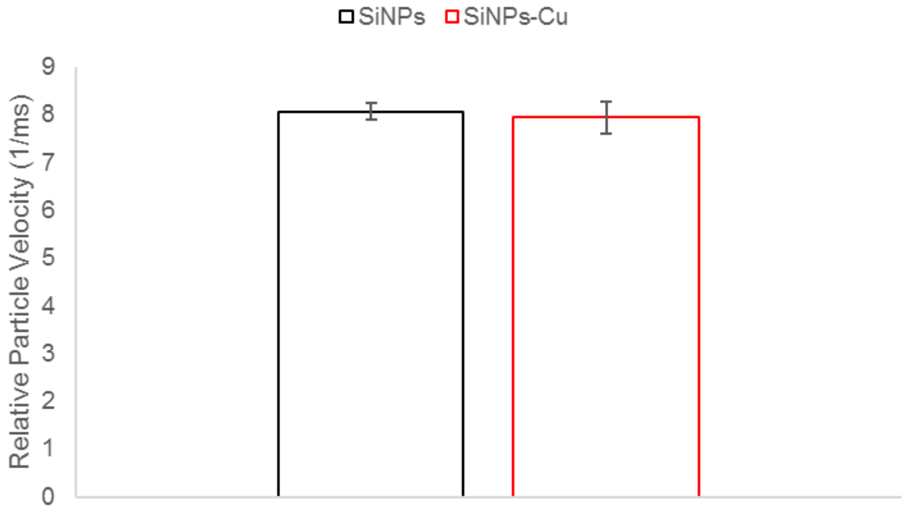

Figure 4.3SiNPs incubated with 10 ppm Cu (II) for 24 hr. The particle velocity was measured before and after incubation. Samples run on a NP200 pore, pH ~ 7, stretch 46.50 mm. Error bars represent the standard deviation of three experiments.

4.4.1.1 ICP-OES

ICP-OES is a common technique used to detect trace elements and is used routinely in detecting heavy metals in solution. The plasma is a macroscopically neutral ionized gas. External energy, in the form of an electrical field is used to ionise the gas and maintain the plasma.[37] The inductively coupled plasma source is comprised of a plasma torch, radio frequency (RF) coil and a RF power supply. The gas used to create the plasma is argon. Argon is commonly used to produce the plasma because like any noble gas, it is monoatomic with a high ionisation energy (15.76 eV), is chemically inert and is the cheapest of the noble gases. Free electrons are introduced into plasma gas by a spark and electrons are accelerated by the field which ionises the argon gas.

$$Ar + e \rightarrow Ar^{+} + e + e$$

The argon ions recombine with electrons which lead to excited argon atoms.

$$Ar^{+} + e \rightarrow Ar^{*} + hv$$

Optical emission spectroscopy quantifies the measurement of the optical emission from excited atoms to determine analyte concentration. The analyte is introduced into the central channel of the ICP where they are de-solvated, vaporised and atomised by plasma. The analyte undergoes excitation into various energy states. Optical emission is the process in which an excited state radiatively decays with the spontaneous emission of a photon. The detector measures the intensity of the emitted light and the concentration of the element is calculated from the intensity.

Copper standards were run prior to the samples to produce a calibration curve which was used to calculate the concentration of copper in solution, Figure 4.4. The Si-APTES and SiNPS were incubated in 10 ppm copper (II) solutions for 24 hr before the solution was analysed by ICP-OES. The same set up was used in the presence of 2 mM KCl to show there is no interference from the electrolyte.

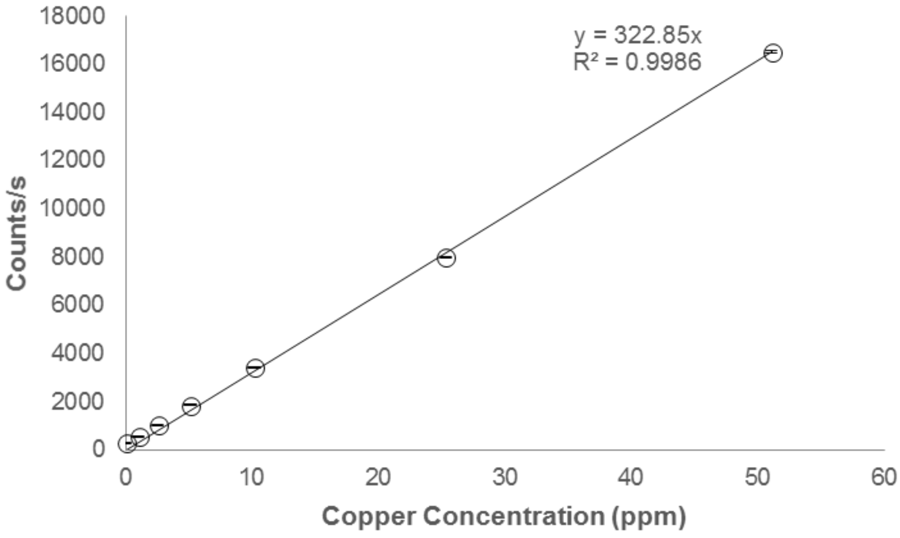

Figure 4.4 Calibration curve for copper concentration v counts per second. Error bar represent one standard deviation from the mean of three repeats.

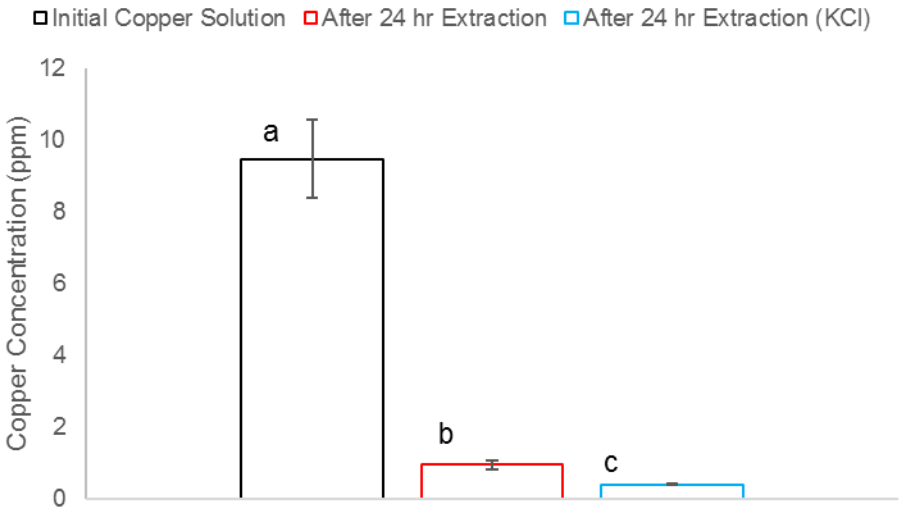

Figure 4.5 Concentration of copper a) before Si-APTES particles were incubated, b) after 24 hr incubation with the particles and c) after 24 hr incubation with the particles in the presence of 2 mM KCl. Error bars represent one standard deviation from the mean of three repeats.

The copper concentration measured in the solution after extraction, with and without KCl, drops below 1 ppm. The concentration analysis confirms the Si-APTES particles extract the copper ions from solution. pH measurements are taken before and after extraction, there was a very small change in pH indicating it was unlikely that the copper is precipitating out of solution. Figure 4.5 shows that the blank SiNPs extracted no copper from solution, this demonstrates the copper is binding to the APTES on the modified particles.

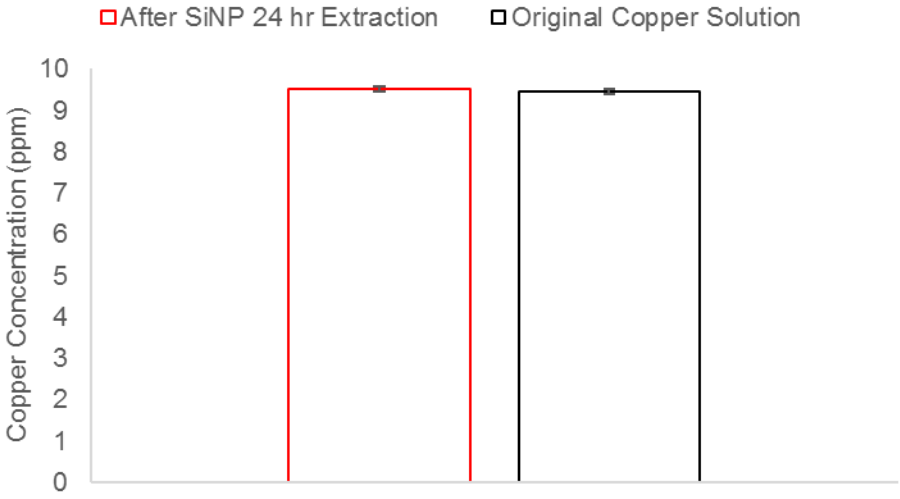

Figure 4.6 Concentration of copper before and after 24 hr incubation with SiNPs. Error bars represent one standard deviation from the mean of three repeats.

Table 4.1 pH measured of copper solutions before and after the incubation with Si-APTES nanoparticles.

Initial Solution pH	pH After Copper Extraction
3.32	3.40
5.41	5.93
7.01	6.88

4.4.1.2 Hard Soft Acid Base Theory

The binding of APTES to copper can be explained using the hard soft acid base (HSAB) theory.[38,39] The HSAB theory is commonly used in chemistry to explain the stability of metal complexes and their reaction pathways. The theory was first introduced by Ralph Pearson in the 1960s.[35] The terms hard and soft, acid and base refer to the chemical characteristics of species. Species with small ionic radii and are non-polarizable are referred to as hard, while species with large ionic radii and highly polarizable are referred to as soft. Hard acids prefer to bind to hard bases, forming ionic complexes and soft acids prefer to bind to soft bases to give covalent complexes.

Table 4.2 categorises species by their hard, soft or intermediate species according to Pearson[38] and Hancock *et al*.[39]

Table 4.2 Examples of hard, soft and borderline acids.[38,39]

Hard	Soft	Borderline
H^+, Li^+, Na^+, K^+	Cu^+, Ag^+, Au^+, Tl^+, Hg^+	Fe^{2+}, Co^{2+}, Ni^{2+}, Cu^{2+}, Zn^{2+}, Pb^{2+}
Be^{2+}, Mg^{2+}, Ca^{2+}, Sr^{2+}, Ba^{2+}	Pd^{2+}, Cd^{2+}, Pt^{2+}, Hg^{2+}	Sn^{2+}, Sb^{3+}, Bi^{3+}, Rh^{3+}, Ir^{3+}, $B(CH_3)_3$
Al^{3+}, Sc^{3+}, Ga^{3+}, Ln^{3+}, La^{3+}, Gd^{3+}, Lu^{3+}, Cr^{3+}, Co^{3+}, Fe^{3+}, As^{3+}	CH_3Hg^+, $Co(CN)_5^{2-}$,Pt^{4+}	$C_6H_2NH_2$, C_5H_5N, N_3^-, Br^-, NO_2^-
Pu^{4+}, Ce^{4+}, Wo^{4+}, Sn^{4+}	Te^{4+}, Br^+, I^+	N_2, SO_3^{2-}
UO^{2+}, VO^{2+}, MoO^{3+}	R_2S, RSH, RS^-, I^-, SCN	
H_2O, OH^-, F^-, $CH_3CO_2^-$, PO_4^{3-}	$S_2O_3^{2-}$, R_3P, R_3As, $(RO)_3P$	
SO_4^{2-}, Cl^-, CO_3^{2-}, ClO_4^-, NO_3^-	CN^-, RNC, CO, C_2H_4, H^-, R^-	
ROH, RO^-, R_2O, NH_3, RNH_2, NH_2NH_2		

Using Table 4.2 , the APTES ligand can be defined in to one of the categories. The APTES ligand is considered a hard base and copper (II) as borderline. In these experiments, it is assumed that copper (II) is behaving like a hard acid when interacting with the nitrogen groups.[40,41] HSAB can be used to explain the copper binding, however it has its limitations and is not comprehensive. HSAB cannot be used to predict which hard acid a hard base will bind to over another hard acid such APTES binding to copper (II) over potassium (I).

4.4.2 pH

The pH of real samples can be varied in environmentalsamples. Therefore, the next experiments measured the signal over a range of pH. The chosen electrolyte was 2 mM KCl. At this ionic strength, differences between the Si-APTES-Cu^{2+} particles and Si-APTES particles is the most prominent. Three solutions of copper (10 ppm) were prepared at pH ~3, 5 and 7. The Si-APTES particles were incubated in the solutions for 24 hr and analysed using TRPS. The nanoparticles incubated in the solutions at pH ~5 and ~7 showed a colour change within 5 minutes of being incubated with the copper solution. The nanoparticles changed from off white to blue, however no colour change was observed in pH ~3.

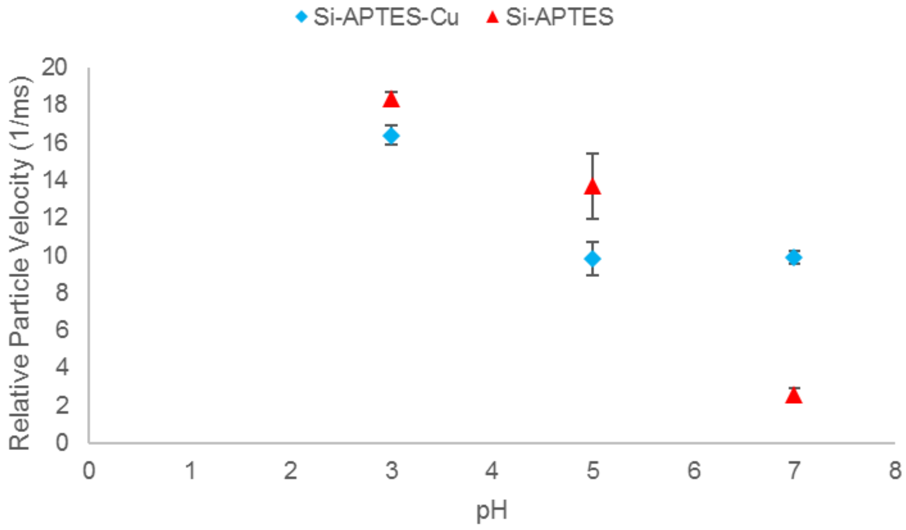

Figure 4.7 Translocation velocity of particles with and without copper as a function of pH. Samples analysed in 2 mM KCl on a NP200 pore, 47 mm stretch, -3.18 V.

The particle velocities were recorded in different pH, Figure 4.7. As the pH is lowered the differences in particle velocities between the blank and those with Cu^{2+} is reduced. As the pH is lowered, the amine group on the APTES ligand is protonated which inhibits the interaction between the Cu^{2+} and the amine group. As a colour change was observed at pH 5, and the particle velocities show a change, concentration analysis was carried out using ICP-OES to confirm the binding of Cu^{2+}.

4.4.2.1 ICP-OES

The copper standards were run prior to the samples to produce a calibration curve which was used to calculate the concentration of copper in solution, Figure 4.8. The Si-APTES was incubated in 10 ppm Cu^{2+} solution, pH ~5 for 24 hr before the solution was analysed by ICP-OES.

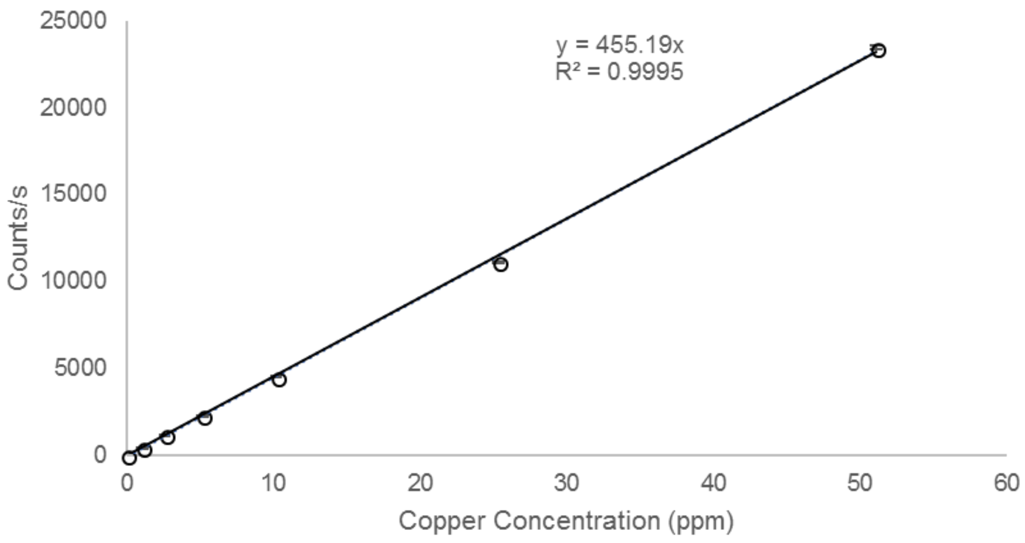

Figure 4.8 Calibration curve for copper concentration v counts per second. Error bar represent one standard deviation from the mean of three repeats.

The concentration of copper measured in solution after a 24 hr incubation with Si-APTES nanoparticles shows a significant decrease, Figure 4.9, this confirms that the nanoparticles have successfully removed copper from solution at pH ~5.

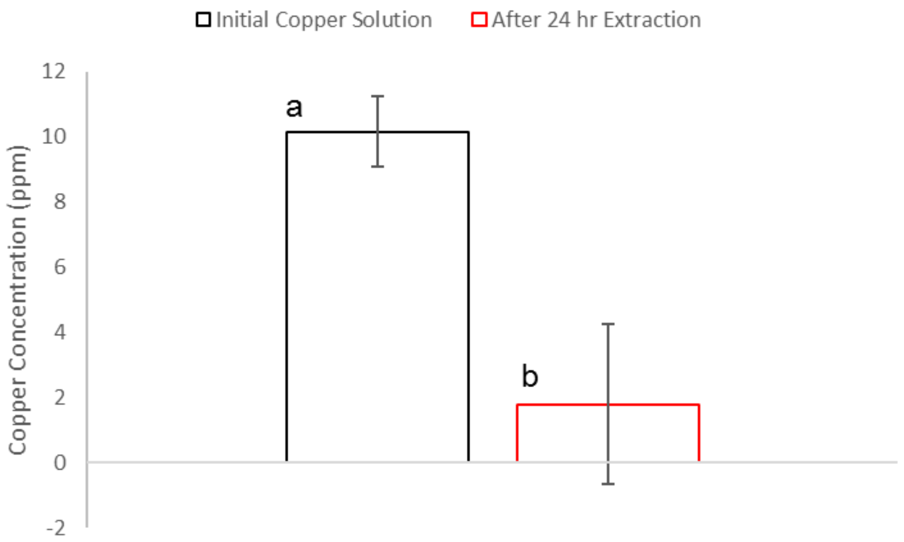

Figure 4.9 Concentration of Cu a) before silica-APTES particles were incubated, b) after 24 hr incubation with the particles. Error bars represent one standard deviation from the mean of three repeats.

4.4.2.2 SEM-EDS

The nanoparticles incubated with copper (II) ions were analysed using SEM-EDS. The particles incubated in solutions in pH ~5 and ~7, show copper on the surface of the nanoparticles, Figure 4.10a and b. The particles incubated in pH ~3 show no copper present on the surface, Figure 4.10c. The protonation of the amine group at pH ~3 hinders the binding of copper ions to the APTES ligand.

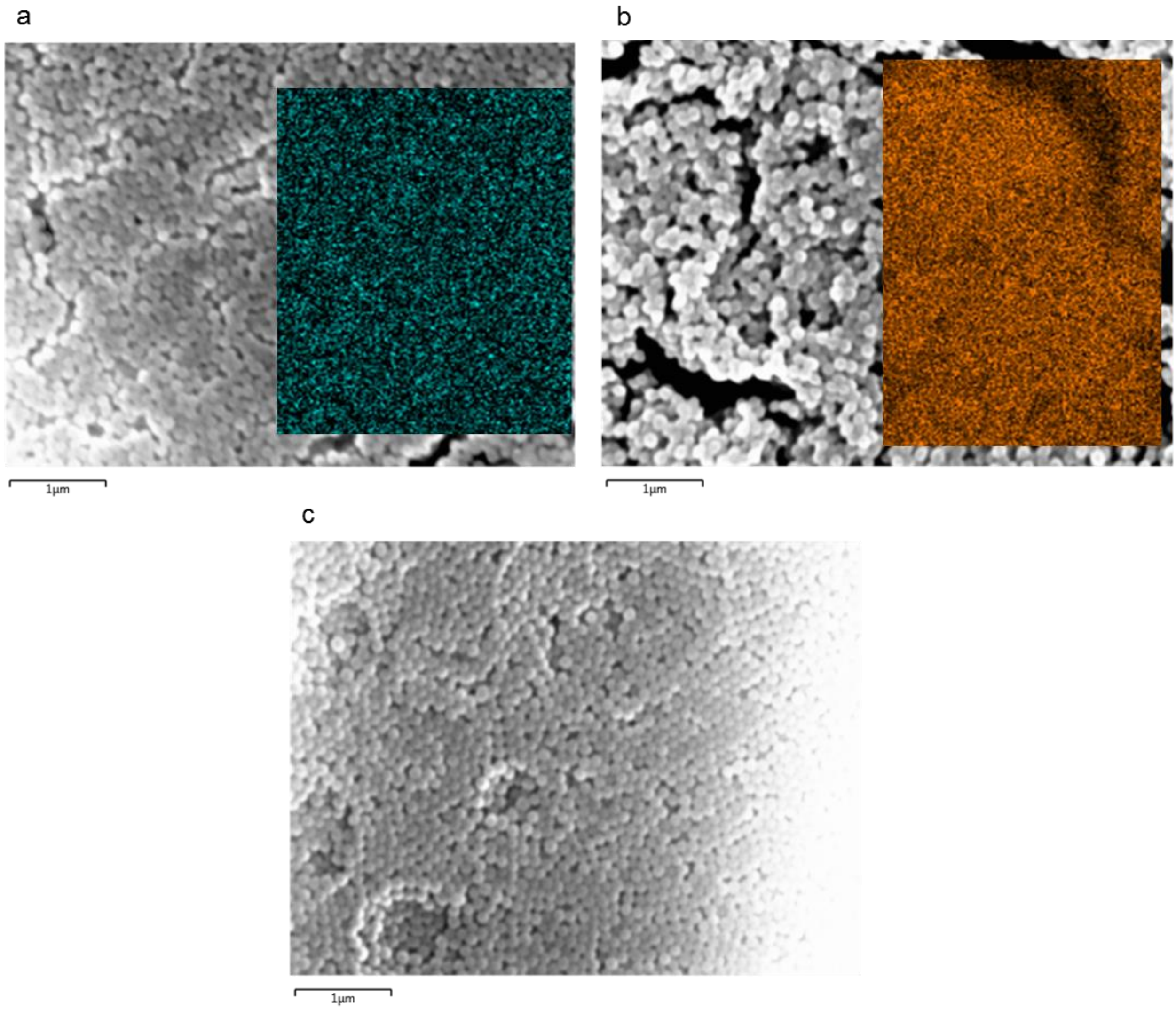

Figure 4.10 SEM images of Si-APTES nanoparticles incubated with copper (10 ppm) at a) pH 5 (copper- blue overlay), b) pH 7 (copper- orange overlay) and c) pH 3 (no copper).Copper Concentration Analysis

The largest change in velocity was observed in 2 mM KCl pH ~7. Experiments at this electrolyte concentration makes counting a significant number of particles (>300) difficult, and time consuming (this is due to low particle count and high background noise). The aim was to produce a technique that was both sensitive and easy to use by less experienced users in the hope it is adopted as a sensor. Thus, results presented here after are analysed in 5 mM. At 5 mM KCl an acceptable particle count (>300/5 min) can be obtained and allows the velocity between Si-APTES and Si-APTES-Cu^{2+} to be distinguished, see Figure 4.2.

To demonstrate a quantitative experiment; Si-APTES particles were placed into a several concentrations of solutions of Cu^{2+} at pH 7. Blank, i.e. Si-APTES particles that had not been exposed to Cu^{2+}, were analysed for comparison. Below 1 ppm, no significant difference was observed, however above 1 ppm a clear increase in particle velocity can be seen, Figure 4.11. The velocity of the particles increases with increasing concentration of metal ion.

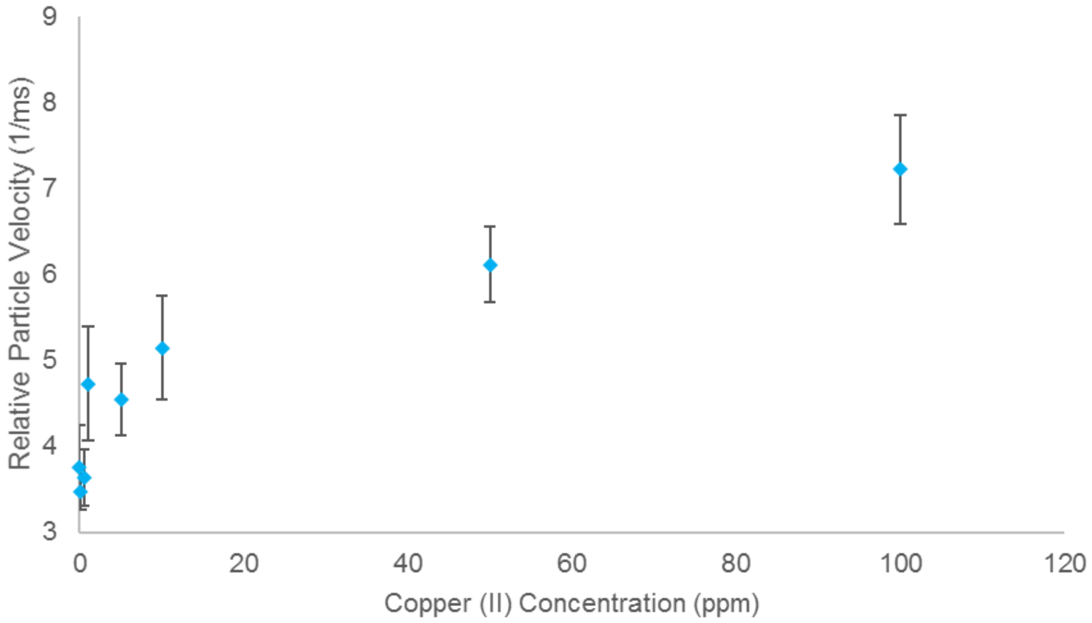

Figure 4.11 Concentration Assay: Silica-APTES nanoparticles incubated in different copper (II) concentration solutions for 24 hr, particle speed was analysed in 5 mM KCl pH 7.0 on at NP200 pore, at a stretch. Error bars represent one standard deviation from the mean of three repeats.

4.4.3 Time Assay

All experiments thus far have utilised a 24 hr incubation period, and this time period is impractical for field measurements. To ascertain the speed in which the signal and Cu^{2+} could be measured the incubation time was decreased to 5 minutes, Figure 4.12, the incubated particles were analysed in KCl (5 mM, pH 7.0). Again a “blank” was analysed for comparison. Particles incubated for the shorter period in 10 and 100 ppm solutions showed a significant increase in speed in comparison to the blank. The longer incubation time of 24 hours did not significantly increase the velocity of the particles suggesting an equilibrium was established quickly.

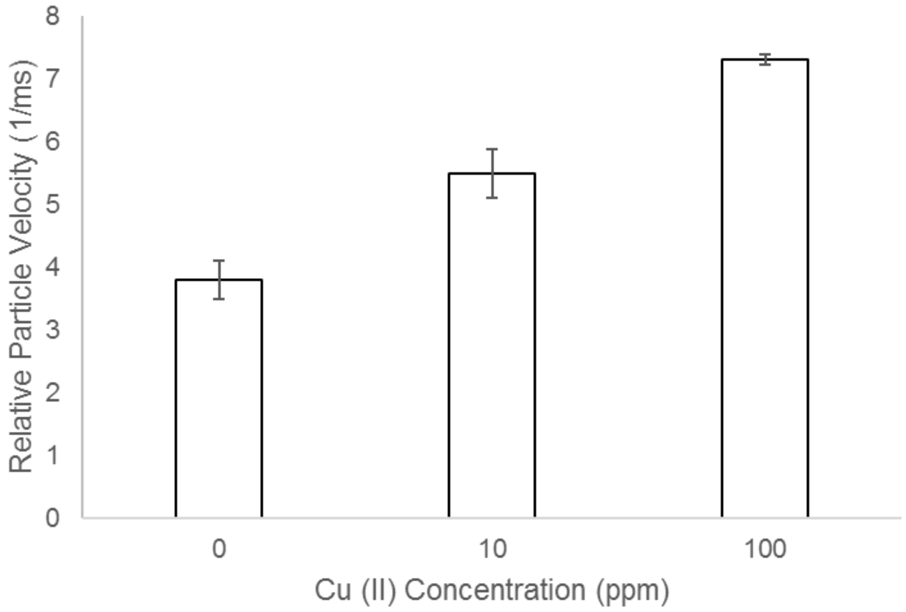

Figure 4.12 Time assay: A change in particle velocity occurs after 5 minutes of incubation with 10 ppm and 100 ppm Cu (II) solutions, measured in 5 mM KCl pH ~7.0. Error bars represent one standard deviation from the mean of three repeats. Samples run on a NP200 pore, 47.50 mm and -2.36 V.

4.4.4 Selectivity

To test the selectivity of the APTES modified silica towards copper the modified nanoparticles were incubated in a series of different metal ions (Mg^{2+}, Na^{+}, Ca^{2+}, Fe^{2+}) and a solution containing a mixture of the above with Cu^{2+}, Figure 4.13. The velocities of the particles were measured after 24 hr in each solution. All metals showed a small increase in velocity from the blank, the particles incubated with the copper ions gave the largest changes from 3.3 to 7.4 mS^{-1}. The particles incubated in the mix of metals show a similar increase in velocity to the copper system, suggesting the Si-APTES particles show preferential binding to the copper (II) ions. To verify this result the concentration of copper remaining in solution was measured by ICP-OES.

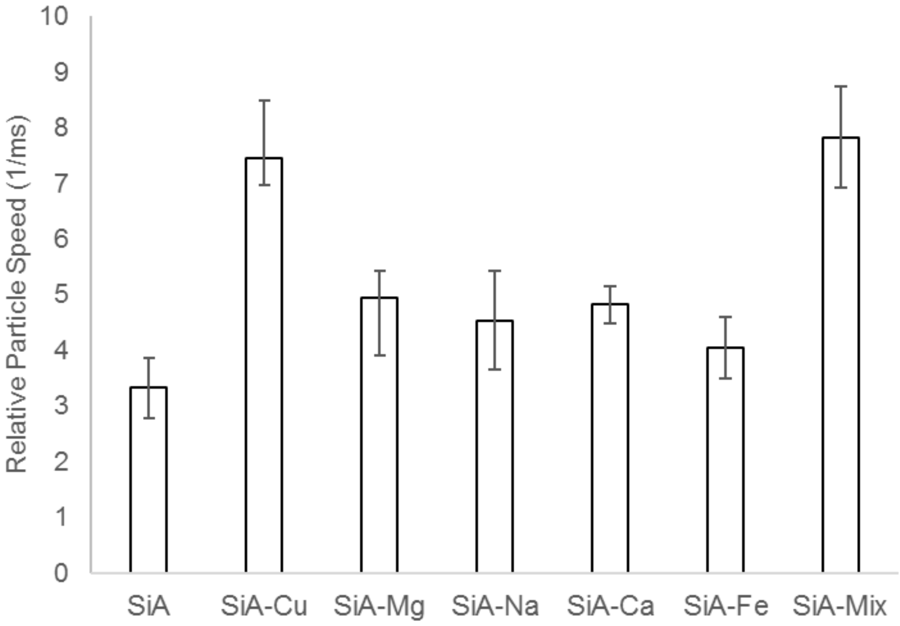

Figure 4.13 Selectivity of the Si-APTES nanoparticles for Cu^{2+} compared to Mg^{2+}, Na^{+}, Ca^{2+}, Fe^{2+} and in the presence of the four competing metal ions (each metal ion at 10 ppm), Error bars represent one standard deviation from the mean of three repeats, Run on a NP200 pore, 47.00 mm and -1.60 V.

4.4.4.1 ICP-OES

The copper standards were run prior to the samples to produce a calibration curve which was used to calculate the concentration of copper in solution, Figure 4.14. The silica-APTES particles were incubated for 24 hr in the solutions containing the mix of competing metal ions and the resulting copper concentration was measured, Figure 4.15. Even in the presence of different metal ions, the silica-APTES nanoparticles removed 72.6 % of the copper ions from solution.

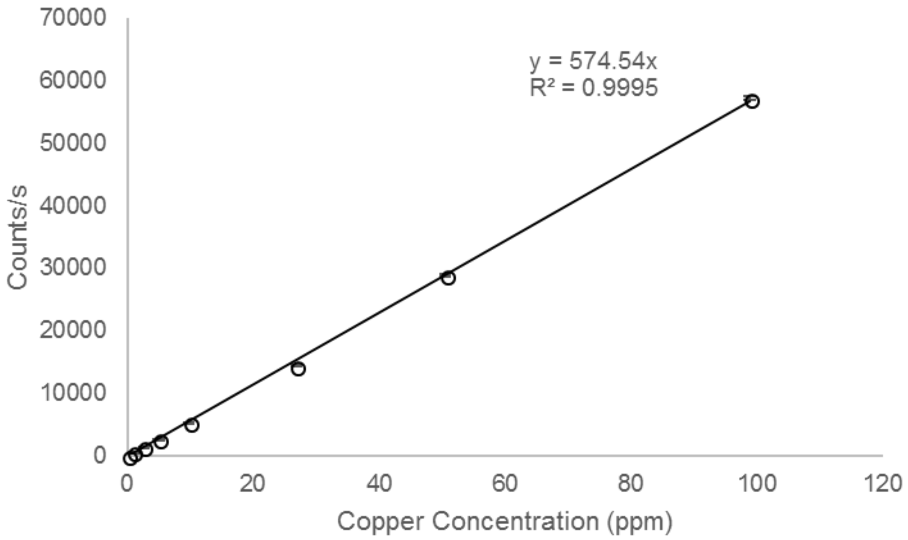

Figure 4.14 Calibration curve for copper concentration v counts per second. Error bar represent one standard deviation from the mean of three repeats.

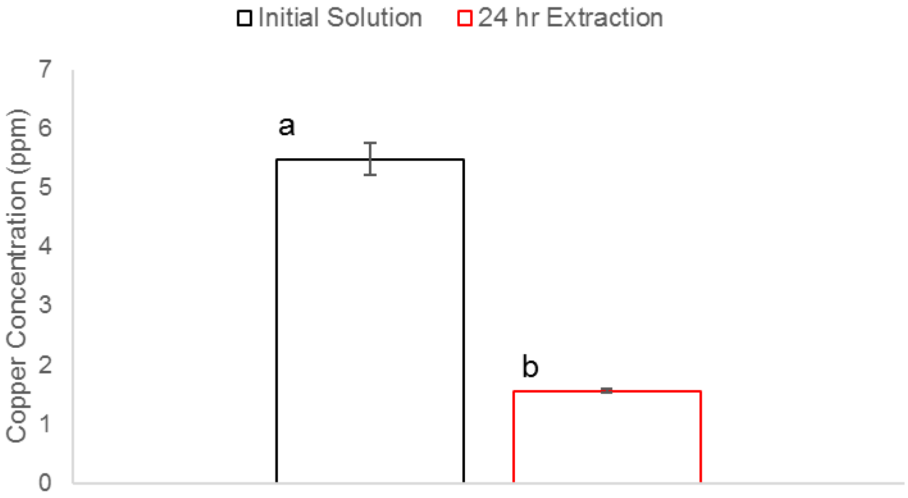

Figure 4.15 Concentration of copper a) before silica-APTES particles were incubated, b) after 24 hr incubation with the particles in the presence of competing metal ions. Error bars represent one standard deviation from the mean of three repeats.

4.4.5 Pulse Waveshape

In addition to the change in the particle translocation velocity, the waveshape of the translocation event was investigated. Biphasic pulse behaviour has been reported in both conventional and tunable RPS in low ionic strengths (< 50 mM KCl).[27,42,43] ICR leads to ion accumulation and depletion within the pore interior, when a charged particle passes through these areas, under certain conditions a change is pulse shape is observed. The change in pulse shape is observed as an increase in conductivity (conductive pulse, Δi_C) before a decrease in current (resistive pulse, Δi_R), Figure 4.16.

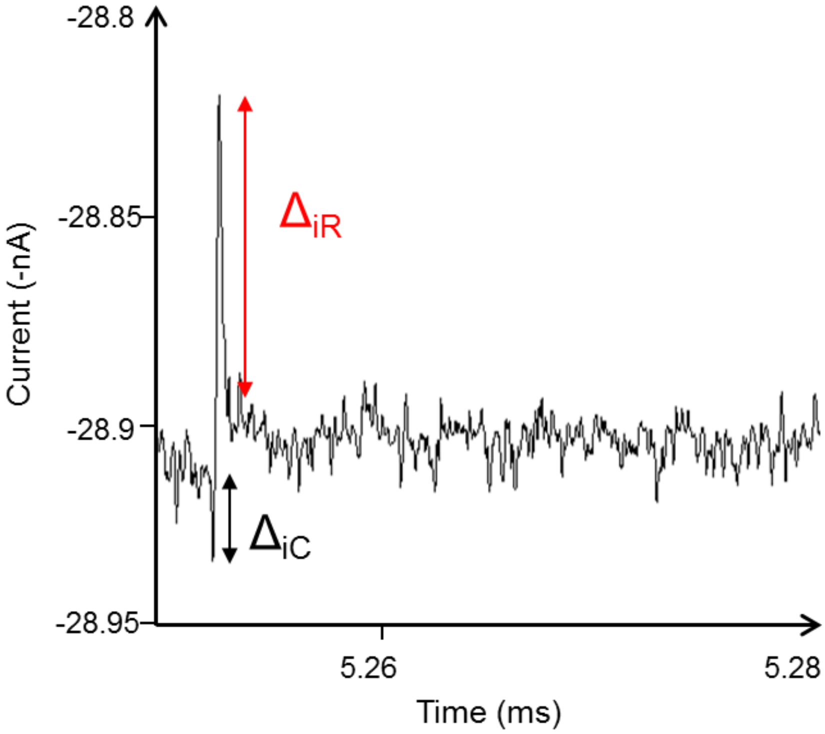

Figure 4.16 Current time recording of a translocating particle. A conductive pulse (Δ_{iC}) is recorded before the resistive pulse (Δ_{iR}).

The conductive pulse arises from a charged particle passing through an area of ion accumulation.[27] The nanoparticles counter ions increase the ionic concentration within the nanopore interior, which is observed as an increase in conductivity before the volume exclusion generated from the particle generates a resistive pulse. The magnitude of the conductive pulse is dependent on the voltage, applied pressure, pore surface charge and the charge of the translocating particle.[27,41] The resistive pulse magnitude is a function of nanoparticle charge.[28,]

At negative potentials, there is an area of ion accumulation within the pore interior of a nanopore with a negative surface charge. When a negative particle passes through this area of accumulation, the K^+ ions associated with the particle increases the ion accumulation further and a conductive pulse is observed. Under the same conditions, a positive particle will only generate a resistive pulse. The resistive pulse will have a greater magnitude compared to a negatively charge particle of the same size. This is due to the Cl^- counter ions being rejected from the pore interior due to the negative charge on the pore surface. [28,41,]

The magnitude of the resistive pulse is dependent on the particles size and on the charge the particle is carrying. The counter ions carried by the particle, can increase or decrease ionic concentrations within the pore and thus result in differences in pulse magnitude. This could result in particle sizes being over/underestimated if they are carrying a high surface charge.[28]

The magnitudes of the resistive and conductive pulse are a function of the particles surface charge. Changes in their size and shape can be seen as the nanoparticle surface is altered, even if the particle size does not change. Conical nanopores, as used within TRPS, exhibit ionic rectification properties. The charge on the pore wall creates areas of ion accumulation and depletion within the pore depending on the applied polarity. This leads to the current being higher at one voltage compared to the voltage of opposite polarity. It is thought that the conductive pulse arises from a charged particle passing through an area of ion accumulation, the nanoparticles counter ions increases the ionic concentration within the pore, which is recorded as an increase in conductivity before the volume exclusion generates a resistive pulse.

When a particle generates a biphasic pulse in TRPS, the particle velocity is still calculated from the resistive pulse. The values for the pulse magnitudes and $T_{0.5}$ for the particle translocation are extracted from the base line before and after the event. Figure 4.17 shows the biphasic pulse and the baseline measured.

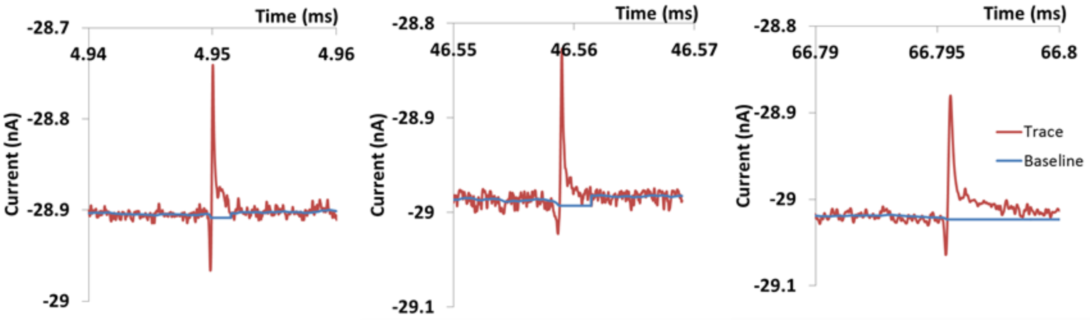

Figure 4.17 Current-time recording of a particle translocation. The blue line represents the baseline from which the pulse magnitudes are measured.

It has been shown that the magnitude of the conductive pulse is dependent on the voltage, applied pressure, pore surface charge and the charge of the translocating particle. The resistive pulse magnitude is also a function of nanoparticle charge. To summarise the expected results based upon theory, at negative potentials, a negatively charged particle passing through a negatively charged pore will generate a conductive pulse before the resistive pulse. A positively charged particle, under the same conditions will only generate a resistive pulse but with a greater magnitude compared to the resistive pulse generated from the negatively charged particle of the same size.

For APTES modified particles both a small conductive and larger resistive pulse were observed at both pH 7 and 5, examples of pH 7 shown in Figure 4.18. At the higher pH the pore surface is negatively charged, shown by current-voltage recordings in Figure 4.19. At pH 7 the conductive pulse magnitude decreases with increasing positive charge on the particle, *i.e.* the binding of the Cu^{2+} ion to the APTES ligand. At pH 5 and with the presence of Cu^{2+}, a small conductive was seen, but the software was unable to distinguish it from the background noise. In both pH 5 and 7, the conductive pulse decreases in magnitude.

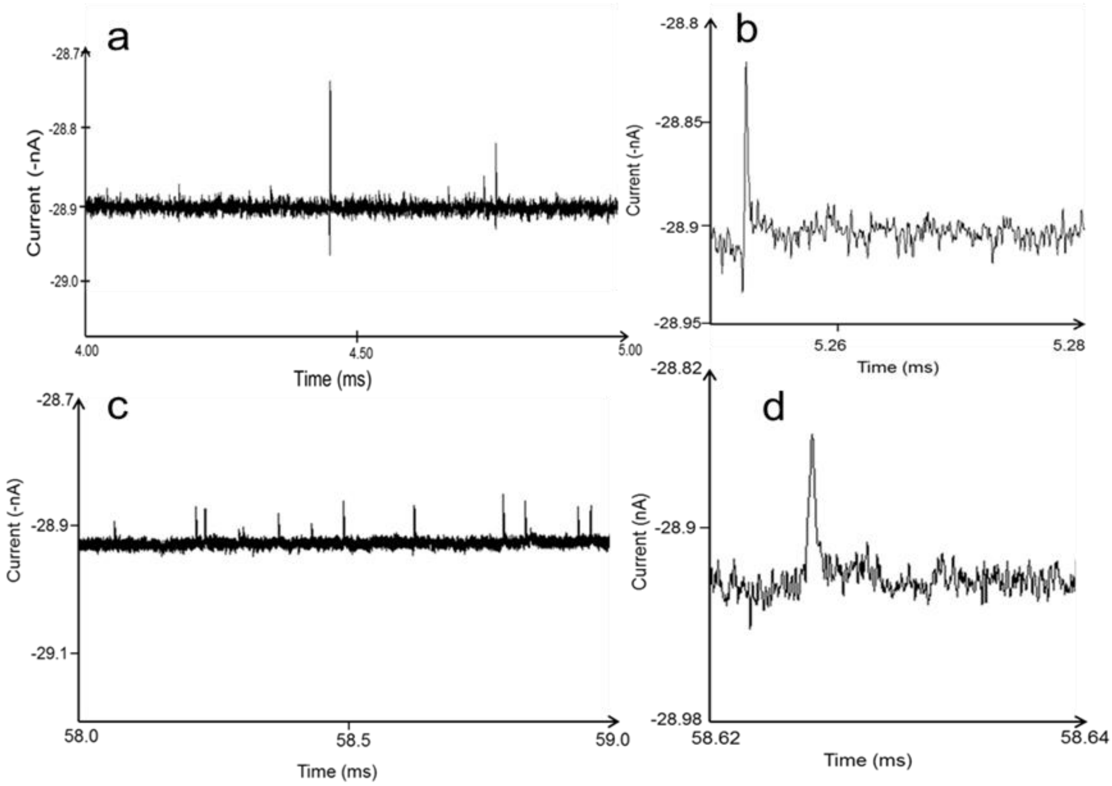

Figure 4.18 Current- time recordings of particle translocations measured in 2 mM KCl pH 7. a) Si-APTES translocation, -3.94 V, b) Magnified pulse from a. c) Si-APTES-Cu particle translocation, -3.94 V. d) Magnified single particle translocation from c.

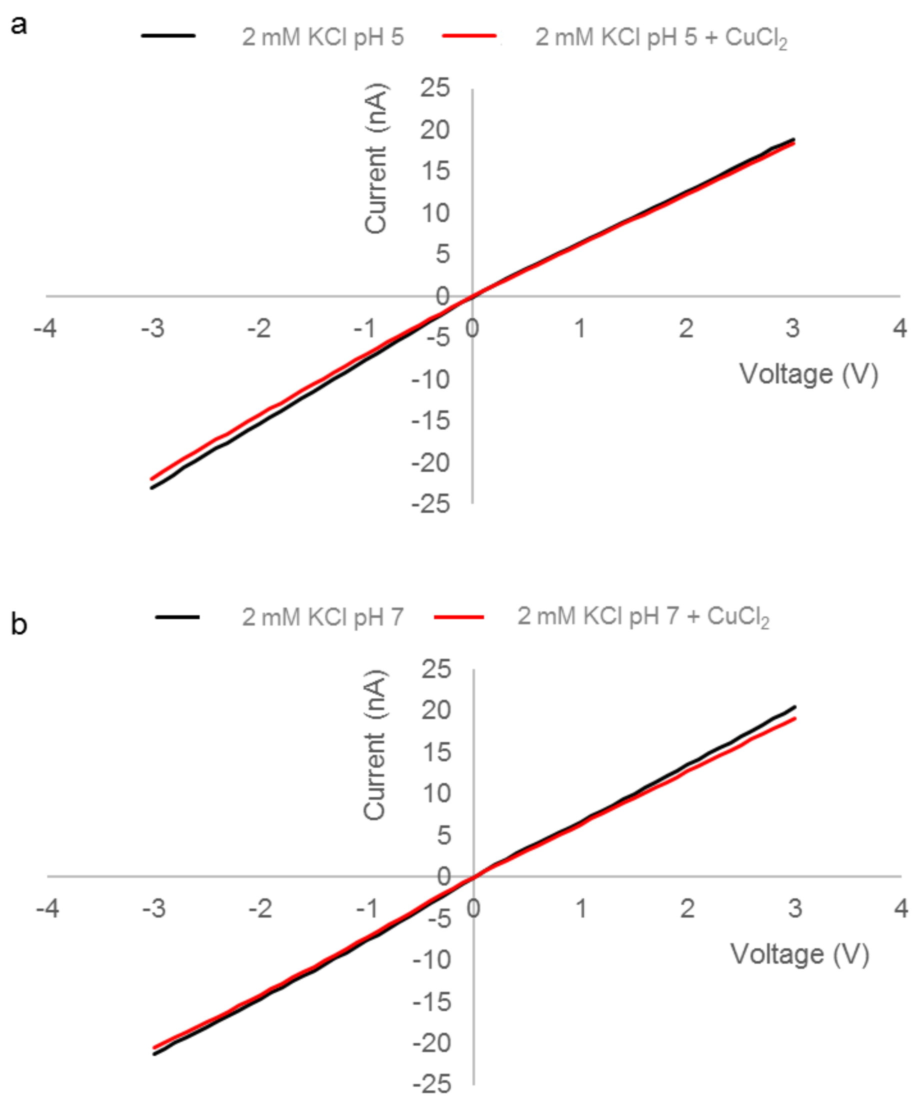

Figure 4.19 Current-voltage curves for 2 mM KCl at a) pH 5 and b) pH 7. The current was recorded again with 15.5 µM $CuCl_2$ present. Recorded on a NP200 pore, 47.11 mm stretch.

In addition to the Δ_{iC} decreasing the Δ_{iR} increased, the values for the pulse magnitudes are given in Figure 4.20. Changes in pulse magnitude can arise from particles aggregating or of axial transport. Here, the particles show no significant aggregation when the Cu^{2+} ion binds, shown in Figure 4.21. Off axial particle trajectory through the pore has also been shown to affect the measured particle blockade, however the results are averaged over hundreds of particles and are relative across a concentration range for the same pore, and should therefore be accounted for within the study. The changes in magnitude are due to the particles counter ions either traversing the pore or being depleted from the pore interior due to the pore surface charge.

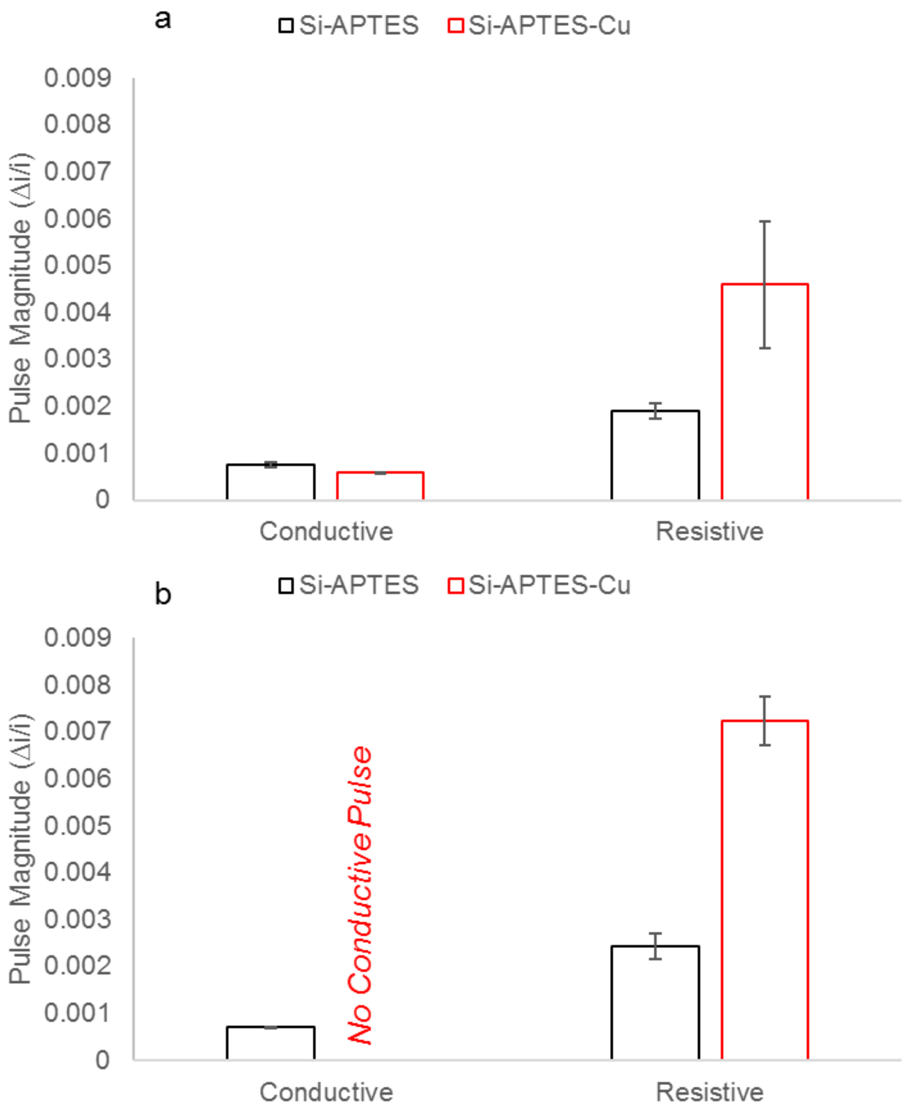

Figure 4.20 a) Conductive and resistive pulse magnitudes recorded for particles with and without copper bound at 2 mM pH 7, -3.94 V. No conductive pulse generated from Si-APTES-Cu particles. b) Conductive pulse and resistive pulse magnitudes recorded for particles with and without copper bound at 2 mM pH 5, -3.94 V. Black lines represent Si-APTES and red lines represent Si-APTES-Cu particles. Error bars represent one standard deviation from the mean for three samples.

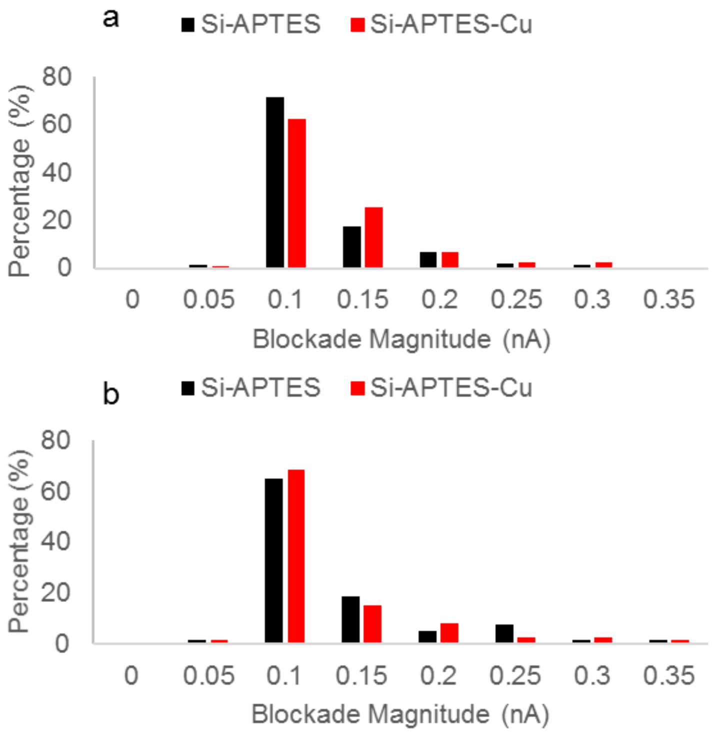

Figure 4.21 Resistive pulse magnitudes of particles with and without copper at a) pH 7 and b) pH 5. Samples analysed in 2 mM KCl on a NP200 pore, 47 mm stretch, -3.18 V. Blockade magnitudes measure for 200 particles in each pH.

The change in pulse shape offers an extra verification that the copper has bound to the particle. When the copper binds to the nanoparticle at pH 5 and 7, the particles increased positive charge results in changes in the waveshape. A Si-APTES particle creates a biphasic pulse as it traverses the pore. When copper is bound to the particle, only a single resistive pulse is generated. The resistive pulse magnitude increases when copper is bound, Figure 4.20. This is explained by the enhanced depletion effect generated by the conical pore and its current rectification properties. This effect interacts with the ion cloud around the positively charged particle. At pH 5, no significant velocity differences between Si-APTES and Si-APTES-Cu^{2+} are observed, Figure 4.7, but measuring the differences in pulse magnitudes allows the changes of the nanoparticle surface to be detected.

At pH 3, the nanopore carries a small positive charge, show by the current-voltage curve in Figure 4.22. At pH 3, the resistive and conductive pulses did not change in size, Figure 4.23. This is due to no copper being bound at the low pH, which is also shown by no change in particle velocity.

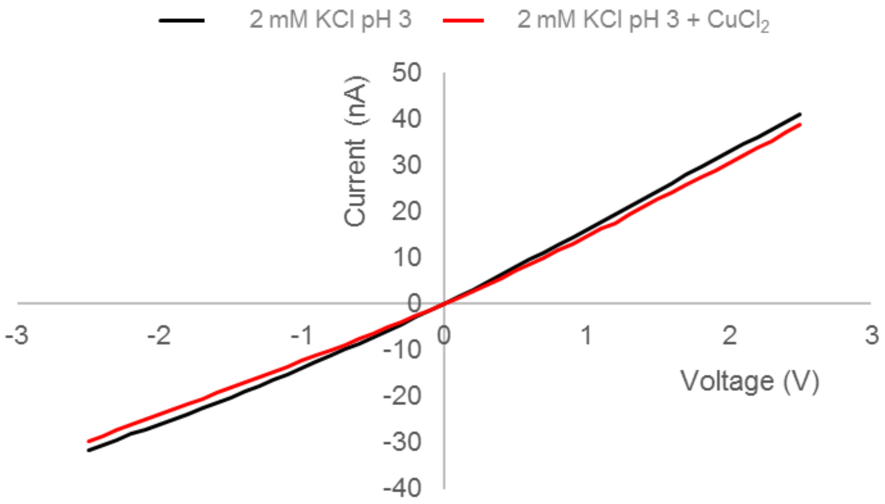

Figure 4.22 Current-voltage curves for 2 mM KCl at pH 3. The current was recorded again with 15.5 µM $CuCl_2$ present. Recorded on a NP200 pore, 47.11 mm stretch.

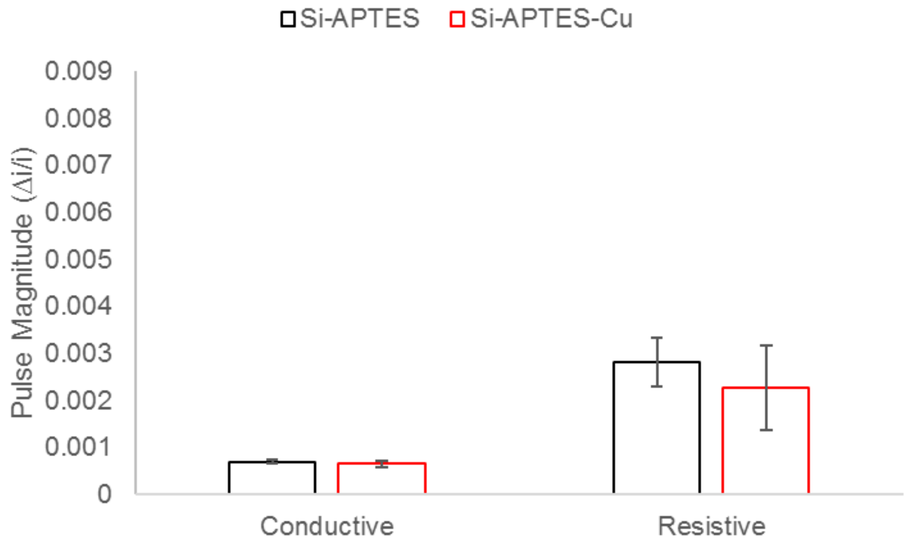

Figure 4.23 Conductive and resistive pulse magnitudes for Si-APTES particles and Si-APTES particles incubated in a copper solution at pH 3.

4.5 Conclusions

Presented in this chapter is a simple and rapid method to use the surface charge of nanoparticles for measuring metal ions in solution. The experiments in this chapter show how using particle translocation velocity and pulse waveshape, the surface charge on a nanoparticle can be monitored and used for the detection of the metal ion, copper (II). The velocity of the particles through the pore were measured before and after incubation with Cu^{2+}. Differences in particle velocity were recorded across a range of ionic strengths, with changes at lower ionic strengths (< 10 mM) being the most prominent. This is due to the double layer increases which reduces the shielding around the particle, allowing changes on the nanoparticle to be detected. The effect of pH on the binding of Cu^{2+} to APTES was investigated, with no particle velocity changes being recorded at pH 3. Changes in particle velocity through the nanopore allows for detection of Cu^{2+} as low as 1 ppm and at 10 ppm with competing metal ions present.

At low ionic strengths, the pulse waveshape changes from a single resistive pulse to a conductive pulse which is then followed by the resistive pulse. Biphasic pulse behaviour has been studied previously in nanopore systems but has not been used for the detection of analytes. The biphasic pulse behaviour of the particle translocating through the pore is used to monitor changes on the nanoparticle surface and infer the presence of ions within the particles double layer. The combination of the particle translocation velocity and pulse waveshape is a powerful tool for monitoring changes upon a nanopore surface such as the binding on a metal ion. This study shows how pH and ionic strength can be tuned for the detection of the chosen analyte. The method can be expanded further by tuning the surface modification to be selective and sensitive towards a specific metal ion. It has the potential for measuring metal ions in environmental samples that require rapid and selective quantification of specific ion.

4.6 References

1. Joshi, A. & Nagaiah, T. C. Nitrogen-doped carbon nanotubes for sensitive and selective determination of heavy metals. *RSC Adv.* **5,** 105119–105127 (2015).

2. Alothman, Z. a. *et al.* Triethylenetetramine modified multiwalled carbon nanotubes for the efficient preconcentration of Pb(II), Cu(II), Ni(II) and Cd(II) before FAAS detection. *RSC Adv.* **5,** 106905–106911 (2015).

3. Ma, P. *et al.* Selective and sensitive SERS sensor for detection of Hg^{2+} in environmental water base on rhodamine- bonded and amino group functionalized SiO_2^- coated Au–Ag core–shell nanorods. *RSC Adv.* **5,** 32168–32174 (2015).

4. Guo, Y. *et al.* Fluorescent copper nanoparticles: recent advances in synthesis and applications for sensing metal ions. *Nanoscale* **8,** 4852–4863 (2016).

5. Ye, Y., Lv, M., Zhang, X. & Zhang, Y. Colorimetric determination of copper(II) ions using gold nanoparticles as a probe. *RSC Adv.* **5,** 102311–102317 (2015).

6. Asgharinezhad, A. A., Jalilian, N., Ebrahimzadeh, H. & Panjali, Z. A simple and fast method based on new magnetic ion imprinted polymer nanoparticles for the selective extraction of Ni(II) ions in different food samples. *RSC Adv.* **5,** 45510–45519 (2015).

7. Girginova, P. I. *et al.* Silica coated magnetite particles for magnetic removal of Hg^{2+} from water. *J. Colloid Interface Sci.* **345,** 234–40 (2010).

8. Behbahani, M., Aliakbari, A., Amini, M. M., Behbahani, A. S. & Omidi, F. Synthesis and characterization of diphenylcarbazide-siliceous mesocellular foam and its application as a novel mesoporous sorbent for preconcentration and trace detection of copper and cadmium ions. *RSC Adv.* **5,** 68500–68509 (2015).

9. Venkateswarlu, S. & Yoon, M. Rapid removal of cadmium ions using green-synthesized Fe_3O_4 nanoparticles capped with diethyl-4-(4 amino-5-mercapto-4H-1,2,4-triazol-3-yl)phenyl phosphonate. *RSC Adv.* **5,** 65444–65453 (2015).

10. Yilmaz, E., Alosmanov, R. M. & Soylak, M. Magnetic solid phase extraction of lead(II) and cadmium(II) on a magnetic phosphorus-containing polymer (M-

PhCP) for their microsampling flame atomic absorption spectrometric determinations. *RSC Adv.* **5,** 33801–33808 (2015).

11. Wang, Z. *et al.* Modified mesoporous silica materials for on-line separation and preconcentration of hexavalent chromium using a microcolumn coupled with flame atomic absorption spectrometry. *Anal. Chim. Acta* **725,** 81–86 (2012).
12. Wu, S., Chandra Sekar, N., Tan, S. N., Xie, H. & Ng, S. H. Determination of chromium(III) by differential pulse stripping voltammetry at a chitosan–gold nanocomposite modified screen printed electrode. *Anal. Methods* **8,** 962–967 (2016).
13. Read, T. L., Joseph, M. B. & Macpherson, J. V. Manipulation and Measurement of pH sensitive Ligand-Metal Binding Using Electrochemical Proton Generation and Metal Detection. *Chem. Commun.* **52,** 1–4 (2016).
14. Meng, X., Xu, Y., Liu, J., Sun, L. & Shi, L. A new fluorescent rhodamine B derivative as an ‘off–on’ chemosensor for Cu^{2+} with high selectivity and sensitivity. *Anal. Methods* **8,** 1044–1051 (2016).
15. Chen, L. *et al.* Facile synthesis of mesoporous carbon nanocomposites from natural biomass for efficient dye adsorption and selective heavy metal removal. *RSC Adv.* **6,** 2259–2269 (2016).
16. Nath, P., Arun, R. K. & Chanda, N. Smart gold nanosensor for easy sensing of lead and copper ions in solution and using paper strips. *RSC Adv.* **5,** 69024–69031 (2015).
17. Blundell, E. L. C. J., Mayne, L. J., Christie, S. D. R. & Platt, M. Protein Detection Using Tunable Pores: Resistive Pulses and Current Rectification. *Faraday Discuss.* **193,** 487–505 (2016).
18. Siwy, Z., Heins, E., Harrell, C. C., Kohli, P. & Martin, C. R. Conical-Nanotube Ion-Current Rectifiers: The Role of Surface Charge. *J. Am. Chem. Soc.* **126,** 10850–10851 (2004).
19. Siwy, Z. S. Ion-Current Rectification in Nanopores and Nanotubes with Broken Symmetry. *Adv. Funct. Mater.* **16,** 735–746 (2006).
20. Lan, W.-J., Holden, D. A., Zhang, B. & White, H. S. Nanoparticle Transport in

Conical-Shaped Nanopores. *Anal. Chem.* **83,** 3840–3847 (2011).

21. Sa, N. & Baker, L. A. Rectification of nanopores at surfaces. *J. Am. Chem. Soc.* **133,** 10398–10401 (2011).

22. Siwy, Z., Heins, E., Harrell, C. C., Kohli, P. & Martin, C. R. Conical-nanotube ion-current rectifiers: The role of surface charge. *J. Am. Chem. Soc.* **126,** 10850–10851 (2004).

23. Jung, J. Y., Joshi, P., Petrossian, L., Thornton, T. J. & Posner, J. D. Electromigration current rectification in a cylindrical nanopore due to asymmetric concentration polarization. *Anal. Chem.* **81,** 3128–3133 (2009).

24. Gao, R. *et al.* Ultrasensitive determination of mercury(II) using glass nanopores functionalized with macrocyclic dioxotetraamines. *Microchim. Acta* **183,** 491–495 (2016).

25. Billinge, E. R. & Platt, M. Multiplexed, label-free detection of biomarkers using aptamers and Tunable Resistive Pulse Sensing (AptaTRPS). *Biosens. Bioelectron.* **68,** 741–748 (2015).

26. Billinge, E. R., Broom, M. & Platt, M. Monitoring aptamer-protein interactions using tunable resistive pulse sensing. *Anal. Chem.* **86,** 1030–1037 (2014).

27. Lan, W. J., Kubeil, C., Xiong, J. W., Bund, A. & White, H. S. Effect of surface charge on the resistive pulse waveshape during particle translocation through glass nanopores. *J. Phys. Chem. C* **118,** 2726–2734 (2014).

28. Qiu, Y. *et al.* Highly Charged Particles Cause a Larger Current Blockage in Micropores Compared to Neutral Particles. *ACS Nano* **10,** 8413–8422 (2016).

29. Qiu, Y., Vlassiouk, I., Chen, Y. & Siwy, Z. S. Direction Dependence of Resistive-Pulse Amplitude in Conically Shaped Mesopores. *Anal. Chem.* **88,** 4917–4925 (2016).

30. World Health Organisation. Copper in Drinking-water Background document for development of WHO Guidelines for Drinking-water Quality. (2004). http://www.who.int/water_sanitation_health/dwq/chemicals/copper.pdf

31. Foster, A. W., Osman, D. & Robinson, N. J. Metal preferences and metallation.

J. Biol. Chem. **289,** 28095–28103 (2014).

32. Brewer, G. J. Copper toxicity in the general population. *Clin. Neurophysiol.* **121,** 459–460 (2010).
33. Holt, J. D. *PhD Thesis,* Loughborough University (2014)
34. Nakanishi, K., Tomita, M. & Kato, K. Synthesis of amino-functionalized mesoporous silica sheets and their application for metal ion capture. *J. Asian Ceram. Soc.* **3,** 70–76 (2015).
35. Mehdinia, A., Shegefti, S. & Shemirani, F. Removal of lead(II), copper(II) and zinc(II) ions from aqueous solutions using magnetic amine-functionalized mesoporous silica nanocomposites. *J. Braz. Chem. Soc.* **26,** 2249–2257 (2015).
36. Mureseanu, M. *et al.* Modified SBA-15 mesoporous silica for heavy metal ions remediation. *Chemosphere* **73,** 1499–1504 (2008).
37. Hill, S. *Inductively Coupled Plasma Spectrometry and its Applications*. (Wiley, 2008).
38. Pearson, G. Hard and Soft Acids and Bases. *J. Am. Chem. Soc.* **85,** 3533–3539 (1963).
39. Hancock, R. D. & Martell, A. E. Ligand Design for Selective Complexation of Metal Ions in Aqueous Solution. *Chem. Rev.* **89,** 1875–1914 (1989).
40. Ahrland, a, Chatt, J. & Davies, N. R. The relative affinities of ligand atoms for acceptors. *Quart. Rev. Chem. Soc* **12,** 265 (1958).
41. Simonsen, S. H. & Burnett, H. M. Spectrophotometric Determination of Copper with Benzoyl-a-pyridyl Thiourea. *Microchem. J.* **15,** 540–544 (1969).
42. Menestrina, J., Yang, C., Schiel, M., Vlassiouk, I. & Siwy, Z. S. Charged particles modulate local ionic concentrations and cause formation of positive peaks in resistive-pulse-based detection. *J. Phys. Chem. C* **118,** 2391–2398 (2014).
43. Weatherall, E. & Willmott, G. R. Conductive and biphasic pulses in tunable resistive pulse sensing. *J. Phys. Chem. B* **119,** 5328–5335 (2015).

5 Ionic current rectification in charged nanopores.

Work presented in this chapter looks at developing a sensor exploiting the current rectification properties of the conical nanopore in TRPS as an alternative to a particle based assay The use of Layer-by-Layer (LbL) assembly of polyelectrolytes onto the surface of the polyurethane pore allowed for modification of the pore wall. The Current-Voltage curves demonstrate the presence of the polymers, producing pH and ionic strength-dependent currents. The LbL assembly allows the facile immobilisation of DNA aptamers onto the pore allowing a specific dose response to Vascular Endothelial Growth Factor, VEGF. VEGF was chosen prior to developing a metal ion assay as it was a system studied in more detail in the literature and within the group. Monitoring changes to the current rectification allows for a rapid detection of 5 pM VEGF. Work presented in this chapter was a contribution towards the publication: Protein Detection Using Tunable Pores: Resistive Pulses and Current Rectification. *Faraday Discuss.* **193,** 487–505 (2016).[1] The publication explores the comparison between a pore based assay and a particle based assay, work presented here was my contribution towards the publication.

5.1 Aims and Objectives

The aim of this chapter is to study and manipulate the current rectification properties of the nanopores used in TRPS experiments. Chapter 4 showed how biphasic pulses were generated due to the presence of current rectification. This chapter explores the conditions in which rectification occurs within the pore and how surface modifications of the pore can be monitored via a change in current flow. The final objective is to detect an analyte (VEGF) using current rectification and to determine the detection limits of the method.

5.2 Introduction

An alternative to a particle-based assay is to use the change in ionic current through the pore, which can be controlled via the modification of the electroosmotic flow through the pore. The electroosmotic flow can be tuned by changing the supporting electrolyte, pH, ionic strength and applied voltage, with the current–voltage, *I*-*V*, curves recording an asymmetric behaviour.[2,3]

Nanopores in a variety of materials exhibit ionic current rectification. Nanopores prepared in polymer films,[2,4,5] glass membranes,[3,6] silicon nitride[7] and gold nanotubes[8] exhibit current rectification when conical in shape. The shape and charged nature of the pore leads to areas of ion accumulation and ion depletion within the pore interior. In turn this leads to a higher current at one voltage compared to the current at the equal voltage but of opposite polarity. This suggests that there is preferential direction for ion transport.

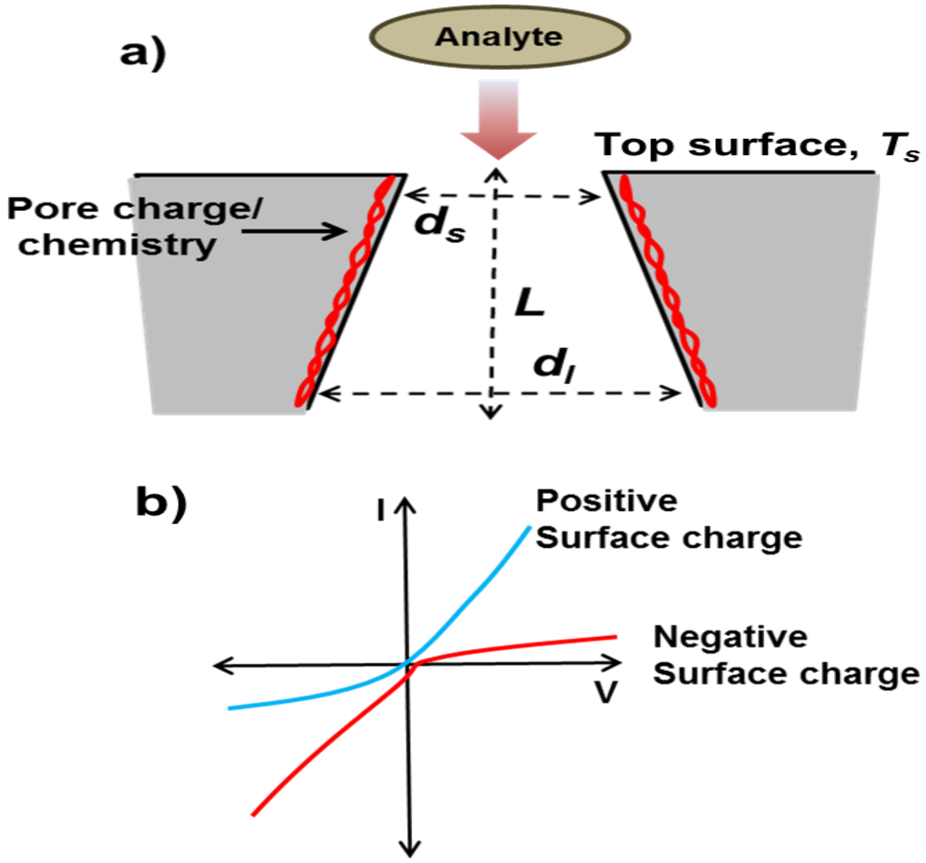

Figure 5.1 a) Schematic of a conical polyurethane pore with small, large pore diameter and pore length, d_s, d_l and L respectively. The top surface of the pore is labelled T_S. b) Schematic of I-V curves for conical pores with different surface charge.

The flow of ions through a nanopore is dependent on the nanopore's surface charge. A negatively charged pore will result in a higher current at a negative voltage compared to the current at the voltage of opposite polarity, Figure 5.1b. When a negative potential is applied, the potassium ions (K^+) flow from the external bulk solution to the pore interior. The chloride ions (Cl^-) move in the opposite direction and are rejected from the negative pore surface. This leads to an increase in K^+ and Cl^- concentrations in the pore interior which leads in an increase in conductivity. When a positive potential is applied the Cl^- are blocked from flowing from the external solution to the internal solution by the charge on the pore. This leads to a depletion of Cl^- within the pore interior and decreases the conductivity. If the nanopore is positively charged, the opposite is true; the current is higher at a positive polarity compared to the voltage at the negative polarity.

By modifying the pores surface, the flow of current can be controlled and allow for molecule detection.[9] Nanopores have been modified with a variety of ligands for the detection of biomolecules. Pores in polymer films have been functionalised with iron-terpyridine for the detection of lactoferrin[10] and biotinylated for the detection of avidin and streptavidin.[11] Gold nanopores were modified with molecular recognition sites to detect streptavidin, immunoglobulin and ricin.[12] The biomolecules binding in these pores leads to permanent blockage of the ionic current and blockage of the nanopore.[12]

Here we modify the surface of polyurethane (PU) pores to detect Vascular Endothelial Growth Factor (*VEGF)*. The pores were modified with the anti-*VEGF* aptamer and the current rectification ratio was monitored (measured at ±1.6 V) in the presence of the *VEGF* protein. The surfaces of the pores were easily modified using a layer-by-layer (LbL), assembly of polymers, polyethylene amine (PEI), and polyacrylic acid-maleic acid (PAAMA). The use of PEI and PAAMA allowed for the easy modification, and reversible surface charge of the pores giving a pH and ionic strength controlled current flow, with current rectification ratios as high as 3. The LbL assembly was shown to be stable for days, allowing the modification of the pore wall with DNA via standard carbodiimide chemistry. The current rectification assay allows for the detection of VEGF down to 5 pM.

5.3 Experimental

5.3.1 Materials and Methods

The following chemicals were purchased from Sigma Aldrich, UK, poly(ethyleneimine), PEI, low molecular weight, LMW (LMW PEI Mw ~ 2000 g mol^{-1}, 50 % wt., 408700) and high molecular weight, HMW, (HMW PEI Mw 750 000 g mol^{-1}, analytical standard, 50 % wt., P3143), poly(acrylic acid-co-maleic acid) (PAAMA, Mw ~3000 g mol^{-1} 50 % wt, 416053), phosphate buffered saline solution (P4417 (0.01 M phosphate buffer, 0.0027 M 9otassium Chloride, 0.137 M sodium Chloride, pH 7.4)), bovine serum albumin (BSA, lyophilized powder, ≥96 %, A2153) and 2-(N--morpholino)ethanesulfonic acid hydrate (MES hydrate, ≥99.5 %, M2933). Tunable conical pores (NP200) were purchased from Izon Science (Christchurch, NZ). Carboxylated polystyrene particles with a mean nominal diameter of 210 nm were purchased from Bangs Laboratories, US and are denoted as CPC200. Potassium chloride (KCl, >99 %, P/4240/60) and potassium hydroxide (KOH, 0.1 M, >85 %, P/5600/60) were purchased from Fisher Scientific, UK. Hydrochloric acid (HCl, 0.5 M, 37 %) was purchased from VWR, UK. 1-ethyl-3-(3-dimethylaminopropyl)carbodiimide hydrochloride (EDC, 22980) and recombinant human Vascular Endothelial Cell Growth Factor (VEGF, lyophilised, >95 %, PHC9394) were purchased from Thermo Scientific, UK.

Custom DNA oligonucleotides were purchased as lyophilised powders (100 pmol/µL) from Sigma Aldrich, UK with DNA sequence as follows: 5’TGTGGGGGTGGACGGGCCGGGTAGATTTTT(V7t1 amine)[13] purchased with an amine functional group at the 3’ end.

All reagents were used without further purification and all solutions were prepared in deionised water with a resistivity of 18.2 MΩ cm (TKA, Smart2Pure). pH of the solutions were altered using HCl and KOH and the solutions were measured using a Mettler Toledo easy five pH meter with a Mettler Toledo InLab micro electrode.

5.3.2 TRPS Set-Up

All measurements were conducted using the qNano, (Izon Sciences Ltd, NZ) combining tunable nanopores with data capture and analysis software, Izon Control Suite v.3.2. The lower fluid cell contains the electrolyte (75 µL). The upper fluid cell contains 40 µL of the sample which is prepared in the same electrolyte. An inherent pressure on the system (47 Pa) was present when recording a current-voltage curve.

The membranes containing the conical pore were placed onto jaws on the qNano instrument and are capable of being stretched.[14] Experiments were run at stretch denoted 45 mm.

5.3.3 Pore Modification

Conical pores were modified by incubating the pore in the polymer solution (5 % wt. in H_2O) at a stretch of 45 mm for two hours, followed by rinsing the pores with deionised water. The pores were then incubated with second polymer layer 2 hours, again washed with deionised water. This process was repeated until the required number of layers was achieved.

5.3.4 Modification of PAAMA modified pores with DNA

The oligomer was dissolved in 100 mM pH 5.9 MES buffer containing 1 mg mL^{-1} EDC. The final concentration of DNA was 220 nM. The pores were incubated with the DNA and EDC solution for 2 hours.

5.3.5 VEGF *I-V* assay

VEGF was suspended in PBS buffer to give the desired concentration. DNA modified pores were incubated in the VEGF solution, in each experiment the VEGF solution was only placed on the side of the pore with the small pore opening Ds. When multiple solutions of different concentrations of VEGF were used the lowest concentration was measured first. The VEGF solution was in contact with the pore for 30 minutes with the pore being rinsed with water x 3, and PBS x 3 after each protein concentration. The current rectification property of the pore was then measured, in a range of KCl solutions starting with 5 mM first and working up to 50 mM. When a BSA control was used, 50 nM BSA was incubated first for 30 minutes, with the rectification properties being measured in KCl solutions before adding VEGF to the pore.

5.3.6 *I-V* Measurements

The pores were mounted between two fluid cells which contain an electrolyte solution. Current-voltage (*I-V*) curves were recorded using Izon control suite v3.2, the potential was stepped in 100 mV increments from +1.6 to -1.6 V and the resulting current measured.

5.4 Results and Discussion

Figure 5.2 shows the *I-V* curves of an unmodified pore in a range of ionic strengths. Each pore was measured in 100 mV increments from +1.6 to -1.6 V, in higher ionic strengths >50 mM the signal would saturate above ±1.6 V. Rectification ratios are used for a measure of current rectification and is calculated by dividing the current measured at 1.6 V by the current recorded at – 1.6 V. A weak current rectification ratio of 1.38 in 5 mM, Figure 5.2a, is observed which is unsurprising as at these parameters as the pore wall contains a low charge density and the double layer thickness should be much smaller than the pore opening. The *I-V* curve for an unmodified pore in higher ionic strengths are shown in Figure 5.2b,c and d, and here the rectification values are 1, illustrating an ohmic response.

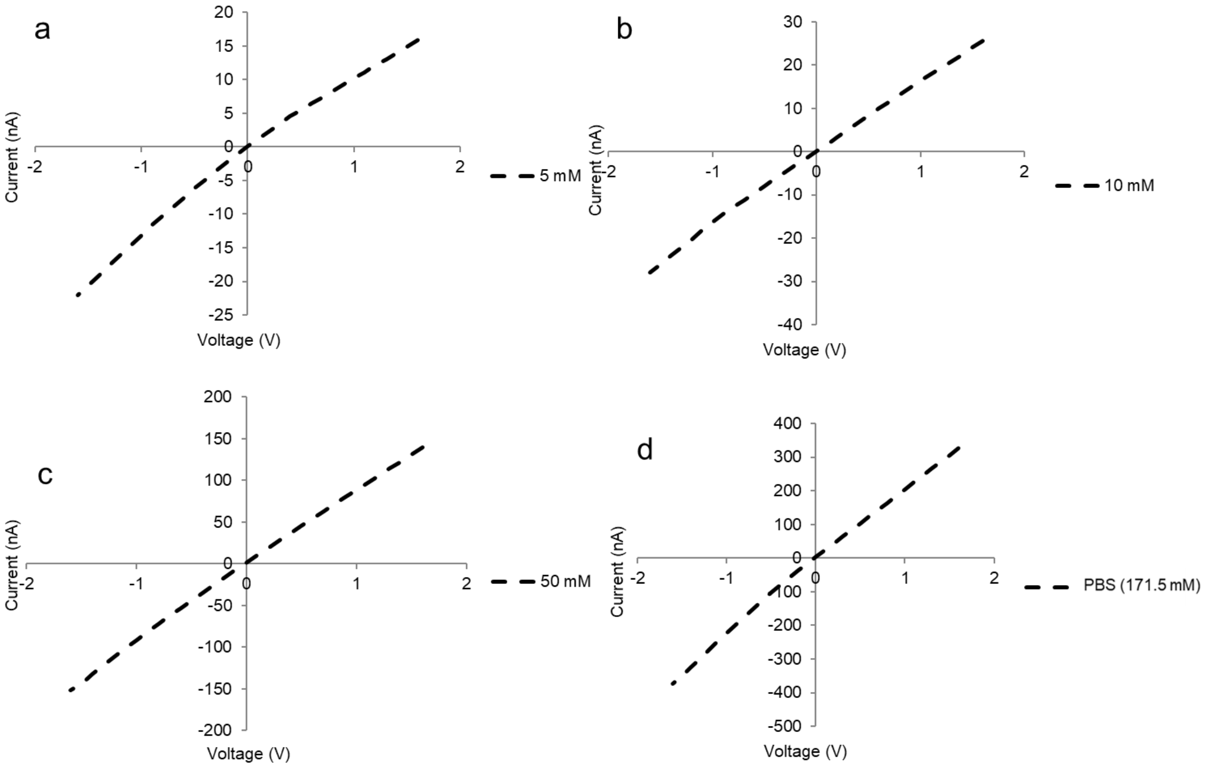

Figure 5.2 Current-volatge (I-V) recordings of an unmodified nanopore measured in different ionic strengths a) 5 mM KCl b) 10 mM KCl c) 50 mM KCl and d) 171.5 mM PBS.

Table 5.1 Rectification ratios measured at 1.6 V for the unmodified pores in different ionic strengths. Rectification averages for three pores with ± 1 standard deviation from the mean.

[KCl] mM	Rectification Ratio
5	1.73±0.56
10	1.30±0.50
50	1.19±0.11
PBS	1.08±0.06

In an attempt to introduce a facile method for modifying the surface chemistry of the pore a LbL, assembly using PAAMA/ PEI was investigated. This system is well studied having been previously used to modify a range of materials[15–20]. We favoured this technique over plasma or other treatment such as the incorporation of grafting polymers into the matrix via swelling[21,22], as it allows for a simple and rapid dip coating strategy that would not damage or change the pores features. In addition the LbL would allow the thickness and even the porosity of the PEI/PAAMA bilayer to be controlled in the future.[18] Here we have adopted to use no more than two bilayers to ensure the they do not extend across the pore opening and that the thickness of the bilayers remains in the order of a few nanometres.[19]

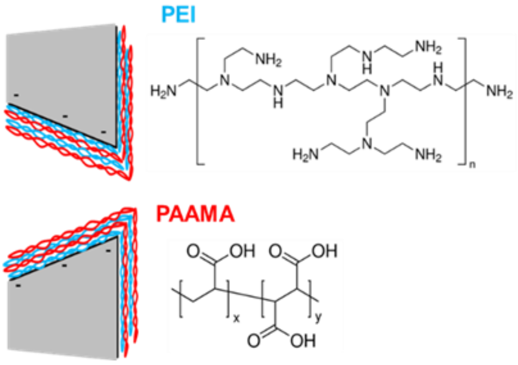

Figure 5.3 Schematic diagram showing the layers using PEI and PAAMA.

Figure 5.3, shows the schematic of the bilayer construction with consecutive PEI/ PAAMA layers. The resulting *I-V* curves in a 5 mM KCl solution are shown in Figure 5.4 alongside the unmodified pore. The addition of the PEI onto the pores surface resulted in a change in the preferred direction of current flow, with a reduced and enhanced current flow through the pore under a negative and positive applied potential respectively. This is indicative of a positive surface charge.[23] Upon coating with

PAAMA, the surface charge switches to negative, resulting in the preferred direction of current flow being inverted.

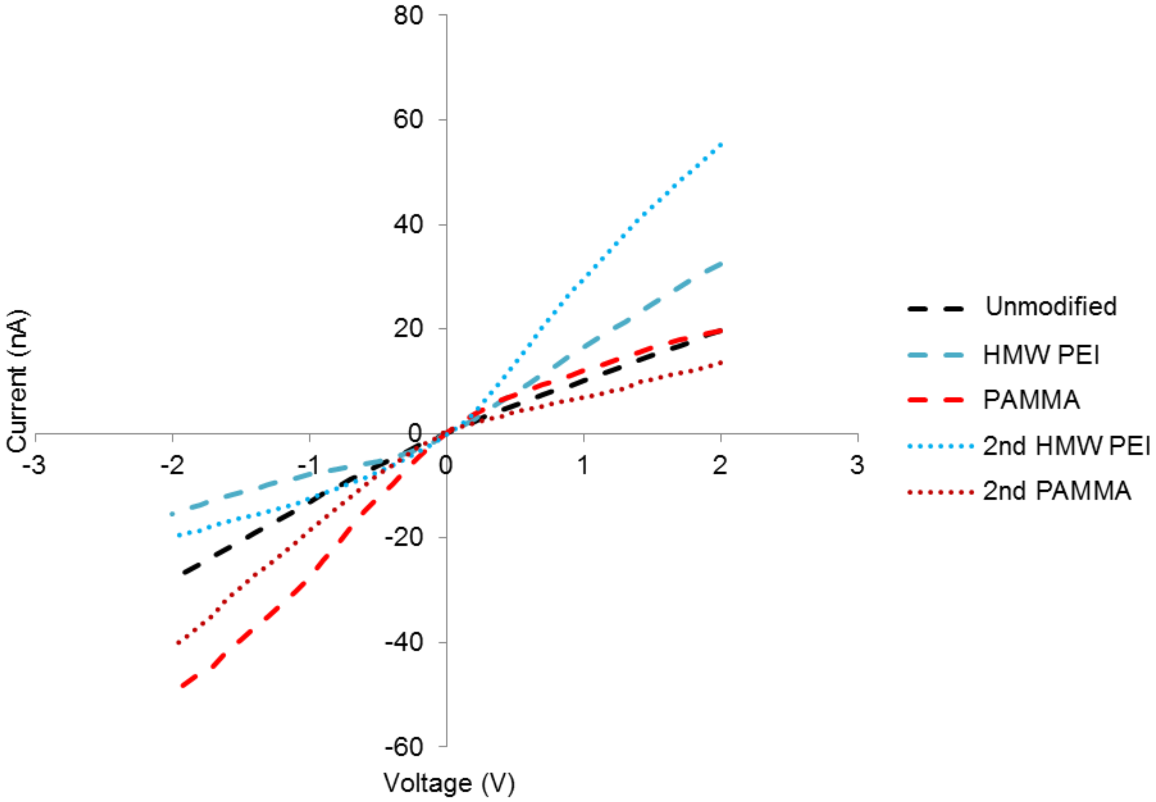

Figure 5.4 Current – voltage (I-V) curves showing the rectification of the nanopore modified with high molecular weight PEI and PAAMA. Recorded in 5 mM KCl.

The rectification ratios for the HMW PEI bilayers are listed in Table 5.2, measured at ±1.6V. The addition of each layer of the LbL assembly caused the preferential current direction, or “on state” to be switched. The magnitude of the rectification can be used to access the presence and quality of the pore coating and as the number of bilayers increased, the rectification ratios improved. It is interesting to note that even with two bilayers added to the pore walls, the pore opening remains unobstructed, as the addition of 210 nm particles to the upper fluid cell results in a standard resistive pulse response as they traverse the pore. This demonstrated that the pore is not blocked with a polymer mesh, or that the bilayers have restricted the pore orifice to a large extend and confirms our hypothesis that the bilayers of on the orders of a few nM thick at the pore mouth.

Table 5.2 *Rectification ratios for a nanopore modified with HMW PEI and PAAMA measured in different ionic strengths. Listed are KCl solution at pH 6.8 and PBS at pH 7.4.[KCl] mM*

	Unmodified Pore	HMW PEI	PAAMA	2^{nd} HMW PEI	2nd PAAMA
5	1.38	0.46	2.40	0.37	2.86
10	1.09	0.67	1.69	0.29	2.44
50	1.09	0.90	1.10	0.73	2.09
PBS (pH 7.4)	1.15	0.81	1.10	0.93	1.29

Ionic current rectification is affected by ionic strength and Table 5.2 shows the effect in increasing the ionic strength of the solution on the rectification ratio. Increasing the ionic strength reduced the rectification properties of the pore, however it is interesting to note that even at above 50 mM, Figure 5.5, with a pore diameter circa 800 nm some rectification was observed. The pore size should be much larger than the electric double layer, and it was initially hypothesised that the rectification of the pores would diminish under such conditions. The persistence of the rectification may be enhanced by the nature of the modification of the pores using the LbL technique which the top surface, T_S, Figure 5.1, to be also modified along with the inner pore walls. A combination of top surface and pore wall modification has been shown to have a bigger effect on the rectification ration and may form a signification part of the behaviour.[3]

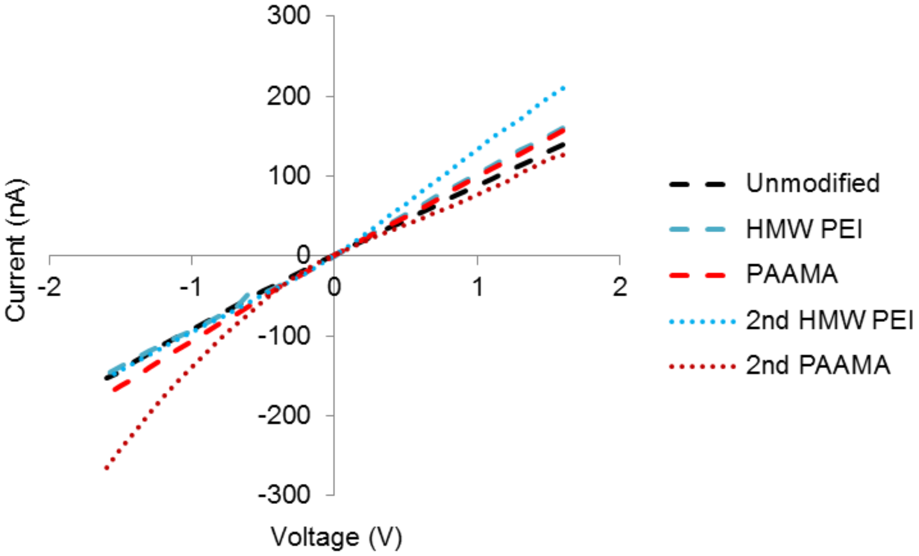

Figure 5.5 Current – Voltage (I-V) curves showing the rectification of the nanopore modified with high molecular weight PEI and PAAMA. Recorded in 50 mM KCl.

A similar set of *I-V* curves were obtained when LMW PEI was used, shown in Figure 5.6. However, the rectification ratios for each subsequent PEI and PAAMA layer were not as high, Table 5.3. This is likely due to the nature of the PEI layer placed onto the surface. The mechanism for LbL assembly goes through island formation before forming a full layer and it is hypothesised that when using the LMW PEI it takes longer to form a full coated surface layer. Subsequent experiments only used HMW PEI when modifying the nanopores.

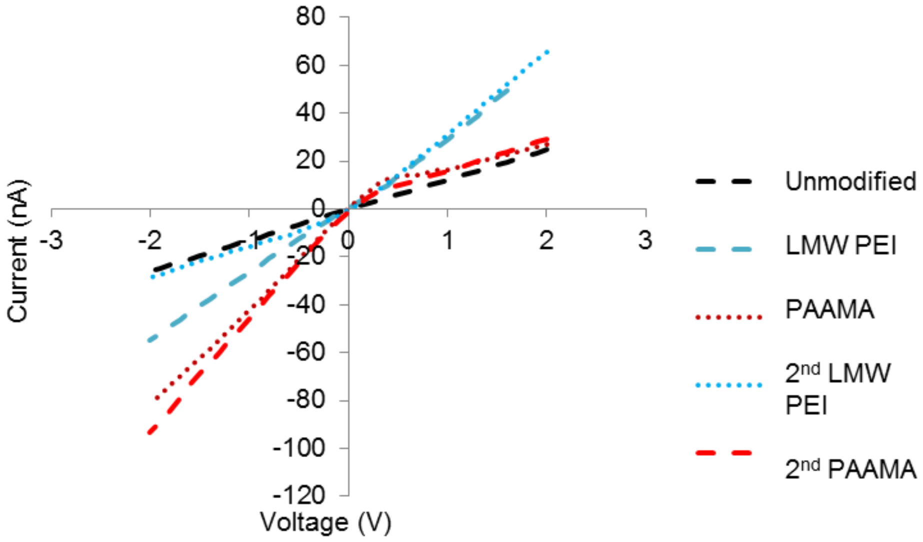

Figure 5.6 Current - Voltage (I-V) curves for low molecular weight PEI and PAAMA layers alongside an unmodified pore. Recorded in 5 mM KCl.

Table 5.3 Rectification ratios for a nanopore modified with LMW PEI and PAAMA measured in different ionic strengths. Listed are KCl solution at pH 6.8 and PBS at pH 7.4.

[KCl] mM	Unmodified Pore	LMW PEI	PAAMA	2nd LMW PEI	2nd PAAMA
5	1.06	0.87	2.89	0.45	3.07
10	1.01	0.96	1.21	0.73	1.35
50	0.98	0.96	1.03	0.95	0.96
PBS (pH 7.4)	0.98	1.00	1.00	1.02	0.97

The stability of the polyelectrolytes was investigated and the LbL approach was repeated on different pores. The LbL approach was shown to be reproducible on different pores, Figure 5.7. The rectification ratios for each pore modified show the same trend, however the current-voltage curves may differ. This is due to the fabrication of the pores, each pore is not a uniform size and shape leading to differences in rectification properties. To improve the method, pores of the exact size and shape would need to be used. The modification of the nanopores was also stable across several cycles shown in Figure 5.7. The *I-V* curves were recorded 1.6 V to -1.6 V, then from -1.6 V to 1.6 V and repeated once more in the opposite direction. This shows slight hysteresis at low – V, this would need to be investigated further and more scans performed.

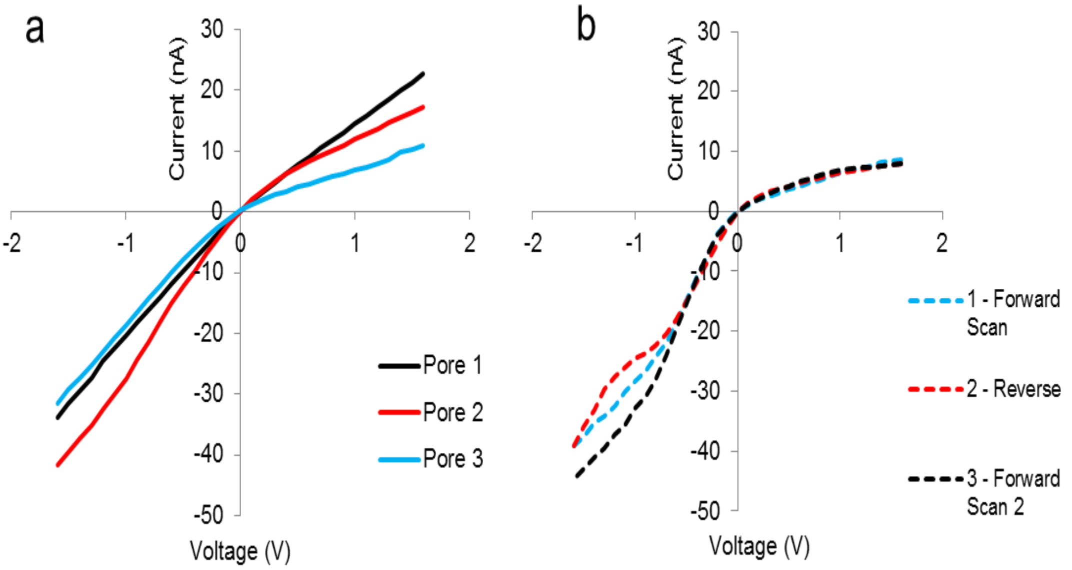

Figure 5.7 Current – voltage (I-V) curves in 5 mM KCl a) recorded on three different pores, each with two bilayers. b) Consecutive scans across the voltage range. Forward scan refers to moving from +1.6V to -1.6V. Each current was recorded after a 5 second wait to the new voltage.

The LbL coating was investigated for stability over time. It was found that the coating was stable over a short period of time even after multiple uses, washes, and being dried and stored overnight, shown in Figure 5.8, although multiple uses and storage for over a week resulted in a deterioration of the surface chemistry.

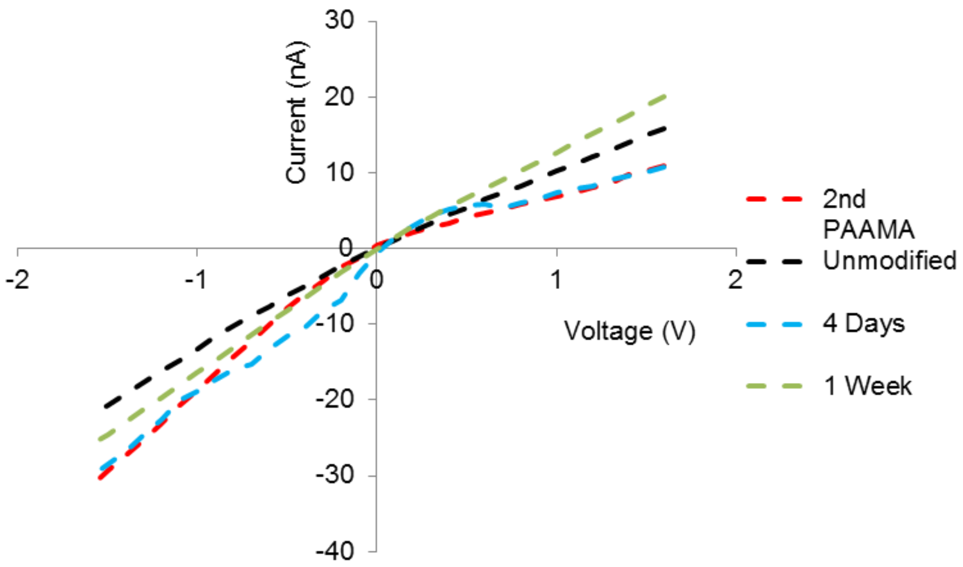

Figure 5.8 Current – Voltage (I-V) curves for an individual pore coated with two bilayers recorded on selected days after the modification.

Given the flexible nature of the PU pore it should be possible to change the rectification ratio by altering the pore's stretch. A smaller stretch, therefore a smaller pore size, produces a higher rectification ratio. A larger stretch, decreases the rectification ratio. Figure 5.9 shows the effect on the *I-V* curves as the stretch is decreased from 47 mm to 44 mm. As the pore opening, d_S, is reduced the observed current at positive potentials decreases.

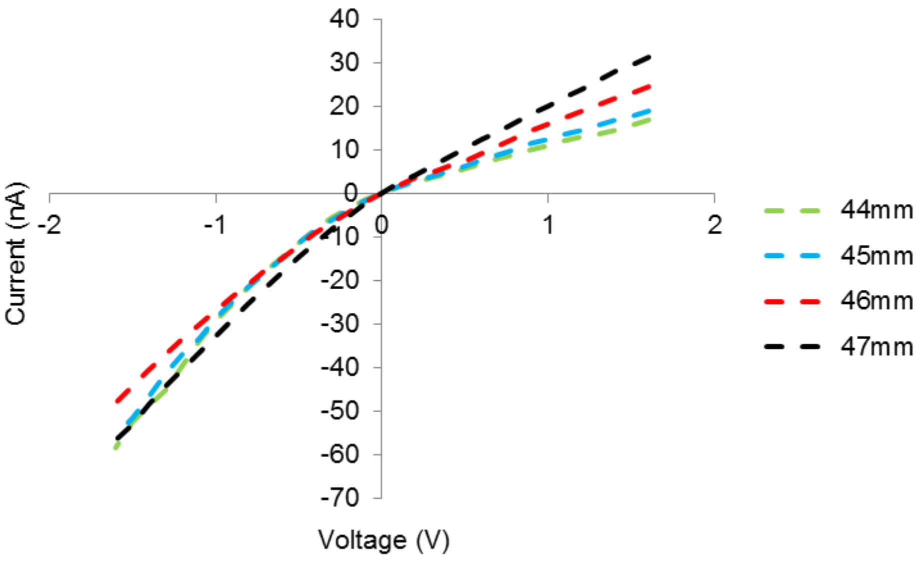

Figure 5.9 Current – voltage (I-V) of nanopores modified with two bilayers recorded at different stretches in 5 mM KCl.

In addition to the pore size, both the PEI and PAAMA have functional groups which should allow a pH controlled current flow. Figure 5.10a and b show the effect of pH on the *I-V* relationship for both the PEI and PAAMA surfaces, for comparison the data for an unmodified pore is given alongside. Lowering the pH of the solution to 3 increases the charge density on the PEI surface as more amines become protonated; this results in an increased current flow at positive potentials and a rectification ratio as low as 0.31. Conversely increasing the pH to 7 reduced the positive charge on the PEI and the current rectification ratio increases to an unmodified pore at 0.52. Table 5.4 lists the rectification ratios for PEI and PAAMA pores at pH 3 and 7. For the PAAMA surface at pH 3, the charge density across the carboxyl groups is reduced and the response which is similar to the unmodified pore is recorded, Table 5.4. Increasing the pH to 7 for the PAAMA pores increases the negative charge density of the PAAMA pore wall, which is then observed as a decrease in current flow at positive potentials and a current rectification of 1.98. The unmodified pore shows a current rectification of 0.8 at a pH of 3, indicating the surface groups have become protonated.

Table 5.4 Rectification ratios for pores with different surface chemistry as a function of pH. Recorded in 5 mM KCl. ± one standard deviation from the mean of three pores.

pH	Unmodified Pore	HMW PEI	PAAMA
3	0.80±0.04	0.31±0.07	0.73±0.13
7	1.32±0.12	0.52±0.09	2.67±0.26

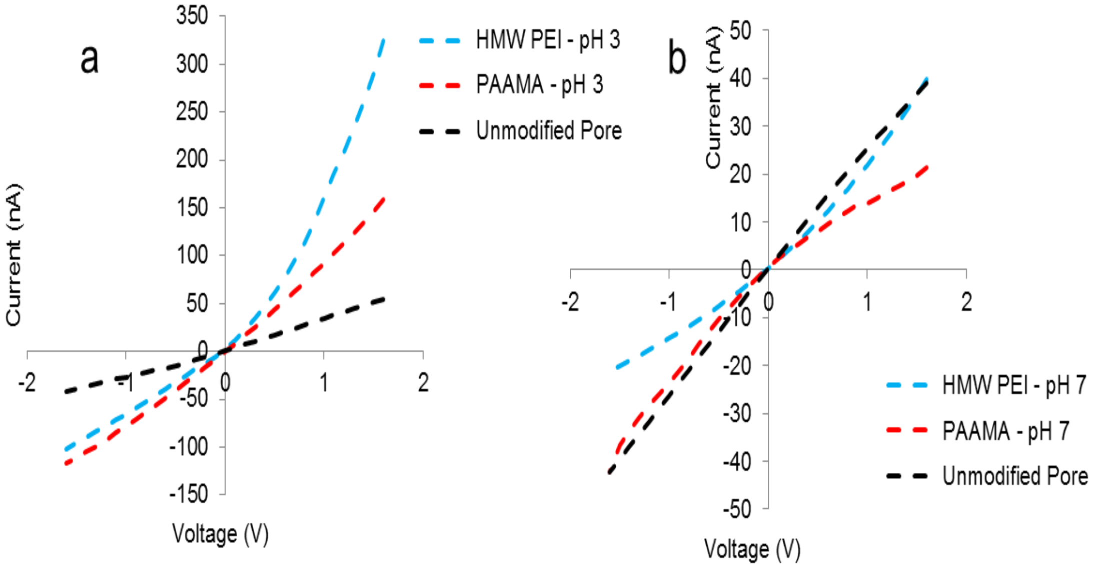

Figure 5.10 a) I-V curves for a unmodified pore, a PAAMA (two complete bilayers) and PEI (1.5 bilayers). Obtained at 45 mm Stretch, pH 3 and 5 mM KCl. b) I-V curves for a unmodified pore, PAAMA (two complete bilayers) and PEI (1.5 bilayers). Obtained at 45 mm Stretch, pH 7 and 5 mM KCl.

The current flow through the pore will have two contributing factors; the electroosmotic flow, EOF, across the pore surface and migration of ions through the centre. EOF has been shown to be a small contributing factor to current rectification in smaller pores.[3] The ion enrichment zone at the opening of the pore is sufficient enough to observe current rectification in the larger nanopores used in TRPS. This illustrates that the electrical double layer does not need to extend over the pore opening for rectification to be observed. The ion enrichment effect has also been attributed to biphasic pulse behaviour in TRPS.[24,25] In this setup, the large top surface of the nanopore is also modified and future work may be needed to ascertain which has the largest impact on current rectification. The reported setup however allows for the easy modification of the pore wall, and by using different polymers or different thickness's it may be possible to further tune these larger pores to be ion selective.

5.4.1 Modification of the pore walls with ssDNA

The main motivation for modifying the pore walls with the LbL polymers was to introduce a functionality to which biomolecules could be easily coupled to the pore wall. Similar aspirations have led to the modification of pores with Au allowing DNA to be placed along the pore wall or utilisation of the carboxyl groups.[26,27] Our method of immobilisation uses EDC chemistry placing the DNA across the top surface and pore surface, shown schematically in Figure 5.11a.

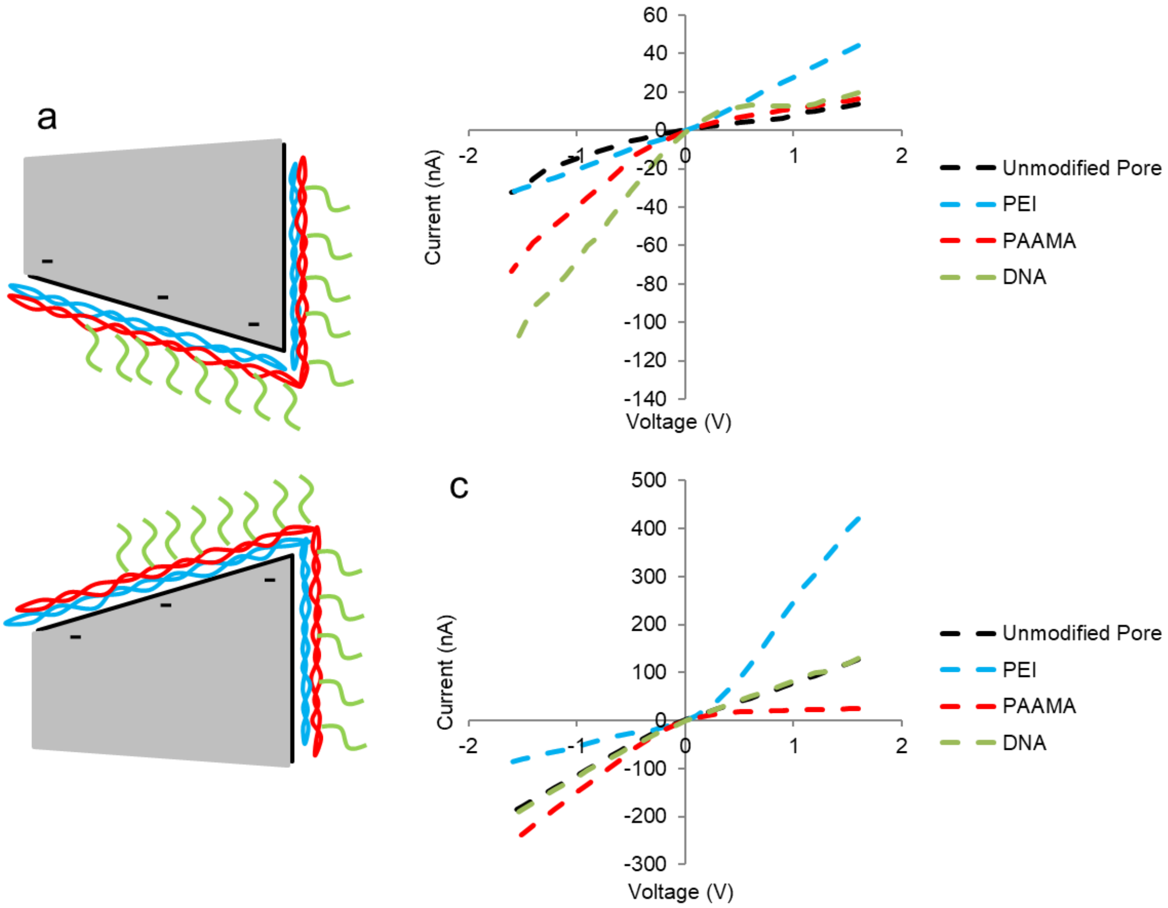

Figure 5.11 a) Schematic of the DNA modified pore. b) and c) current – voltage (I-V) curves recorded in 5 mM and 50 mM KCl respectively.

Shown in Figure 5.11 are (*I*-*V*) curves showing the bilayer modification and then the DNA modification. Figure 5.11a shows the pore rectifications recorded in 5 mM and Figure 5.11b in 50 mM. Only one bilayer was immobilised on the pore wall when DNA was added. In this case, it has introduced the carboxyl groups needed for DNA immobilisation and reduced the number of preparation stages. At higher ionic strengths, >50 mM KCl, the DNA modified pores do not exhibit current rectification. The reduction in rectification may be due to the high number of DNA strands on the pores surface and the counter ion condensation effect that is observed at surfaces with high charge densities.

The pores were incubated with the target VEGF protein and the subsequent incubation of the VEGF results in a strong rectification; shown in Figure 5.12. The (*I*-*V*) curves for 5 mM and 50 mM are shown, Figure 5.12b and c. The decrease in currents at positive potentials was shown to be specific to the aptamer-VEGF interaction in the presence of BSA Figure 5.13. Each pore at each ionic strength shows the same trend at positive voltages, however at lower negative voltages there is variation between each pore and each ionic strength. Difference in each pore will arise from different sizes, shape, polymer and DNA coverage. Figure 5.7b shows hysteresis at negative voltages and can be used to explain the difference between Figure 12a and b. To ensure the current is stable before taking measurements, current-voltage scans may need to be performed prior to analysis.

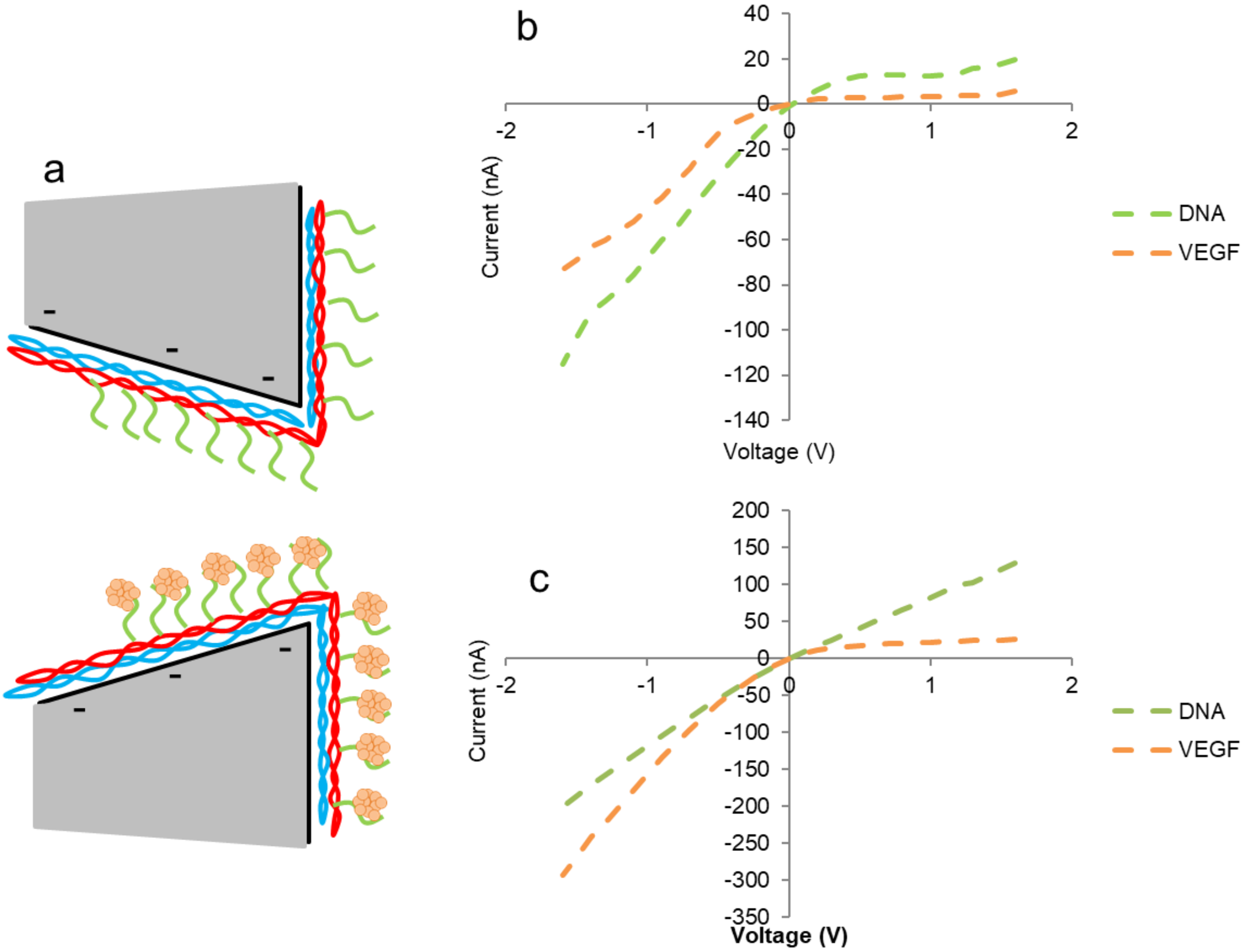

Figure 5.12 a) Schematic of the DNA modified pore interacting with VEGF. b) and c) Current – Voltage (I-V) recorded for DNA modified pore and after incubation with 50 nM VEGF in 5 and 50 mM respectively.

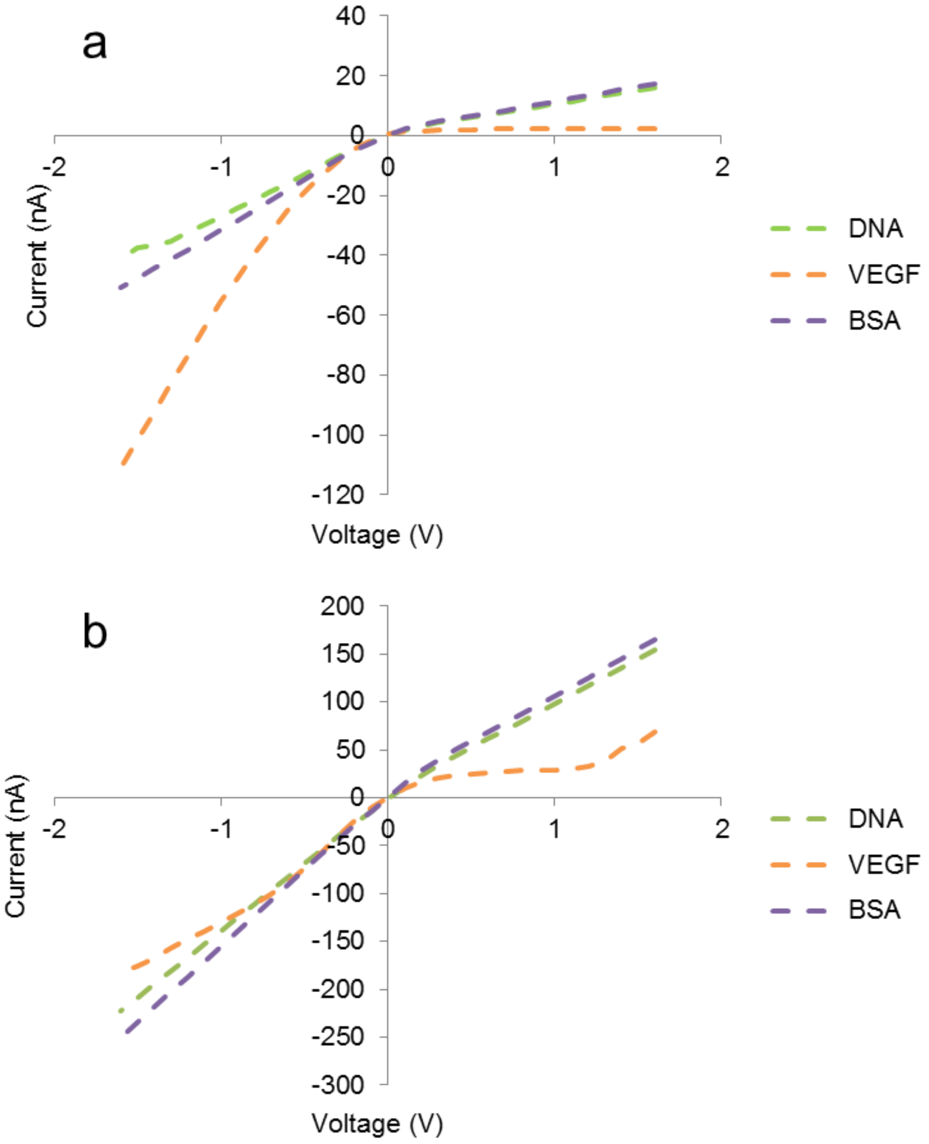

Figure 5.13 Current – Voltage (I-V) curves recorded for a DNA modified pore, BSA was incubated with the pore, followed by VEGF. a) 5 mM b) 50 mM KCl.

The hypothesis for the observed rectification behaviour relies upon the high pI of VEGF (8.2), and that the protein is positively charged. The presence of the positively charged protein at the pore mouth will repel the cation flow through the nanopore. In addition to this, the folding of the aptamer into a tertiary structure to bind to the VEGF must require an increase in counter ions to stabilise the structure, and these two factors contribute to a decrease in conductivity at the pore mouth at positive potentials.

Figure 5.14 shows the concentration dose response of the DNA modified pore at 5 mM KCl. As the concentration of VEGF is increased the current measured at 1.6 V decreases, and appears to saturate or remain unchanged beyond 5nM. The rectification ratios for the 5 mM KCl experiment are given in Table 5.5. The rectification ratios increase from 50 pM upwards, however a small decrease is seen at 5 pM. These differences need to be explored further and may be due to the top surface of the pore being modified which could have a role in the differences seen in rectification behaviour.

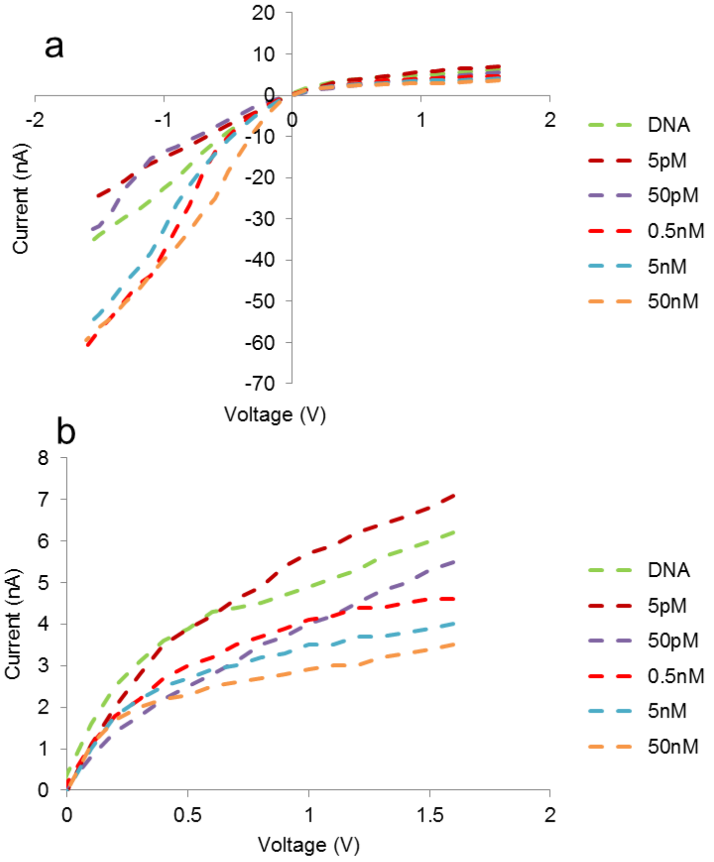

Figure 5.14 a) Current – Voltage (I-V) curves recorded with different concentrations of VEGF at 5 mM KCl. b) Magnified section of currents recorded between 0 – 1.6V.

Table 5.5 Rectification ratios for varying concentration of VEGF recorded in 5 mM KCl.

VEGF Concentration	Rectification Ratio
5 pM	3.63
50 pM	6.04
0.5 nM	13.28
5 nM	14.00
50 nM	17.00
DNA	5.88

The same pore and experiments were ran in 50 mM KCl and here, Table 5.6, there is an increase in rectification ratio seen with 5 pM VEGF. At higher ionic strength the measured rectification is affected less by surfaces changes due to the smaller electrical double layer. Further experiments would need to be carried out to establish a suitable electrolyte for measuring the analyte. The detection of the VEGF at such low levels, when compared to RPS, may be aided by the inherent nature of the membrane to pre-concentrate cations in the pore mouth.

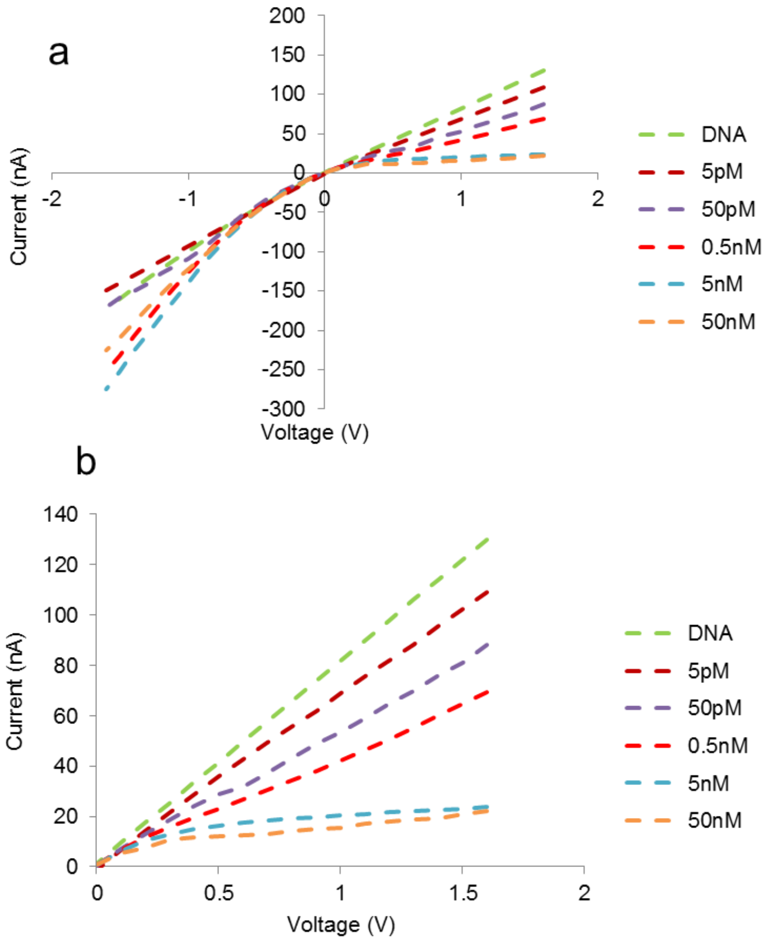

Figure 5.15 a) Current – Voltage (I-V) curves recorded with different concentrations of VEGF at 50 mM KCl. b) Magnified section of currents recorded between 0 – 1.6V.

Table 5.6 Rectification ratios of varying VEGF concentration recorded in 50 mM KCl.

VEGF Concentration	Rectification Ratio
5 pM	1.36
50 pM	1.93
0.5 nM	3.64
5 nM	11.60
50 nM	10.12
DNA	1.33

5.5 Conclusions

Presented here is the first LbL modification of polyurethane pores which allows a pH, and ionic strength controlled current flow. The strong rectification on pores of the dimension, circa 800 nm indicates that the electrical double layer does not need to extend significantly across the pore opening. The LbL assay reported here offers a simple and reusable method for modifying the surface chemistry of the pores. The introduction of polyelectrolytes offers a pH and ionic strength dependent rectification behaviour and is the first reported method on such a system. The rectification properties of the pore allowed the modification process of the pore to be followed by measuring the change in charge. The change in charge as each polyelectrolyte was introduced to the pore gave a clear signal that the modification had been a success.

The LbL assembly is stable for several days that allows for DNA-modification of the pore wall via standard carbodiimide chemistry. This method could be developed further by controlling the modification of the pore wall so specific binding sites could be incorporated for a variety of analytes. It is acknowledged that further studies are required to access the effects of the modification of the top surface of the pore has on the rectification mechanism. The protein binding to the top surface could lead to differences in rectification compared to the protein binding within the pore interior. A method would need to be developed and carefully controlled to ensure only the interior of the pore was modified. The electroosmotic flow has been shown to be a small contributing factor to current rectification in smaller pores, however in the larger pores used in TRPS, the total contribution of the electroosmotic flow would need to be further investigated.

5.6 References

1. Blundell, E. L. C. J., Mayne, L. J., Christie, S. D. R. & Platt, M. Protein Detection Using Tunable Pores: Resistive Pulses and Current Rectification. *Faraday Discuss.* **193,** 487–505 (2016).

2. Siwy, Z. S. Ion-current rectification in nanopores and nanotubes with broken symmetry. *Adv. Funct. Mater.* **16,** 735–746 (2006).

3. White, H. S. & Bund, A. Ion Current Rectification at Nanopores in Glass Membranes. *Langmuir* **24,** 2212–2218 (2008).

4. Siwy, Z. *et al.* Ion transport through asymmetric nanopores prepared by ion track etching. *Nucl. Instruments Methods Phys. Res. Sect. B Beam Interact. with Mater. Atoms* **208,** 143–148 (2003).

5. Siwy, Z. *et al.* Rectification and voltage gating of ion currents in a nanofabricated pore. *Europhys. Lett.* **60,** 349–355 (2002).

6. Lan, W. J., Holden, D. A. & White, H. S. Pressure-dependent ion current rectification in conical-shaped glass nanopores. *J. Am. Chem. Soc.* **133,** 13300–13303 (2011).

7. Chen, P. *et al.* Atomic layer deposition to fine-tune the surface properties and diameters of fabricated nanopores. *Nano Lett.* **4,** 1333–1337 (2004).

8. Siwy, Z., Heins, E., Harrell, C. C., Kohli, P. & Martin, C. R. Conical-nanotube ion-current rectifiers: The role of surface charge. *J. Am. Chem. Soc.* **126,** 10850–10851 (2004).

9. Pérez-Mitta, G. *et al.* Noncovalent functionalization of solid-state nanopores via self-assembly of amphipols. *Nanoscale* **8,** 1470–1478 (2016).

10. Ali, M. *et al.* Metal ion affinity-based biomolecular recognition and conjugation inside synthetic polymer nanopores modified with iron-terpyridine complexes. *J. Am. Chem. Soc.* **133,** 17307–17314 (2011).

11. Lepoitevin, M., Bechelany, M., Balanzat, E., Janot, J. M. & Balme, S. Non-Fluorescence label protein sensing with track-etched nanopore decorated by avidin/biotin system. *Electrochim. Acta* **211,** 611–618 (2016).

12. Siwy, Z. *et al.* Protein biosensors ’based on biofunctionalized conical gold nanotubes. *J. Am. Chem. Soc.* **127,** 5000–5001 (2005).

13. Nonaka, Y., Sode, K. & Ikebukuro, K. Screening and improvement of an anti-VEGF DNA aptamer. *Molecules* **15,** 215–25 (2010).

14. Vogel, R., Anderson, W., Eldridge, J., Glossop, B. & Willmott, G. A variable pressure method for characterizing nanoparticle surface charge using pore sensors. *Anal. Chem.* **84,** 3125–3131 (2012).

15. Steitz, B. *et al.* Characterization of PEI-coated superparamagnetic iron oxide nanoparticles for transfection: Size distribution, colloidal properties and DNA interaction. *J. Magn. Magn. Mater.* **311,** 300–305 (2007).

16. O’Mahony, J. J., Platt, M., Kilinc, D. & Lee, G. Synthesis of Superparamagnetic Particles with Tunable Morphologies: The Role of Nanoparticle–Nanoparticle Interactions. *Langmuir* **29,** 2546–2553 (2013).

17. Yang, Y.-H., Haile, M., Park, Y. T., Malek, F. A. & Grunlan, J. C. Super Gas Barrier of All-Polymer Multilayer Thin Films. *Macromolecules* **44,** 1450–1459 (2011).

18. Fu, J. *et al.* pH-Amplified Exponential Growth Multilayers: A Facile Method to Develop Hierarchical Micro- and Nanostructured Surfaces. *Langmuir* **25,** 672–675 (2009).

19. Yang, Y.-H., Bolling, L., Haile, M. & Grunlan, J. C. Improving oxygen barrier and reducing moisture sensitivity of weak polyelectrolyte multilayer thin films with crosslinking. *RSC Adv.* **2,** 12355–12363 (2012).

20. Podsiadlo, P. *et al.* Exponential Growth of LBL Films with Incorporated Inorganic Sheets. *Nano Lett.* **8,** 1762–1770 (2008).

21. Kulkarni, A., Diehl-Jones, W., Ghanbar, S. & Liu, S. Layer-by-layer assembly of epidermal growth factors on polyurethane films for wound closure. *J. Biomater. Appl.* **29,** 278–290 (2014).

22. Jozwiak, A. B., Kielty, C. M. & Black, R. A. Surface functionalization of polyurethane for the immobilization of bioactive moieties on tissue scaffolds. *J. Mater. Chem.* **18,** 2240–2248 (2008).

23. Siwy, Z., Heins, E., Harrell, C. C., Kohli, P. & Martin, C. R. Conical-Nanotube Ion-Current Rectifiers: The Role of Surface Charge. *J. Am. Chem. Soc.* **126,** 10850–10851 (2004).

24. Weatherall, E. & Willmott, G. R. Conductive and biphasic pulses in tunable resistive pulse sensing. *J. Phys. Chem. B* **119,** 5328–5335 (2015).

25. Mayne, L. J., Christie, S. D. R. & Platt, M. A tunable nanopore sensor for the detection of metal ions using translocation velocity and biphasic pulses. *Nanoscale* **8,** 19139–19147 (2016).

26. Ali, M., Nasir, S. & Ensinger, W. Bioconjugation-induced ionic current rectification in aptamer-modified single cylindrical nanopores. *Chem. Commun.* **51,** 3454–3457 (2015).

27. Nguyen, G., Howorka, S. & Siwy, Z. S. DNA Strands Attached Inside Single Conical Nanopores: Ionic Pore Characteristics and Insight into DNA Biophysics. *J. Membr. Biol.* **239,** 105–113 (2011).

6 Simultaneous metal ion detection using DNA aptamers and nanoparticles

This chapter presents a multiplexed metal ion assay utilising aptamer modified nanoparticles for the detection of the toxic heavy metal ions, lead and mercury, using particle translocation velocities. This work builds upon knowledge of developing metal ion sensors using nanopores which has been demonstrated in Chapter 4. Aptamer-modified nanomaterials provide a simple, yet powerful sensing platform when combined with resistive pulse sensing technologies. Aptamers adopt a more stable tertiary structure in the presence of a target analyte, which results in a change in charge density and velocity of the carrier particle. In practice the tertiary structure is specific for each aptamer and target, and the strength of the signal varies with different applications and experimental conditions. Measuring the velocity of aptamer-modified nanomaterials as they traverse the pore provides information on their charge state and densities. To help understand how the aptamer structure and charge density effects the sensitivity of aptamer-RPS assays, here we study two metal binding aptamers. This creates a sensor for the simultaneous detection mercury and lead ions with nM sensitivity that is capable of being run in a range of electrolyte concentrations, equivalent to river to seawater conditions.

6.1 Aims and Objectives

Chapter 4 shows the potential for TRPS to be used in metal ion sensing. Often more than one metal ion contaminant is present in solution, this chapter aims to develop a method for detecting more than one metal ion simultaneously. TRPS can easily distinguish particles based on their size, two particles of different sizes have two different aptamers grafted to their surfaces for the detection of Pb^{2+} and Hg^{2+} and each analyte can then be measured simultaneously. Each assay will be developed separately initially to determine detection parameters in a range of ionic strengths.

6.2 Introduction

In recent years, oligonucleotides have attracted attention for the detection of metal ions.[1] Several DNA-based sensors have been reported for various metal ions including Hg^{2+}, [,2,3] Pb^{2+},[4,5,6] UO^{2+},[7,] and Cu^{2+}[8,]. DNA aptamers for binding metal ions have shown to be specific and highly sensitive to their target ion. The DNA-based sensors often incorporate fluorescence,[10-13] colorimetric[14,15] and electrochemical detection[16]. The DNA aptamers are often grafted to a surface such as nanoparticles and graphene sheets.[17,18] While each platform has its merits, other present ions often interfere with selectivity. Potassium ions (K^+) can compete with lead ions (Pb^{2+}) for G-quadruplex forming aptamers.[19] This is a draw back when detecting ions in solutions with high potassium levels such as blood and sea water.[20,21] Detection methods often only focus on one heavy metal contaminant when one or more contaminant may be present. Chung et al.[20] reported the dual fluorescent detection of Pb^{2+} and Hg^{2+} in serum; however, each aptamer used requires a different fluorescent label. It is highly desirable to develop a system that is selective, sensitive and easily adaptable to a range of target ions for simple multiplex detection.

The work presented in this chapter demonstrates the ability of TRPS to distinguish between two different particle sizes to develop a method for the simultaneous detection of lead and mercury. Heavy metals, such as mercury and lead, are highly toxic and dangerous pollutants. Lead and mercury are common environmental contaminants which pose a risk to human health. They accumulate in plants and animals and thus can enter the food chain. Even in low concentrations these metal ions can cause adverse side effects. Therefore, developing sensors both mercury and lead has been a long-standing focus of research.

6.3 Experimental

6.3.1 Method and Materials

The following chemicals were purchased from Sigma Aldrich, UK, poly(ethyleneimine), PEI, (Mw 750 000 g mol^{-1}, analytical standard, 50 % wt., P3143), poly(acrylic acid-co-maleic acid) (PAAMA, Mw ~3000 g mol^{-1} 50 % wt., 416053), copper (II) chloride dihydrate ($CuCl_2.2H_2O$, reagent grade, 221783), lead(II) nitrate ($Pb(NO_3)_2$, ACS reagent, ≥99.0%, L7281), mercury (II) chloride ($HgCl_2$, ACS reagent, ≥99.5%, M6529), sodium hydroxide (NaOH, reagent grade, ≥98%, S5881), (2-(N-Morpholino)ethanesulfonic acid hydrate (MES hydrate, ≥99.5 %, M2933) and N-Hydroxysulfosuccinimide sodium salt (NHS, ≥98.5 %, 56485). Tunable conical pores (NP200s) and carboxylated polystyrene particles (210 nm in diameter, denoted CPC200) were purchased from Izon Science, Christchurch, NZ. The following chemicals were purchased from Fisher Scientific, UK, potassium chloride (KCl, >99 %, P/4240/60), sodium chloride (NaCl, analytical grade, S/3160/60) and potassium hydroxide (KOH, 0.1 M, >85 %, P/5600/60).Hydrochloric acid (HCl, 0.5 M, 37 %) was purchased from VWR, UK.1-ethyl-3-(3-dimethylaminopropyl)carbodiimide hydrochloride (EDC, 22980) was purchased from Thermo Scientific, UK.

Reagents were prepared in deionised water with a resistivity of 18.2 MΩ cm (Maxima). pH of solutions were altered using HCl and KOH. The solutions were measured using a Mettler Toledo easy five pH meter with a Mettler Toledo InLab micro electrode.

6.3.2 Custom DNA Oligonucleotides

The oligonucleotides used in this study were purchased as lyophilised powders from Sigma Aldrich, UK. The sequences were synthesised with an amine functional group at the 3' end: 5'-TTCTTTCTTCGCGTTGTTTGTT-3' (mercury binding aptamer),[2] 5'-GGAAGGTGTGGAAGG-3' (lead binding aptamer, TBAA),[4] 5'-GGAAAATGTGGAAGG-3' (lead control aptamer).

6.3.3 Particles

Superparamagnetic particles were purchased from Ademtech, France (150 nm in diameter, 0211). The particles were modified using PEI and PAAMA to ensure a carboxyl group was present on the particles. Particles were taken from stock (50 µL) and suspended in PEI (1 mL, 5% in H_2O). The solution was placed on the rotary wheel for 30 minutes. The solution was vortexed for 5 minutes at 10 000 rpm, the PEI solution removed from the particles and replaced with water. The sample was vortexed and sonicated until the particles were fully dispersed. This wash step was repeated twice to ensure all excess PEI had been removed. The PEI coated particles were suspended in PAAMA (5% in 50 mM NaCl) for 30 minutes and placed on the rotary wheel. The same process for removing the excess PEI was used. The particles were then stored at 2 – 4 ºC in water. Carboxyl polystyrene particles (303 nm in diameter,11839) were purchased from Bangs Laboratories, US and used without any modification.

Each aptamer was dissolved in 100 mM MES buffer (pH 5.7) containing 1 mg ml^{-1} EDC and 1 x 10^{10} carboxylated particles/ mL. The final concentration of DNA was 410 nM. The solution containing the particles was placed on the rotary wheel for 1 hour. To remove an excess DNA, the solutions containing the magnetic 150 nm particles were placed in a MagRack (Life Sciences). After 5 minutes, the particles had formed a visible cluster and the solution was removed and replaced with an equal volume of NaCl (20 – 500 mM). The solutions containing the 300 nm particles were centrifuged for 10 minutes at 10 000 rpm. The solution was removed from the pellet of particles and replaced with equal volume of NaCl (20 – 500 mM).

6.3.4 Metal Ion Extraction

A lead (II) solution (1 µM) was prepared from $Pb(NO_3)_2$ in a range of ionic strengths (20 – 500 mM NaCl). The solution was further diluted in the same ionic strength to give a range of lead concentrations (0.05 – 100 nM). A 0.1 nM Lead (II) solution was prepared in KCl (500 mM). A mercury (II) solution (1000 nM) was prepared from $HgCl_2$ in a range of ionic strengths (20 – 500 mM NaCl). The solution was further diluted in the same ionic strength to give a range of mercury concentrations (20 – 500 nM). A copper (II) solution (1 µM) was prepared from $CuCl_2.H_2O$ in NaCl (100 mM).

Aptamer modified particles (1 x 10^9 particles mL^{-1}) were added to the solutions of desired metal ion concentration and ionic strength. The solutions were vortexed for 30 s and placed on the rotary wheel for 1 hour.

6.3.5 Multiplex Detection Assay

150 nm particles with Hg binding aptamer and 300 nm particles with lead binding aptamer were prepared as described above. The functionalised particles were placed into vials at a concentration of 1 x 10^9 particles mL^{-1} and lead (20 nM) and mercury (20 nM) were added. The samples were placed on the rotary wheel for 1 hour.

6.3.6 TRPS Set-up

All measurements were conducted using the qNano (Izon Science, NZ) combing tunable nanopores with data capture and analysis software, Izon Control Suite v.3.1. The lower fluid cell contains the electrolyte (75 µL). The particle is suspended in the same electrolyte and placed in the upper fluid cell (40 µL). Prior to analysis all samples were vortexed and sonicated for 30 s. After each sample run, the system was washed by placing 40 µL of electrolyte into the upper fluid cell several times with various pressures applied to ensure there were no residual particles remaining and therefore no cross contamination between samples.

6.3.7 Particle Translocation Velocity

The same method for calculating the relative particle translocation velocity through the pore was presented previously in copper chapter. Briefly. the method uses the resistive pulse to calculate the relative velocity. For each blockade, the time at which the peak occurs is defined as $T_{1.0}$ (time at 100% of peak magnitude) and the maximum magnitude of the pulse (relative to the local baseline resistance) is recorded as dRmax. The duration from $T_{1.0}$ to each section is defined at $T_{0.60}$, $T_{0.50}$, $T_{0.40}$ and $T_{0.30}$. When the proportional blockade magnitude is equal for any given particles (small or large), these particles are at the same position within the pore. Hence, the relative magnitude is an indicator of the particle position within the pore. The velocities reported in this chapter are all measured at $1/T_{0.50}$.

6.4 Results and Discussion

Carboxyl particles were modified with the chosen aptamers for the lead and mercury detection and the particles were measured using TRPS before and after modification. The speed at which the particles traverse the pore can be related to the surface charge. Here, this is dominated by the carboxyl groups and the negative phosphate backbone after modification. The particles are negatively charged and therefore travel towards to cathode. Figure 6.1 shows the average velocities for the 150 nm carboxyl particles across a range of electrolyte concentrations. The particle velocity is denoted ms^{-1} and is the time taken for the particle to travel 50 % of the way through the nanopore ie $T_{0.50}$. The speed of the particle increases as the supporting electrolyte concentration is lowered. The measured particle speed is related to the electrophoretic mobility and is a function of the double layer structure which changes as ionic strength is changed. As the electrolyte concentration is reduced the shielding around the particles is reduced leading to an increased electrophoretic mobility through the pore. The addition of DNA onto the particles surface was measured using the particle's translocation speed.

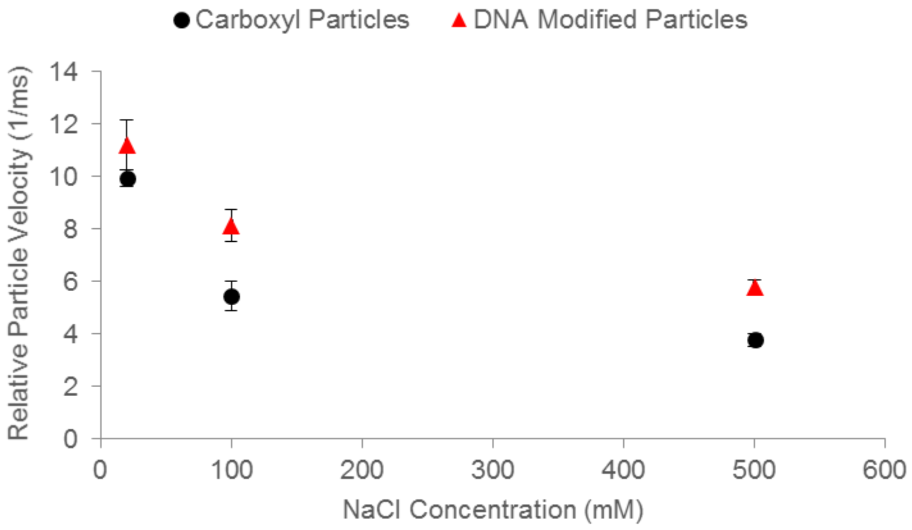

Figure 6.1 150 nm carboxyl nanoparticles (black circles) were modified with the lead binding aptamer (red triangles). Samples were analysed using an NP200 pore, pH ~6, stretch 45.50 mm. Error bars represent the standard deviation of three experiments.

The particles modified with DNA have a greater velocity than those without. This is attributed to the phosphate groups carrying a negative charge and increasing the charge density on the surface of the particle. A benefit of the TRPS system is particle-by-particle analysis. Figure 6.2 shows the distribution speeds of carboxyl particles and DNA modified particles measured in 100 mM NaCl. A shift in the mean values from 5.5 ms^{-1} to 8.1 ms^{-1} at 100 mM is recorded, as well a shift in the distributions.

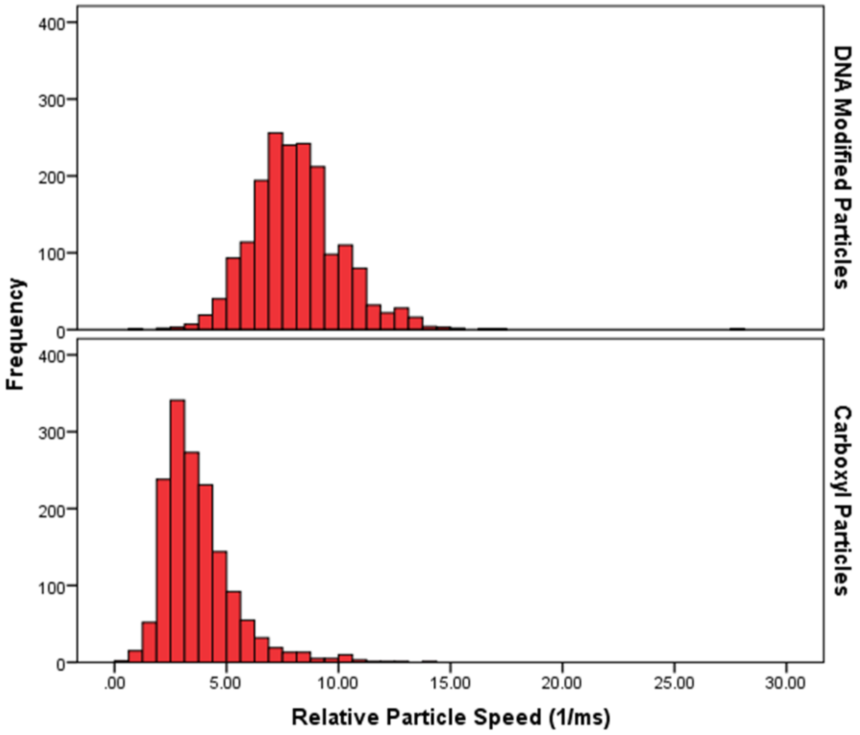

Figure 6.2 Particle velocity distributions of 150 nm carboxyl and lead binding aptamer modified particles. Samples were analysed on a NP200 pore, pH ~6, 100 mM NaCl and a 45.50 mm stretch.

6.4.1 Detection of Lead

Oligonucleotides which are G rich are known to form G-quadruplex structures in the presences of specific metal ions such as K^+ and Na^+.[22,23] It was reported that the binding of Pb^{2+} to a thrombin binding aptamer (TBA) was stronger than the binding to monovalent cations.[4] The strong association of Pb^{2+} has made it possible to develop highly sensitive sensors.[5] The presence of monovalent ions such as Na^+ and K^+ may interfere with the detection of Pb^{2+} when using a G-rich oligonucleotide. To overcome the potential interference from Na^+ and K^+ a modified thrombin binding aptamer (TBAA) is used in this work. TBAA has been used previously to bind Pb^{2+} with no interference from K^+ ions.[4,20] The TBAA aptamer has an affinity of 10^7 M^{-1} towards Pb^{2+} and it has been shown to not fold into the G-quadruplex in the presence of monovalent cations such as K^+ and Na^+.[4,24]The TBAA binds a single Pb^{2+} ion in the inter quartet region with a coordination number of 8, Figure 6.3.[4]

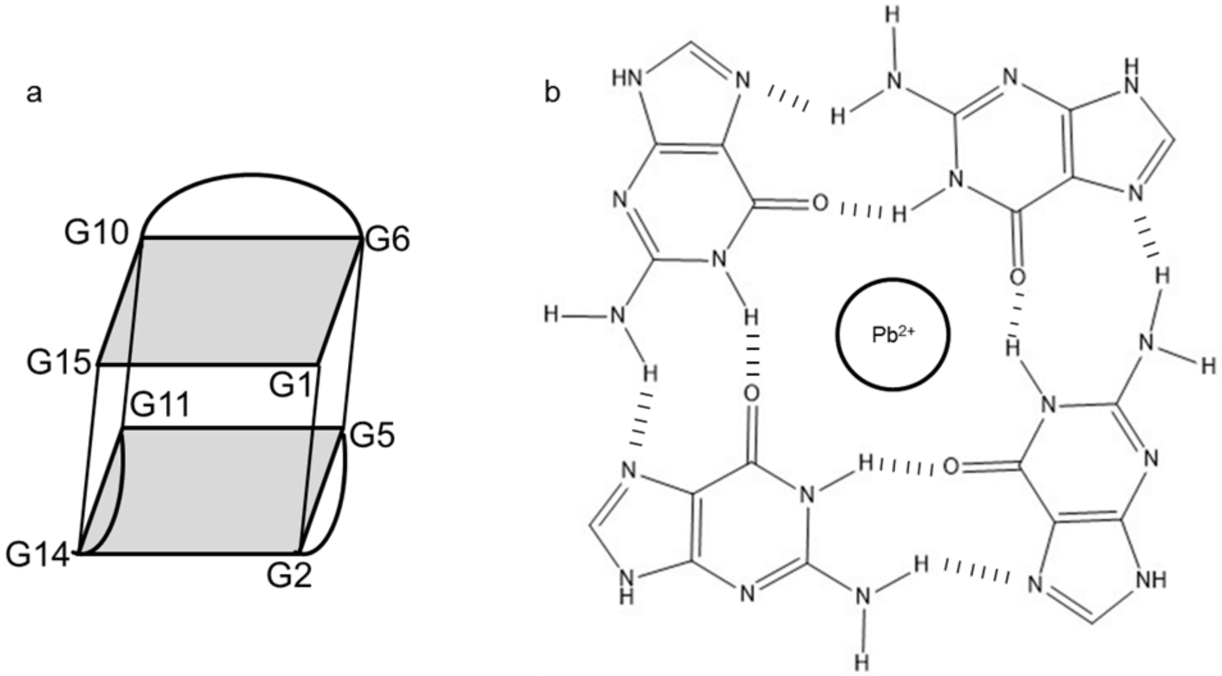

Figure 6.3 a) The folding of TBAA aptamer into the G-quadruplex structure with two guanine quartets formed. b) A guanine quartet formed with Pb^{2+} bound in the centre of the two quartets.

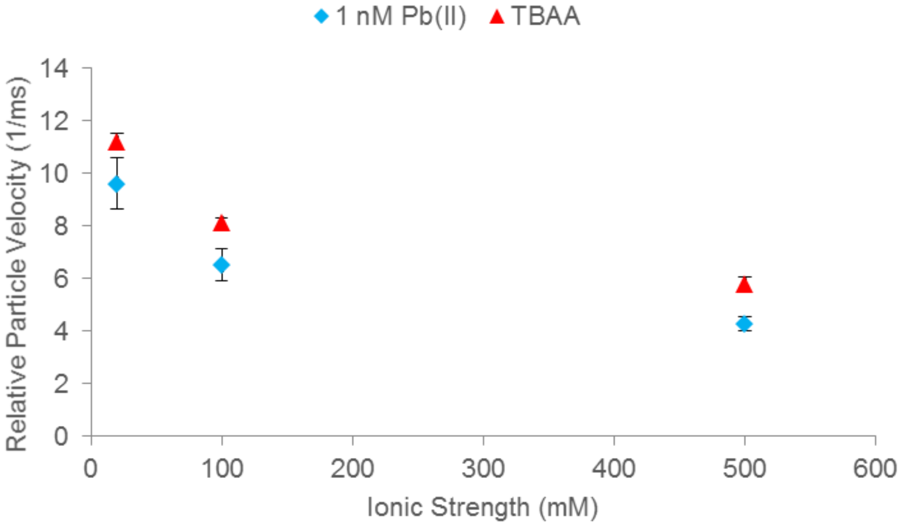

Figure 6.4 Aptamer modified (TBAA) particles (red triangles) incubated with 1 nM Pb^{2+}(blue diamonds) for 1 hour. Samples were analysed using an NP200 pore, pH ~6, stretch 45.50 mm. Error bars represent the standard deviation of three experiments.

Carboxyl particles modified with TBAA aptamer were incubated with 1 nM Pb^{2+} in a range of ionic strengths (20 -500 mM NaCl) for 1 hour. Following the incubation, the particles were analysed using TRPS. The velocities of the particles across a range of electrolyte concentrations at pH 6 are shown in Figure 6.4 (for comparison, the DNA modified particle data is reproduced). Particles with Pb^{2+} bound have a lower translocation velocity compared to those without. When the Pb^{2+} ion binds, the DNA undergoes a conformational change from a single strand to a G-quadruplex. The changes in particle velocity can be attributed to the changes in DNA structure on the surface of the particle.

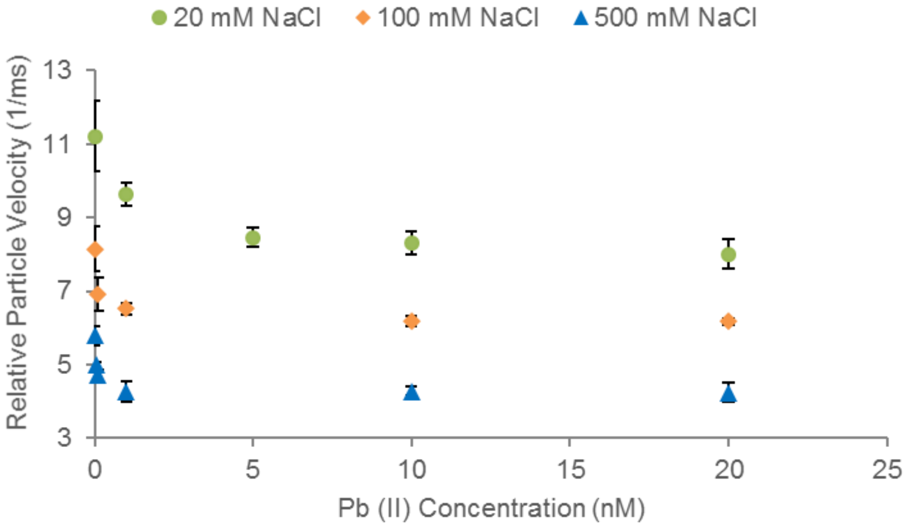

Figure 6.5 Aptamer modified particles incuabted in a range of Pb^{2+} cocentrations and analysed in three different NaCl concentrations, 20 mM NaCl (green circles), 100 mM NaCl (orange diamonds) and 500 mM NaCl (blue triangles). Samples were analysed using an NP200 pore, pH ~6, stretch 45.50 mm. Error bars represent the standard deviation of three experiments.

The TBAA modified particles were incubated with a range of Pb^{2+} concentrations and electrolyte concentrations, Figure 6.5. Electrolyte concentrations were used to match real life samples containing Na^+. The concentrations used were in the range of sewage water (~ 20 mM), river water (~ 50 mM), human body (~ 140 mM) and sea water (~ 500 mM). The concentrations of Pb^{2+} which show a significant velocity change from the blank (DNA modified particle with no Pb^{2+}) differed in each electrolyte; 1 nM, 0.1 nM and 0.05 nM for 20 mM, 100 mM and 500 mM respectively. The recorded differences in velocities between the blank and particles with Pb^{2+} bound are different in each electrolyte. This is due to the standard deviations from three samples of the blank being larger in lower ionic strengths. In 20 mM NaCl, the standard deviation of the blank is 0.95, this reduces to 0.60 in 100 mM NaCl and 0.26 in 500 mM NaCl. In lower electrolyte concentrations, there is less shielding around the particle's charge, therefore any differences in charge between the particles is detected. The distribution of the particle velocities, shown in Figure 6.6, shows a broadening of velocity with lowering electrolyte concentration.

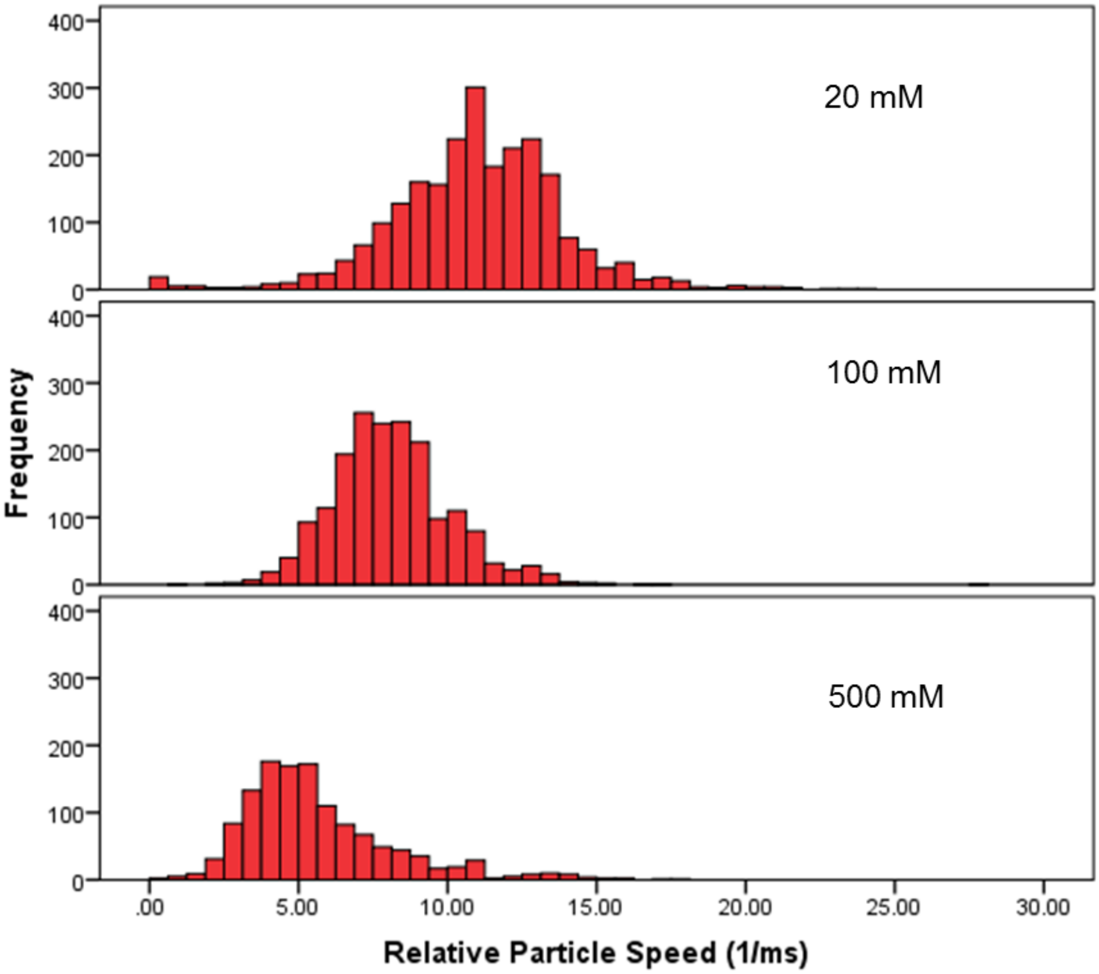

Figure 6.6 Particle velocity distributions of lead binding aptamer modified particles recorded in 20, 100 and 500 mM NaCl. Samples were analysed using an NP200 pore, pH ~6, stretch 45.50 mm.

To show there is no interference from K^+ ions to form the G-quadruplex, the particles were measured in both 500 mM NaCl and KCl and incubated with 0.1 nM Pb^{2+}. There were no differences in the velocities recorded when compared with 500 mM NaCl, Figure 6.7. To confirm the binding of Pb^{2+} to the G-quadruplex, a control aptamer with two G bases replaced with A bases was used. The aptamer modified particles were incubated with 1 µM Pb^{2+}. The aptamer with and without the Pb^{2+} show no differences in velocity, Figure 6.8. The removal of the G bases would disrupt the formation of the G-quadruplex and stop the formation of the guanine quartets shown in Figure 6.3.

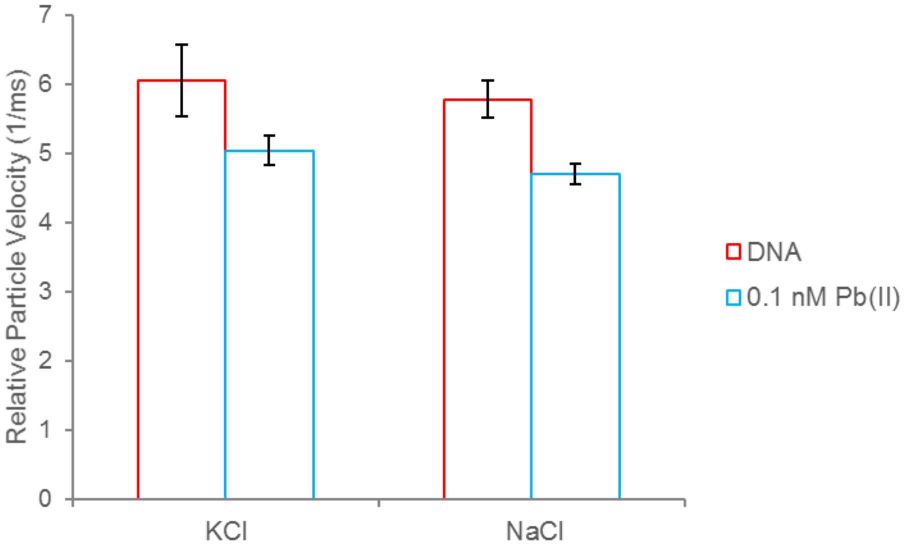

Figure 6.7 Aptamer modified particles incubated with 0.1 nM Pb^{2+} and measured in 500 mM NaCl and 500 mM KCl. Samples were analysed using an NP200 pore, pH ~6, stretch 45.50 mm. Error bars represent the standard deviation of three experiments.

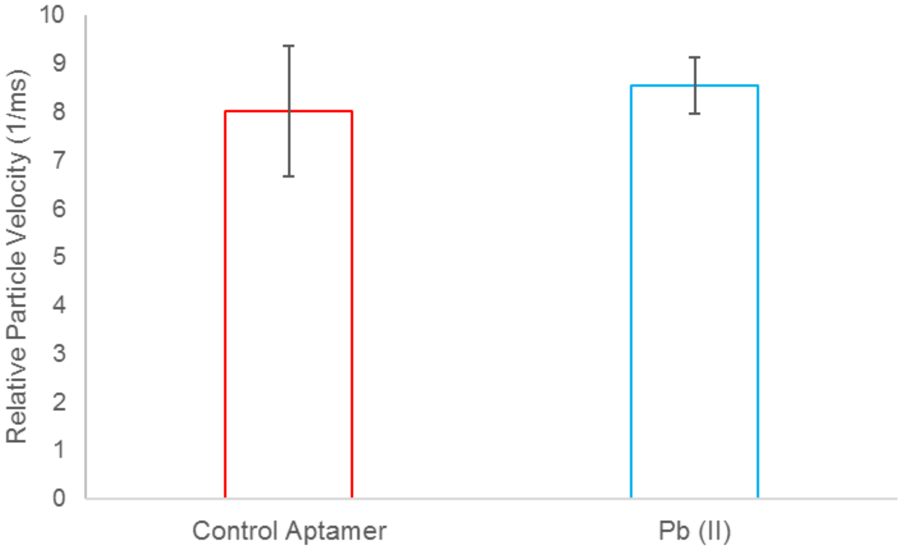

Figure 6.8 Particles modified with a control aptamer and incuabted with 1 µM Pb^{2+}. Samples were analysed using an NP200 pore, pH ~6, stretch 45.50 mm. Error bars represent the standard deviation of three experiments.

6.4.2 Detection of Mercury

In the absence of Hg^{2+} the DNA aptamer is single stranded and immobilised on the surface of the nanoparticle. When Hg^{2+} ions are present the DNA aptamer folds into a hairpin structure due to the T-Hg^{2+}-T coordination,[2] Figure 6.9. The T-T mismatch is more stable than a Watson Crick T-A pairing[25] and has an affinity of 10^6 M^{-1} for each T-Hg-T pair bonding.[26] This structural change and addition of metal ions changes the particles velocity through the nanopore.

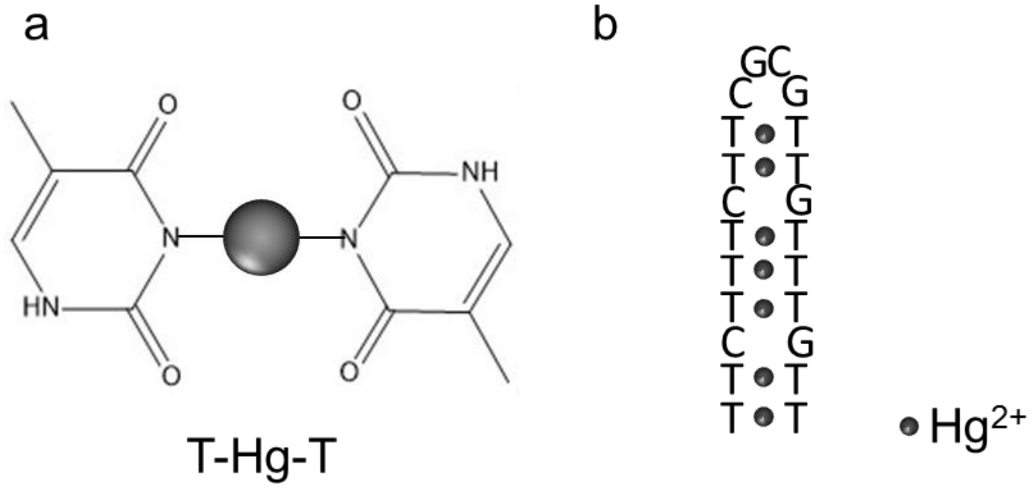

Figure 6.9 a) Thymine base pairs stabilised through binding with Mercury (Hg^{2+}) ions. b) Structure of mercury binding aptamer upon binding with Hg^{2+}.

The Hg^{2+} binding aptamer modified particles were incubated with 50 nM Hg^{2+} for an hour before being analysed using TRPS. The aptamer modified particles were incubated in a range of ionic strengths. The particle velocities were recorded for each ion strength and compared to the aptamer modified particles, shown in Figure 6.10. The addition of Hg^{2+} ion decreases the particles velocity. The change in velocity is attributed to the changes of the DNA structure when the Hg^{2+} ions bind. The ionic strengths chosen were the same used in the Pb^{2+} experiments and designed to mimic real life samples containing Na^+.

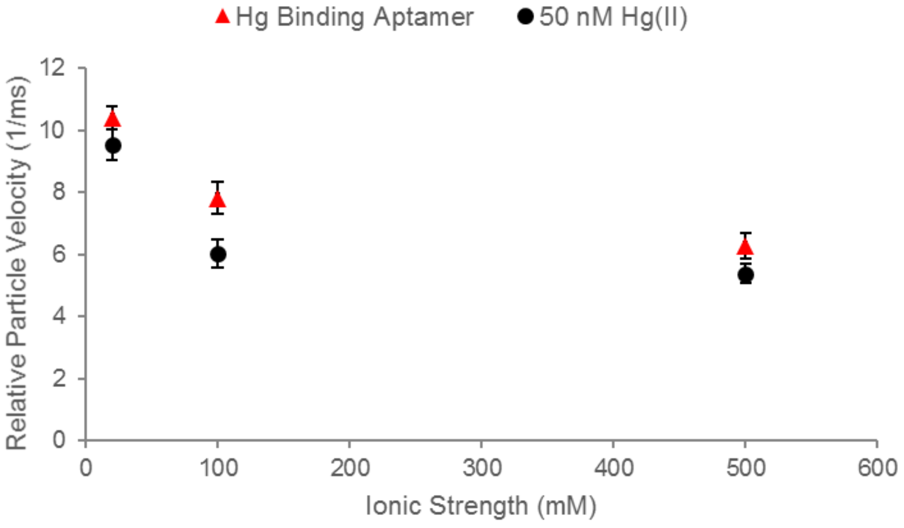

Figure 6.10 Particles modified with the mercury binding aptamer (red triangles) and incubated with 50 nM Hg^{2+} for 1 hour (black circles). Samples were analysed using an NP200 pore, pH ~6, stretch 45.50 mm. Error bars represent the standard deviation of three experiments.

The aptamer modified particles were incubated with range of Hg^{2+} concentrations and were analysed across the electrolyte concentrations and their velocities are shown in Figure 6.11. In each electrolyte concentration, particles incubated with 20 nM Hg^{2+} showed a significant decrease in velocity from the blank.

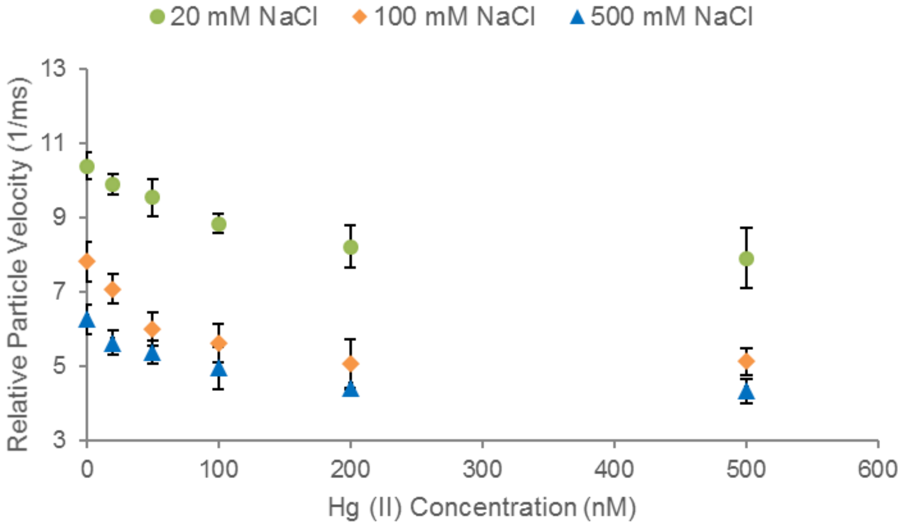

Figure 6.11 Aptamer modified particles incuabted in a range of Hg^{2+} cocentrations and analysed in three different NaCl concentrations, 20 mM NaCl (green circles), 100 mM NaCl (orange diamonds) and 500 mM NaCl (blue triangles). Samples were analysed using an NP200 pore, pH ~6, stretch 45.50 mm. Error bars represent the standard deviation of three experiments.

The dynamic range for Hg^{2+} is higher than Pb^{2+}. Each strand of the TBAA aptamer can bind a single Pb^{2+} ion, the mercury binding aptamer can bind up to seven Hg^{2+} ions. More mercury ions are needed to see a difference in particle velocity, suggesting that for the DNA aptamer to form a hairpin structure more than one Hg^{2+} ion is needed for each aptamer strand.

To demonstrate the selectivity of the mercury binding to aptamer, a control experiment was carried out with another metal ion. The mercury binding aptamer modified particles were incubated with Cu^{2+} (1 µM) for one hour and the velocities recorded. Figure 6.12 shows there is no significant decrease in velocity when incubated with the copper ions. The Cu^{2+} ions do not bind to the thymine bases on the aptamer and therefore do not change the particles velocity.

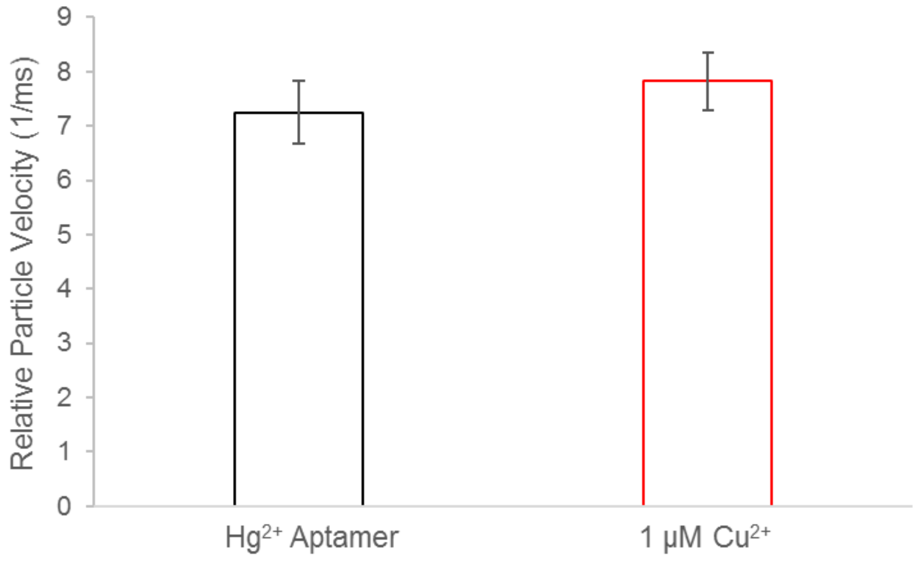

Figure 6.12 Mercury binding aptamer modified particles incubated with 1 µM Cu^{2+} measured in 100 mM NaCl. Samples were analysed using an NP200 pore, pH ~6, stretch 45.50 mm. Error bars represent the standard deviation of three experiments.

6.4.3 Multiplexed Detection of Lead and Mercury

The benefit of Particle-by-Particle analysis carried out using TRPS allows for different particle sizes in one sample to be detected. This is beneficial over other particle characterisation techniques such as DLS. Two or more analytes can easily be detected by using two different sized particles with different aptamers on the particles. The Pb^{2+} binding aptamer (TBAA) was immobilised on 300 nm particles and the Hg^{2+} binding aptamer was immobilised on 150 nm particles.

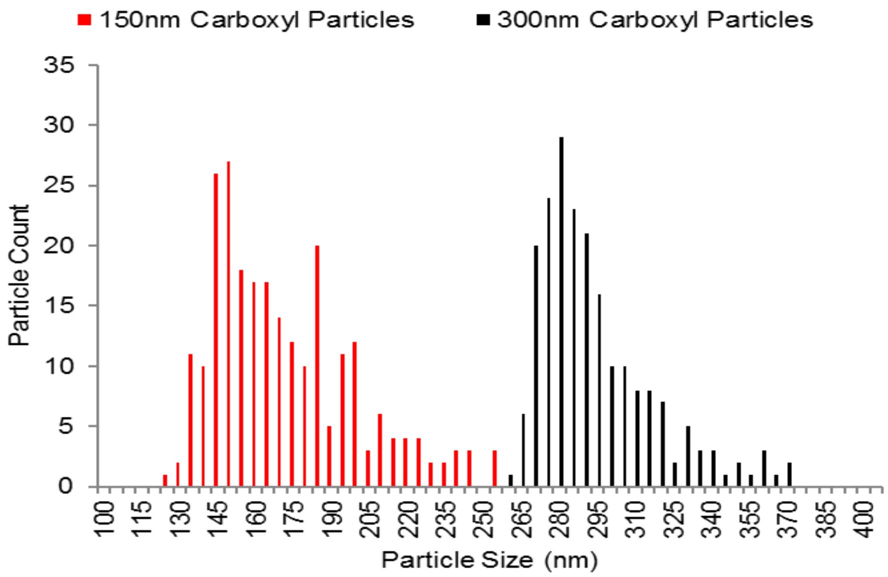

Figure 6.13 Particle size distribitions of two different particle sets. 150 nm carboxyl particles (red) and 300 nm carboxyl particles (black) run seperately on a NP200 pore.

The particles used can be distinguished based on their size, Figure 6.13 displays the calibrated diameter distributions for the two different particles measured separately. The two particle sizes can be distinguished without overlap. The velocities of the particles can be extracted for each individual particle, therefore can easily be distinguished based on their size.

To demonstrate the ability to multiplex the detection of Pb^{2+} and Hg^{2+} a control experiment was conducted to show no interference from the additional metal ion in solution. The velocities were recorded for 150 nm particles modified with Hg^{2+} binding aptamer which had been incubated with 20 nM Pb^{2+}, Figure 6.14. The velocities were also recorded for 300 nm particles modified with TBAA which were incubated with 20 nM Hg^{2+}, Figure 6.14. The velocities of the aptamer modified particles did not significantly change, which illustrates that the binding of the aptamer is specific to the chosen metal ion.

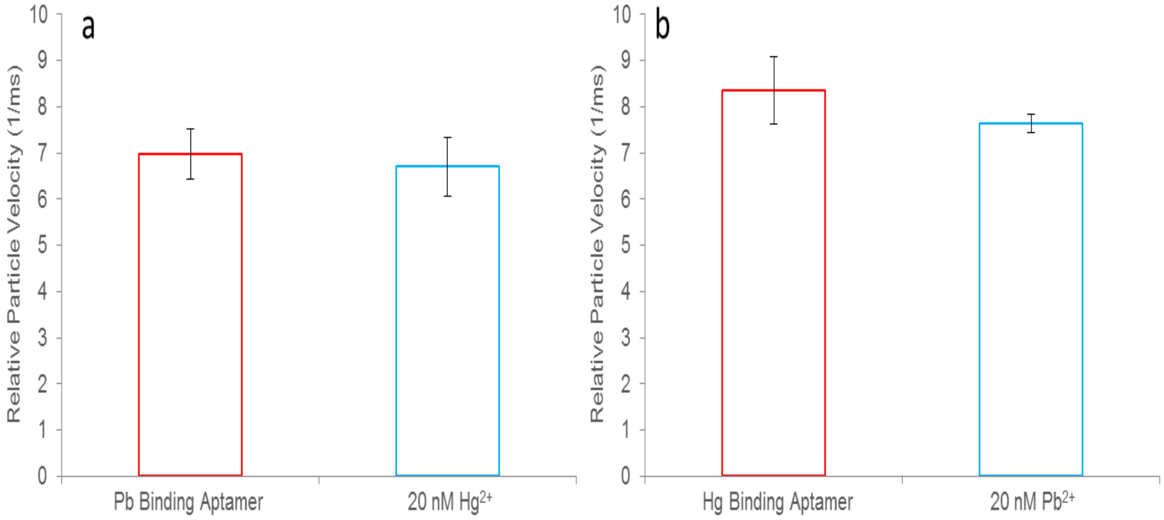

Figure 6.14 a) Particles modified with the lead binding aptamer (TBAA) incubated with 20 nM Hg^{2+} for 1 hour. b)Particle modified with the mercury binding aptamer incubated with 20 nM Pb^{2+} for 1 hour. Samples were analysed using an NP200 pore, in 100 mM NaCl, pH ~6, stretch 45.50 mm. Error bars represent the standard deviation of three experiments.

The velocities of the two different sized particles were measured simultaneously in the presence of 20 nM Pb^{2+} and Hg^{2+}, Figure 6.15a. The velocity of each individual particle is recorded as the particles traverse the pore. This allows particle sizes to be easily distinguished and thus each analyte to be easily distinguished when binding to the particle. As a comparison the velocities of both particle sizes were measured separately and then simultaneously in the same solution. The velocities measured simultaneously show little variation compared to when each particle size was measured separately, Figure 6.15b.

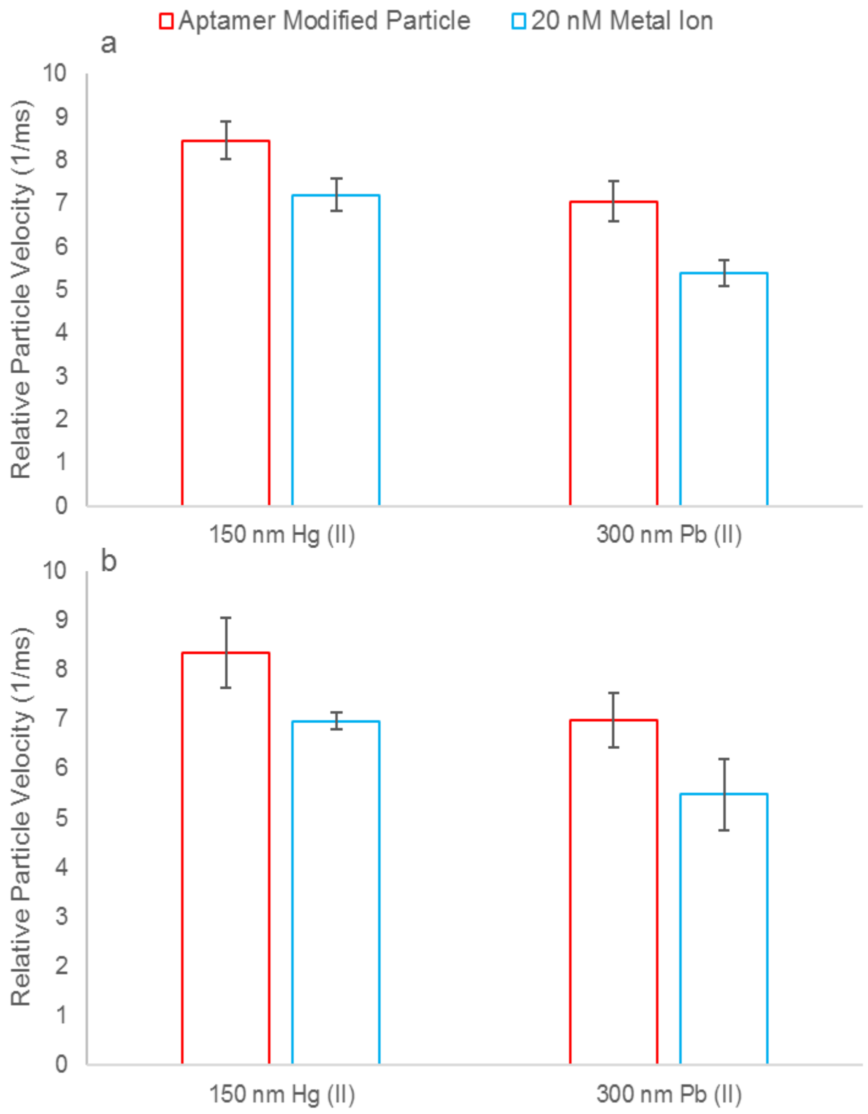

Figure 6.15 a) 150 nm particles modified with mercury binding aptamer and 300 nm particle modified with lead binding aptamer (TBAA) were incubated in a solution containing 20 nM Pb^{2+} and 20 nM Hg^{2+} for 1 hour. b) 150 nm particles modified with mercury binding aptamer were incubated with 20 nM Hg^{2+} for 1 hour and 300 nm particles modified with lead binding aptamer (TBAA) were incubated with 20 nM Pb^{2+} for 1 hour seperately. Samples were analysed using an NP200 pore, in 100 mM NaCl, pH ~6, stretch 45.50 mm. Error bars represent the standard deviation of three experiments.

Using two different sized particles allows for simultaneous detection of two or more analytes. The method can be adapted for analysis of more analytes by using a greater number of particle sizes. For more particles to be analysed on one pore, the size distributions for each particle set need to be smaller.

Simultaneous detection of lead and mercury has been reported previously using aptamer modified particles.[16] However, the method used requires a lengthy process for the modification of the gold nanoparticles with the DNA aptamers, unlike the simple modification method presented here. Both methods offer similar detection times, incubating the particles with the metal ion for one hour. This is something that could be explored further with the potential to lower the incubation times as shown in Chapter 4 when detecting Cu^{2+} after 5 minutes.

6.5 Conclusions

In summary, the work in this chapter further develops the work presented in Chapter 4. Particle velocities were recorded for aptamer modified particles in the presence of toxic heavy metal ions, lead and mercury. The selectivity and specificity of the DNA aptamers ensures the signal measured is due to the metal ion binding to the aptamer. The method was shown to be responsive over a large range of ionic strengths with little interference from a high salt content.

A benefit of TRPS is particle-by-particle analysis and particles of different sizes are easily distinguished. To detect both metals simultaneously two different particle sizes were used. The mercury aptamer was grafted to 150 nm particles, while the lead aptamer was grafted to 300 nm particles. Monitoring the velocity of the particles and distinguishing the particle based on size enabled the simultaneous detection of mercury and lead with little variation from when the analytes were detected individually. This creates a sensor for the simultaneous detection mercury and lead ions with nM sensitivity that is capable of being run in a range of electrolyte concentrations, equivalent to river to seawater conditions.

Multiplexed detection of analytes is beneficial, however a typical RPS device will have an upper limit to the number of particles that can be run simultaneously. This is dependent upon the pore size and ability to produce uniform beads within the pores sensing range. Further work would need to be carried out to determine the number of different particles TRPS could distinguish between. Changing the shape of the particles is another avenue that could be explored when designing a multiplexed sensor.

6.6 References

1. Zhou, W., Saran, R. & Liu, J. Metal Sensing by DNA. *Chem. Rev.* acs. **117**, 8272−8325 (2017).

2. Ono, A. & Togashi, H. Highly selective oligonucleotide-based sensor for mercury(II) in aqueous solutions. *Angew. Chemie - Int. Ed.* **43,** 4300–4302 (2004).

3. Li, M., Zhou, X., Ding, W., Guo, S. & Wu, N. Fluorescent aptamer-functionalized graphene oxide biosensor for label-free detection of mercury(II). *Biosens. Bioelectron.* **41,** 889–893 (2013).

4. Smirnov, I. V., Kotch, F. W., Pickering, I. J., Davis, J. T. & Shafer, R. H. Pb EXAFS studies on DNA quadruplexes: Identification of metal ion binding site. *Biochemistry* **41,** 12133–12139 (2002).

5. Yang, D. *et al.* Aptamer-based biosensors for detection of lead(II) ion: a review. *Anal. Methods* **9,** 1976–1990 (2017).

6. Hai, H., Yang, F. & Li, J. Highly sensitive electrochemiluminescence 'turn-on' aptamer sensor for lead(II) ion based on the formation of a G-quadruplex on a graphene and gold nanoparticles modified electrode. *Microchim. Acta* **181,** 893–901 (2014).

7. Liu, J. *et al.* A catalytic beacon sensor for uranium with parts-per-trillion sensitivity and millionfold selectivity. *Proc. Natl. Acad. Sci. U. S. A.* **104,** 2056–61 (2007).

8. Liu, J. & Lu, Y. A DNAzyme Catalytic Beacon Sensor for Paramagnetic Cu^{2+} Ions in Aqueous Solution with High Sensitivity and Selectivity. *J. Am. Chem. Soc.* **129,** 9838–9839 (2007).

9. Sekhon, S. S. *et al.* Defining the copper binding aptamotif and aptamer integrated recovery platform (AIRP). *Nanoscale* **9,** 2883–2894 (2017).

10. Huang, Y. *et al.* Highly sensitive and selective optical detection of lead(II) using a label-free fluorescent aptasensor. *Rsc Adv.* **6,** 90300–90304 (2016).

11. Kumar, P., Kumar, V. & Gupta, R. Selective fluorescent turn-off sensing of Pd $^{2+}$ ion: applications as paper strips, polystyrene films, and in cell imaging. *RSC Adv.* **7,** 7734–7741 (2017).

12. Li, J. & Lu, Y. A Highly Sensitive and Selective Catalytic DNA Biosensor for Lead Ions. *J. Am. Chem. Soc.* **122,** 10466–10467 (2000).

13. Li, T., Dong, S. & Wang, E. A lead(II)-driven DNA molecular device for turn-on fluorescence detection of lead(II) ion with high selectivity and sensitivity. *J. Am. Chem. Soc.* **132,** 13156–13157 (2010).

14. Li, L., Li, B., Qi, Y. & Jin, Y. Label-free aptamer-based colorimetric detection of mercury ions in aqueous media using unmodified gold nanoparticles as colorimetric probe. *Anal. Bioanal. Chem.* **393,** 2051–2057 (2009).

15. Zhang, S. *et al.* Ultratrace Naked-eye Colorimetric Detection of Hg^{2+} in Wastewater and Serum Utilizing Mercury-stimulated Peroxidase Mimetic Activity of Reduced Graphene Oxide-PEI-Pd Nanohybrids. *Anal. Chem.* **89**, 3538–3544 (2017).

16. Li, Y. *et al.* Fully integrated graphene electronic biosensor for label-free detection of lead (II) ion based on G-quadruplex structure-switching. *Biosens. Bioelectron.* **89,** 758–763 (2017).

17. Chiu, T. C. & Huang, C. C. Aptamer-functionalized nano-biosensors. *Sensors* **9,** 10356-10388 (2009).

18. Samanta, A. & Medintz, I. L. Nanoparticles and DNA – a powerful and growing functional combination in bionanotechnology. *Nanoscale* **8,** 9037–9095 (2016).

19. Kotch, F. W., Fettinger, J. C. & Davis, J. T. A lead-filled G-quadruplex: insight into the G-Quartet's selectivity for Pb^{2+} over K^{+}. *Org Lett* **2,** 3277–3280 (2000).

20. Chung, C. H., Kim, J. H., Jung, J. & Chung, B. H. Nuclease-resistant DNA aptamer on gold nanoparticles for the simultaneous detection of Pb^{2+} and Hg^{2+} in human serum. *Biosens. Bioelectron.* **41,** 827–832 (2013).

21. Yu, Z. *et al.* Na+-Induced Conformational Change of Pb^{2+}-Stabilized G-Quadruplex and Its Influence on Pb^{2+} Detection. *Anal. Chem.* **88,** 9375–9380 (2016).

22. Sen, D. & Gilbert, W. A sodium-potassium switch in the formation of four-stranded G4-DNA. *Nature* **344,** 410–4 (1990).

23. Jing, N., Rando, R. F., Pommier, Y. & Hogan, M. E. Ion selective Folding of loop domains in a potent anti-HIV oligonucleotide. *Biochemistry* **36,** 12498–12505 (1997).

24. Marathias, V. M. & Bolton, P. H. Determinants of DNA quadruplex structural type: Sequence and potassium binding. *Biochemistry* **38,** 4355–4364 (1999).

25. Miyake, Y. *et al.* Mercury(II)-mediated formation of thymine-Hg(II)-thymine base pairs in DNA duplexes. *J. Am. Chem. Soc.* **128,** 2172–2173 (2006).

26. Torigoe, H., Ono, A. & Kozasa, T. Hg(II) ion specifically binds with T:T mismatched base pair in duplex DNA. *Chem. - A Eur. J.* **16,** 13218–13225 (2010).

7 Comparison of a particle and pore assay using modified aptamers to simultaneously detect metal ions.

Work presented in this chapter is a continuation of the work presented in Chapter 6. The ability to quickly detect and quantify metal ions in solution is attractive and has many applications within environmental and health sciences. But a typical RPS device will have an upper limit to the number of particles that can be run simultaneously. This is dependent upon the pore size and ability to produce uniform beads within the pores sensing range. One way to increase the number of analytes for detection may be to create dual responsive beads, that is, one bead whose velocity changes in the presence of two different analytes. To advance this multiplexed concept, the two independent aptamer sequences used in Chapter 6 are merged together. While both aptamer halves retain their initial functionality and bind to the respective metals, the location of the binding and change in DNA structure with respect to the particles surface is the dominating factor in determining the sensitivity of the RPS technology. Two assays are developed, one using nanoparticles and the other using a modified pore wall. Each assay is developed further from previous chapters and can be used for the design of sensors to simultaneously detect lead and mercury.

7.1 Aims and Objectives

To develop the multiplex assay further, the work presented in this chapter aims to create an aptamer which has binding sites for two different metal ions. The dual aptamer will allow particles to be modified with a dual responsive aptamer which will alter the particles velocity through the pore when in the presence of mercury and lead. Chapter 5 demonstrates the sensitivity of a pore-based assay and the same principle will be used here to detect each metal ion simultaneously, using a single aptamer.

7.2 Introduction

DNA has many desirable properties for metal ion sensing and the use of nucleotides as metal ligands has been extensively studied.[1–5] DNA is a polyanion, which allows for electrostatic attraction with metal ions. DNA phosphates can bind to hard metals, while the bases coordinate with metal ions with varying affinities.[1–5] Through DNA folding, 3D binding pockets can form to accommodate specific metal coordination preferences which are often difficult to achieve via rational ligand design. The versatile binding gives DNA the potential for selective and specific metal binding. DNA is highly stable with chemical synthesis of DNA at low cost. The synthesis methods offer a diverse range of modifications too. Finally, DNA is amenable to *in vitro* selection, allowing combinational searches for metal binding sequences. These selections can be carried out in most laboratories with common equipment.

Extensive progress has been made in developing DNA-based metal ligands and related analytical applications in the past two decades. Such functional DNAs are important for both fundamental research and practical applications. However, there is still a need to improve the sensitivity of DNA based metal ion detection assays. One intrinsic problem of DNA is its relatively low metal binding affinity in the low μM to low mM range. Efforts are focusing on by introducing modified nucleotides with functional groups to improve sensitivity.[6]

Environmental samples, unlike biological samples, have no concentrated proteins in solution, therefore detection using DNA aptamers is less complicated. However, often in environmental samples, more than one toxic heavy metal is present. Detection of multiple metals simultaneously is favourable and is the focus on the work presented in this chapter. Two DNA aptamers, which were used in chapter 7 to detect Pb^{2+} and Hg^{2+}, were combined to create a DNA aptamer with the binding sites for both metal ions. It is hypothesised that the ability to multiplex can be increased by having a dual response surface. Here, a comparison of a nanoparticle based assay and a pore wall based assay is presented. Both assays give an insight into how DNA based sensors can be used in TRPS and shows the limitations of using a nanoparticle based assay.

7.3 Experimental

7.3.1 Method and Materials

The following chemicals were purchased from Sigma Aldrich, UK, poly(ethyleneimine), PEI, (Mw 750 000 g mol^{-1}, analytical standard, 50 % wt., P3143), poly(acrylic acid-co-maleic acid) (PAAMA, Mw ~3000 g mol^{-1} 50 % wt., 416053), copper (II) chloride dihydrate ($CuCl_2.2H_2O$, reagent grade, 221783), lead(II) nitrate ($Pb(NO_3)_2$, ACS reagent, ≥99.0%, L7281), mercury (II) chloride ($HgCl_2$, ACS reagent, ≥99.5%, M6529), sodium hydroxide (NaOH, reagent grade, ≥98%, S5881), (2-(N-Morpholino)ethanesulfonic acid hydrate (MES hydrate, ≥99.5 %, M2933) and *N*-hydroxysulfosuccinimide sodium salt (NHS, ≥98.5 %, 56485).. Tunable conical pores (NP200s) and carboxylated polystyrene particles (210 nm in diameter, denoted CPC200) were purchased from Izon Science, Christchurch, NZ. The following chemicals were purchased from Fisher Scientific, UK, potassium chloride (KCl, >99 %, P/4240/60), sodium chloride (NaCl, analytical grade, S/3160/60) and potassium hydroxide (KOH, 0.1 M, >85 %, P/5600/60).Hydrochloric acid (HCl, 0.5 M, 37 %) was purchased from VWR, UK.1-ethyl-3-(3-dimethylaminopropyl)carbodiimide hydrochloride (EDC, 22980) was purchased from Thermo Scientific, UK.

Reagents were prepared in deionised water with a resistivity of 18.2 MΩ cm (Maxima). pH of solutions were altered using HCl and KOH. The solutions were measured using a Mettler Toledo easy five pH meter with a Mettler Toledo InLab micro electrode.

7.3.2 Custom DNA Oligonucleotides

The oligonucleotides used in this study were purchased as lyophilised powders from Sigma Aldrich, UK. The sequences were synthesised with an amine functional group at the 3’ end, the sequences are shown in Table 7.1.

.

Table 7.1 Custom Oligonucleotides used in this chapter. Mercury aptamer (italics), Lead aptamer (underlined)and loop length (bold).

Aptamer	Sequence
Lead and mercury binding aptamer[7,8]	5'-*TTCTTTCTTCG*GGAAGGTGTGGAAGG*CGTTGTTTGTT*-3'
Loop 4	5'-*TTCTTTCTT***GAGG***TTGTTTGTT*-3'
Loop 8	5'-*TTCTTTCTTCG***GAGGGGAA***CGTTGTTTGTT*-3'
Loop 11	5'-*TTCTTTCTTCG***GGAAGTGGAAG**CG*TTGTTTGTT*-3'

7.3.3 Particles

Superparamagnetic particles were purchased from Ademtech, France (150 nm in diameter, 0211). The particles were modified using PEI and PAAMA to ensure a carboxyl group was present on the particles. Particles were taken from stock (50 µL) and suspended in PEI (1 mL, 5% in H_2O). The solution was placed on the rotary wheel for 30 minutes. The solution was vortexed for 5 minutes at 10 000 rpm, the PEI solution removed from the particles and replaced with water. The sample was vortexed and sonicated until the particles were fully dispersed. This wash step was repeated twice to ensure all excess PEI had been removed. The PEI coated particles were suspended in PAAMA (5% in 50 mM NaCl) for 30 minutes and placed on the rotary wheel. The same process for removing the excess PEI was used. The particles were then stored at 2 – 4ºC in water. Carboxyl polystyrene particles (303 nm in diameter,11839) were purchased from Bangs Laboratories, US and used without any modification.

Each aptamer was dissolved in 100 mM MES buffer (pH 5.7) containing 1 mg ml^{-1} EDC and 1 x 10^{10} carboxylated particles/ mL. The final concentration of DNA was 410 nM. The solution containing the particles was placed on the rotary wheel for 1 hour. To remove an excess DNA, the solutions containing the magnetic 150 nm particles were placed in a MagRack (Life Sciences). After 5 minutes, the particles had formed a visible cluster and the solution was removed and replaced with an equal volume of NaCl (20 – 500 mM). Metal Ion Extraction

A lead (II) solution (1 µM) was prepared from $Pb(NO_3)_2$ in a range of ionic strengths (20 – 500 mM NaCl). The solution was further diluted in the same ionic strength to give a range of lead concentrations (0.05 – 100 nM). A 0.1 nM Lead (II) solution was prepared in KCl (500 mM). A mercury (II) solution (1000 nM) was prepared from $HgCl_2$ in a range of ionic strengths (20 – 500 mM NaCl). The solution was further diluted in the same ionic strength to give a range of mercury concentrations (20 – 500 nM).

Aptamer modified particles (1×10^9 particles mL^{-1}) were added to the solutions of desired metal ion concentration and ionic strength. The solutions were vortexed for 30 s and placed on the rotary wheel for 1 hour.

7.3.4 Pore Modification

The nanopores were modified by incubating the pore in the PEI solution (5 % wt in H_2O) at a stretch of 45 mm for two hours. The pore was rinsed with deionised water and then incubated with the PAAMA solution (5% wt in H_2O) for two hours. The pores were rinsed with deionised water and *I-V* curves recorded between each incubation.

The pores modified with PAAMA were modified with a DNA aptamer. The aptamer was dissolved in 100 mM MES buffer containing 1 mg mL^{-1} EDC. The pore was incubated with the DNA solution for 1 hour at a 45 mm stretch.

7.3.5 TRPS Set-Up

All measurements were conducted using the qNano (Izon Science, NZ) combing tunable nanopores with data capture and analysis software, Izon Control Suite v.3.1. The lower fluid cell contains the electrolyte (75 µL). The particle is suspended in the same electrolyte and placed in the upper fluid cell (40 µL). Prior to analysis all samples were vortexed and sonicated for 30 s. After each sample run, the system was washed by placing 40 µL of electrolyte into the upper fluid cell several times with various pressures applied to ensure there were no residual particles remaining and therefore no cross contamination between samples.

7.3.6 Particle Translocation Velocity

The same method for calculating the relative particle translocation velocity through the pore was presented previously in Chapters 3 and 4. Briefly. the method uses the resistive pulse to calculate the relative velocity. For each blockade, the time at which the peak occurs is defined as $T_{1.0}$ (time at 100% of peak magnitude) and the maximum magnitude of the pulse (relative to the local baseline resistance) is recorded as dRmax. The duration from $T_{1.0}$ to each section is defined at $T_{0.60}$, $T_{0.50}$, $T_{0.40}$ and $T_{0.30}$. When the proportional blockade magnitude is equal for any given particles (small or large), these particles are at the same position within the pore. Hence, the relative magnitude is an indicator of the particle position within the pore.

7.3.7 Pore Modification

The nanopores were modified by incubating the pore in the PEI solution (5 % wt in H_2O) at a stretch of 45 mm for two hours. The pore was rinsed with deionised water and then incubated with the PAAMA solution (5% wt in H_2O) for two hours. The pores were rinsed with deionised water and *I-V* curves recorded between each incubation.

The pores modified with PAAMA were modified with a DNA aptamer. The aptamer was dissolved in 100 mM MES buffer containing 1 mg mL^{-1} EDC. The pore was incubated with the DNA solution for 1 hour at a 45 mm stretch.

7.3.8 Metal Ion *I-V* Assay

The metal ions, Hg^{2+} and Pb^{2+}, were prepared in 500 mM NaCl to give the desired concentration. in each experiment, the solution containing the metal ion was only placed on the side of the pore with the small pore opening. When multiple solutions of different concentrations of the metal ions were used the lowest concentration was measured first. The metal ion solution was in contact with the pore for 30 minutes with the pore being rinsed with water x 3, and NaCl (20 mM) x 3 after each incubation step. The current rectification property of the pore was then measured, in a range of NaCl solutions starting with 20 mM first and working up to 500 mM.

7.3.9 *I-V* Measurements

The pores were mounted between two fluid cells which contain an electrolyte solution. Current-voltage (*I-V*) curves were recorded using Izon control suite v3.2, the potential was stepped in 100 mV increments from +1.6 to -1.6 V and the resulting current measured.

7.3.10 Statistical Analyses

All statistical analyses were performed using IBM SPSS Statistics (v 22.0, IBM Corp., Armonk, NY, USA). To assess the change in particle velocity through the pore, a t-test assuming equal variance was carried out. A p value of < 0.05 was considered statistically significant.

7.4 Results and Discussion

The mercury binding aptamer and lead binding aptamer, used in chapter 6 demonstrates the high sensitivity and selectivity that DNA aptamers exhibit towards metal ions. The Hg^{2+} and Pb^{2+} ions bind to different bases on the DNA sequence, the Hg^{2+} binds to thymine bases causes at T-T mistmatch and the Pb^{2+} will bind to a guanine rich DNA strand by for a G-quadruplex structure, Figure 7.1Aii. By exploiting the binding characteristics of DNA, a single stranded DNA aptamer was developed to bind both analytes. The sequence is as follows, 5'-*TTCTTTCTTCG*GGAAGGTGTGGAAGG*CGTTGTTTGTT*-3'. The Pb^{2+} aptamer section is underlined, while the Hg^{2+} aptamer is in italics.[7,8]

We hypothesised that combining the aptamers for lead and mercury would enable us to detect both metal ions simultaneously using a single DNA sequence. The DNA sequence was checked in mFold that combining the aptamers does not introduce other tertiary structures that could prevent binding. Chapter 6 shows how using the two aptamers enables us to detect mercury and lead using two different particle sizes. Using a single DNA strand eliminates the need for multiple particle sizes and we hypothesis that two different signals can be generated from a single aptamer with binding sites for two different metals.

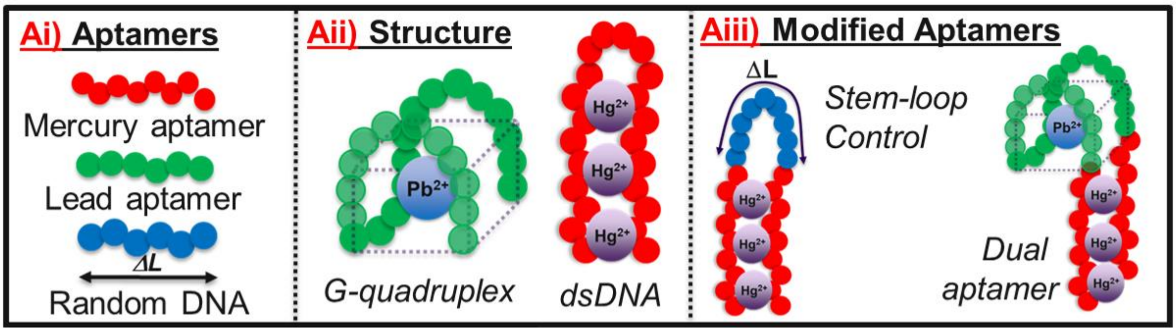

Figure 7.1 Ai) Aptamer sequences used when detecting Hg^{2+} and Pb^{2+}. Aii) Structure of DNA aptamers upon binding with the metal ion. Aiii) Modified aptamer structures combining the Pb^{2+} and Hg^{2+} binding aptamers.

Figure 7.1 shows the structures of each aptamer when binding to the metal ions. The modified aptamer investigates the differences seen in nanoparticle and pore wall assays and offers insight into the design of DNA sensors using nanopores.

Carboxyl nanoparticles particles were modified with the aptamer and the velocity measured in 100 mM NaCl. The velocity of the DNA modified particles was greater than particles modified with either the Pb^{2+} or Hg^{2+} binding aptamer, Figure 7.2. This is to be expected due to the longer length of the DNA which has been shown previously to increase particle mobility. [9]

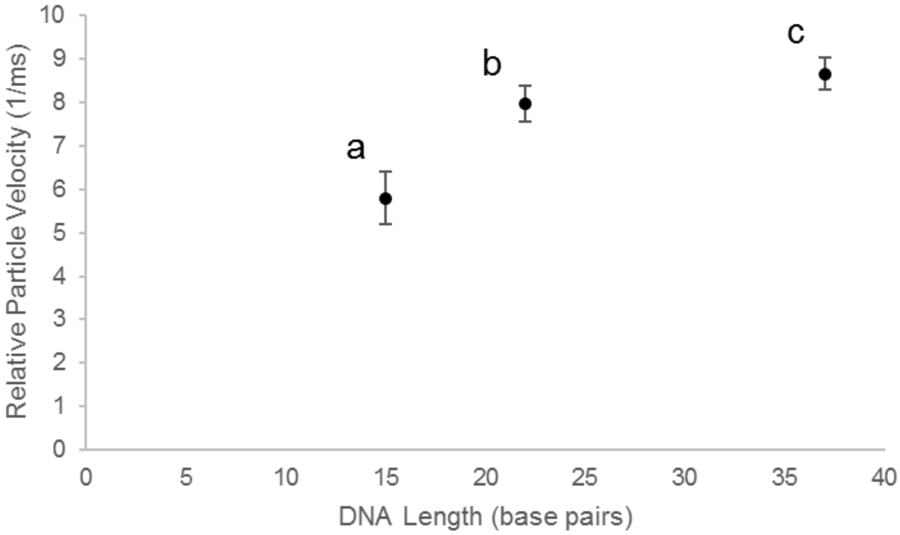

Figure 7.2 Carboxyl particles modified with varying lengths of DNA. a) Lead binding aptamer, b) mercury binding aptamer and c) dual modified aptamer. Samples were analysed using an NP200 pore, pH ~6, stretch 45.50 mm, 100 mM NaCl. Error bars represent the standard deviation of three experiments.

The modified particles were incubated with a solution of 20 nM Pb^{2+} for an hour and the resulting particle velocity measured. The same experiment was carried out on a different aliquot of particles using 20 nM Hg^{2+}. The particle velocities were recorded before and after the metal binding. The particles incubated with Pb^{2+} decreased in velocity, Figure 7.3, however the particles incubated with Hg^{2+} showed no difference in velocity compared with the particles with no metal ion, Figure 7.3. The particles were incubated with a larger concentration of Hg^{2+} ions (200 nM) and the velocities measured again. There were still no observed changes in the particle's velocity, Figure 7.3.

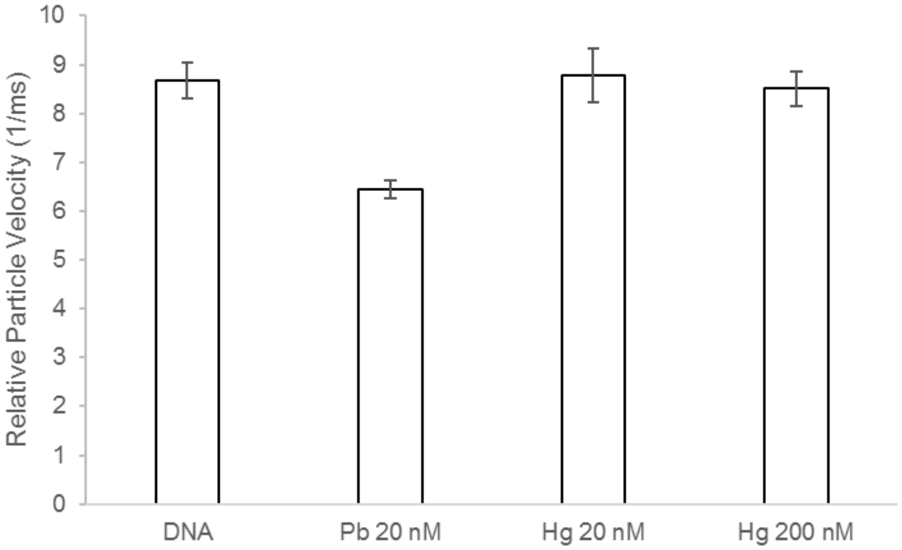

Figure 7.3 Changes in particle translocation velocity when incubated with lead or mercury. Samples were analysed using an NP200 pore, pH ~6, stretch 45.50 mm, 100 mM NaCl. Error bars represent the standard deviation of three experiments. Mean velocity Pb 20 nM significantly differs from the velocity of DNA (t-test, p=<0.001). No sigificant difference between DNA and mercury recorded (t-test, p=0.61).

The aptamer has binding sites for both the Pb^{2+} and Hg^{2+} ions, the aptamer modified particles were incubated with both metal ions. Firstly, the particles were incubated with 20 nM Pb^{2+} ions followed by 20 nM Hg^{2+} ions. The particle velocities were measured between each metal ion incubation step. As expected from the previous experiment, the velocities of the particles incubated with Pb^{2+} were reduced however after the particles incubation with Hg^{2+}, no change in particle velocity was measured, Figure 7.4.

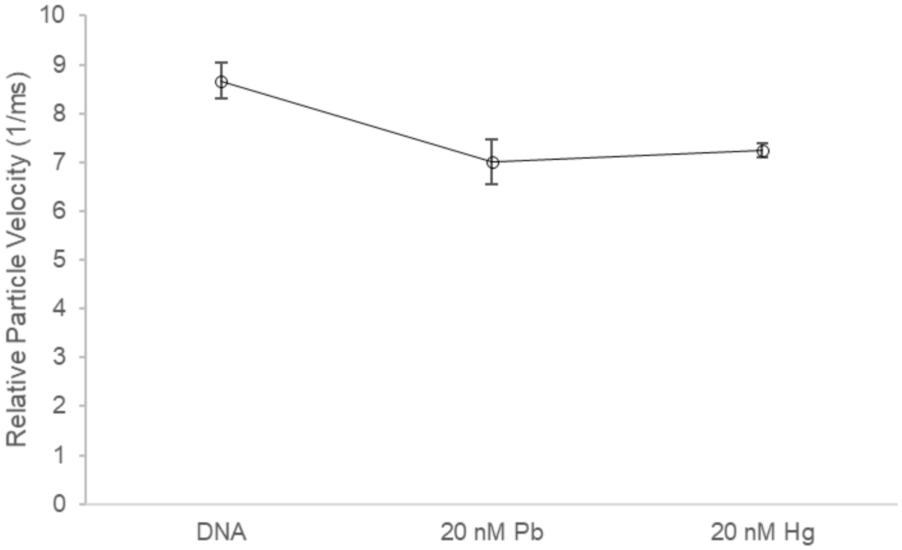

Figure 7.4 Aptamer modified particles incubated with 20 nM Pb followed by 20 nM Hg. Samples were analysed using an NP200 pore, pH ~6, stretch 45.50 mm, 100 mM NaCl. Error bars represent the standard deviation of three experiments. Mean velocity Pb 20 nM significantly differs from the velocity of DNA (t-test, p=<0.001). No sigificant difference between lead and mercury recorded (t-test, p=0.55).

The same experiment was performed with the first incubation with 20 nM Hg^{2+} followed by 20 nM Pb^{2+}. No change in particle velocity was recorded after the first incubation with Hg^{2+}. The particle velocity decreased after the incubation with Pb^{2+}, Figure 7.5. Observing a change in particle velocity suggests that the mercury ions were either not binding to the aptamer or that the change in aptamer design has inhibited the ability for TRPS to detect changes on the particle surface via particle translocation.

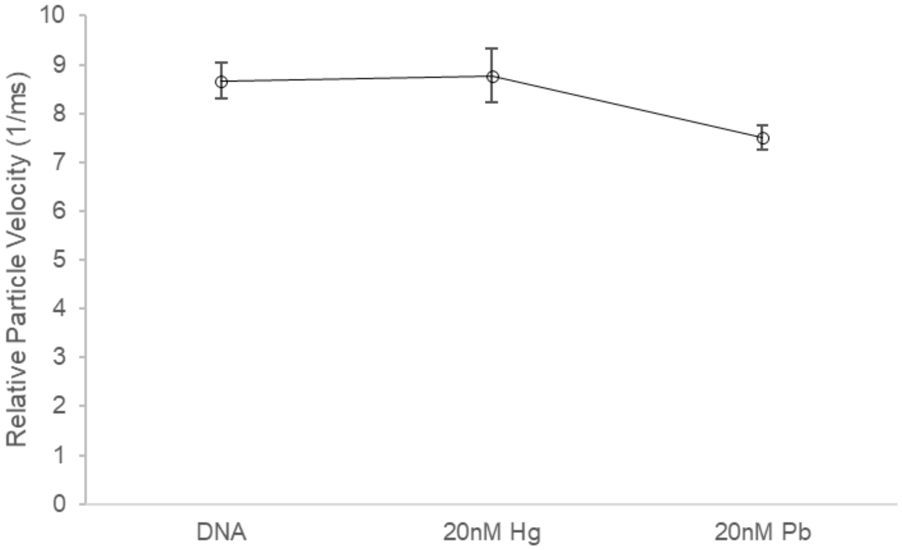

Figure 7.5 Aptamer modified particles incubated with 20 nM Hg followed by 20 nM Pb. Samples were analysed using an NP200 pore, pH ~6, stretch 45.50 mm, 100 mM NaCl. Error bars represent the standard deviation of three experiments. No sigificant difference between DNA and mercury recorded (t-test, p=0.89).

The T-Hg^{2+}-T structure is more stable than a Watson-Crick A-T bond.[7,10] Therefore, it was hypothesised that the Hg^{2+} ions were bound to the DNA aptamer, however due to the structure of the DNA aptamer, TRPS was unable to detect the differences between the aptamer modified particles with and without Hg^{2+} bound. It was hypothesised that no changes in particle velocity are detected due to the Hg^{2+} ions being held close to the particles surface in the hairpin while being shielding by a large DNA loop. To test this, the effect of the loop length was looked at.

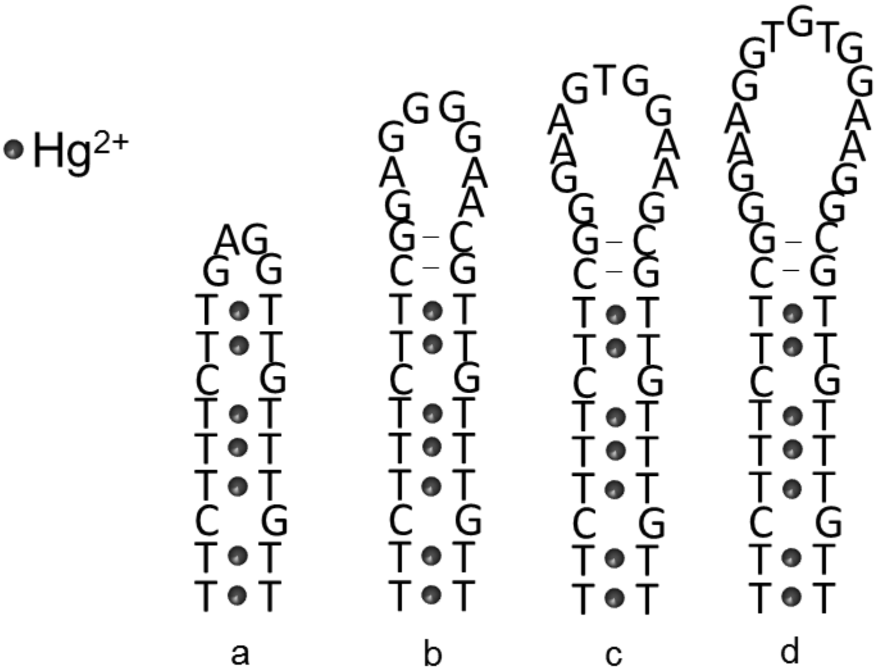

Figure 7.6 DNA sequences with varying loop length, a) loop 4, b) loop 8, c) loop 11 and d) loop 15.

Three more DNA aptamers were used with varying loop lengths. The beads were modified with each aptamer of varying loop length and the particles were incubated with 200 nM Hg^{2+} and the resulting velocities recorded. The DNA loop is increased from four bases up to fifteen bases (dual aptamer). The velocities of the shorter DNA loops, four and eight bases, decreased when incubated with Hg^{2+} ions, Figure 7.7. At eleven bases the velocity changes are negligible and at fifteen bases there is no significant differences in the particles velocities. At these loop lengths, the charge of the DNA loop shields the Hg^{2+} binding which is held close to the particles surface and therefore no significant decrease in velocity is recorded. Increasing the loop length results in a diminishing response and change between the blank and assay signal, that is, as the outer layer of DNA becomes longer, the change in signal decreases.

This observation may indicate there is a limit to what aptamer structure and length can be observed in RPS sensors.

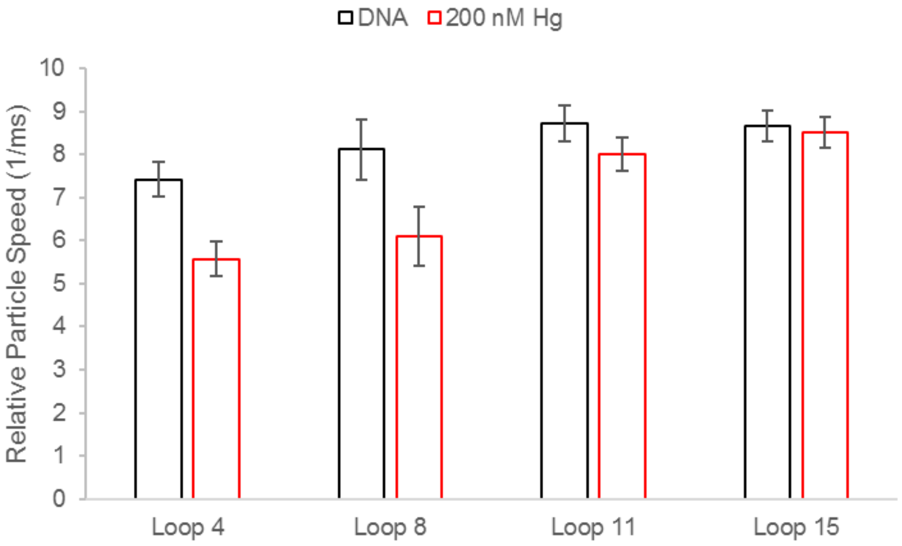

Figure 7.7 Varying loop length of DNA measured with and without Hg. Samples were analysed using an NP200 pore, pH ~6, stretch 45.50 mm, 100 mM NaCl. Error bars represent the standard deviation of three experiments.

We assume there is no change in binding affinities of the aptamer towards each metal when combined, previous work has shown that adding G-quadruplex structures to the end of stem regions have been shown to enhance their binding to proteins. Further work would need to be carried out to obtain the binding affinities towards the dual aptamer.[11] We conclude that a dual aptamer approach here will not work using a nanoparticle assay. This insight may help other nanoparticle-based assays using TRPS in the future.

7.4.1 Ion Current Rectification

Previous work in chapter 5 has shown that modifying the nanopores with the DNA aptamers has enabled the detection of proteins by studying the rectification of the nanopore.[12] The layer by layer method (LbL) for modifying the conical pores used in this work allows for facile modification of the pore to introduce the carboxyl groups needed for the DNA modification.

Modifying the pore with different polymers shows how the rectification of the pore changes. Figure 7.8, illustrates the change in rectification as the pore wall charge changes. The unmodified pore shows ohmic behaviour, when the pore is modified with HWM PEI the current at positive voltages is higher than at negative voltages. This is indicative of a positively charged pore. When the pore is modified with PAAMA, the opposite is true. The PAAMA introduces carboxyl groups onto the pore wall which DNA can be covalently attached.

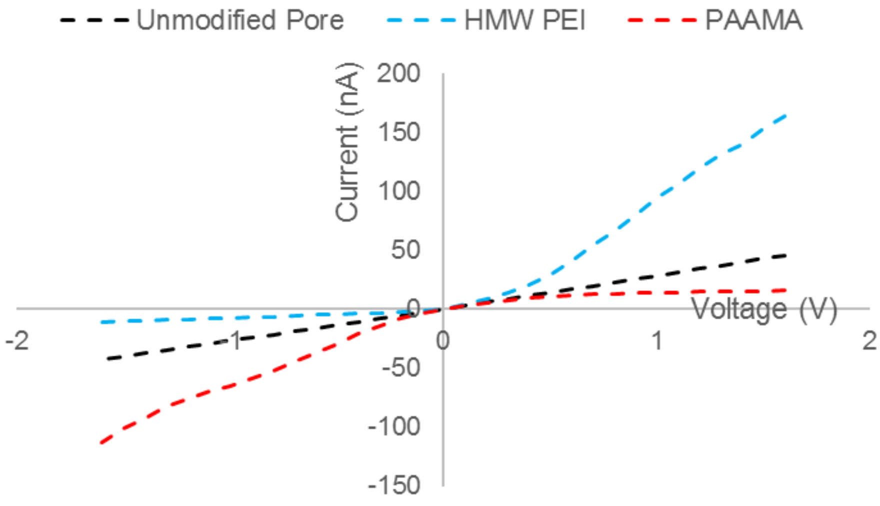

Figure 7.8 Current – Voltage (I-V) curves showing the rectification of the nanopore modified with high molecular weight PEI and PAAMA. Recorded in 20 mM KCl.

The rectification of the pore changes when DNA is attached to the pore wall surface, this is used to confirm the presence of the DNA aptamer, Figure 7.9. The aptamer used is the dual aptamer which can bind both Pb^{2+} and Hg^{2+}. Table 7.2 shows how the ratios between the – voltage and + voltage changes as the pore surface is modified.

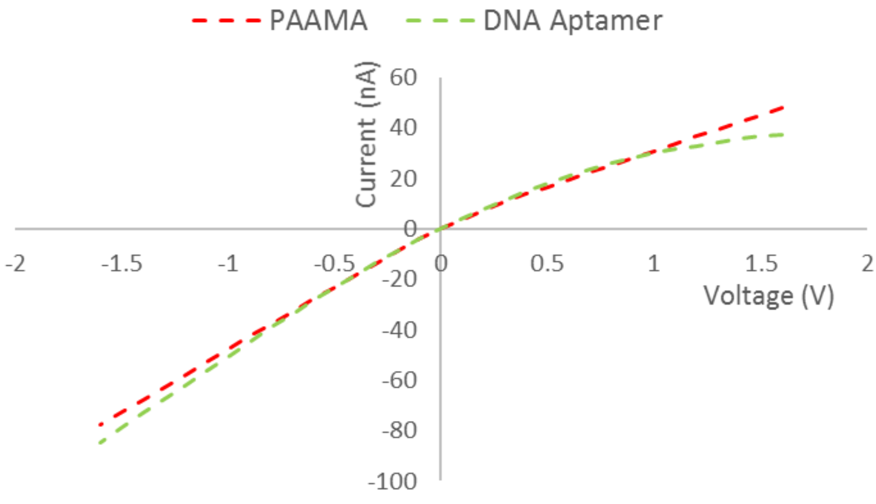

Figure 7.9 Current – Voltage (I-V) curves showing the rectification of the nanopore modified with PAAMA and DNA. Recorded in 20 mM KCl.

Table 7.2 Rectification ratios for a nanopore modified with HMW PEI, PAAMA and DNA measured in different NaCl ionic strengths.

	20 mM	100 mM	500 mM
Unmodified Pore	1.46983	1.14793	1.01911
PEI	0.30239	0.69733	0.97775
PAAMA	1.62213	1.25158	1.00643
DNA	2.261333	1.29366	1.27675

To analyse the rectification behaviour of the nanopore when the analyte binds, rectification ratios are used. The rectification ratio is measured at +/- 1.60 V and is the ratio between the current recorded at a negative voltage compared to the current at the positive voltage. The pores were incubated with different concentrations of a single ion i.e. either Pb^{2+} or Hg^{2+}. Figure 7.10 shows the rectification ratios of pores incubated with varying metal ion concentrations. The rectification reduces as the metal ion concentration increases, this is due to the positively charged metal ions binding to the DNA and altering the flow of current through the nanopore. It is interesting to note that the Hg^{2+} changes the rectification of the pore, Figure 7.10a, but could not be detected on the particles surface. The Pb^{2+} binding to the DNA also changes the rectification behaviour of the pore, Figure 7.10b. The modification of the pore can be used to detect ions either held closely to the surface or further away.

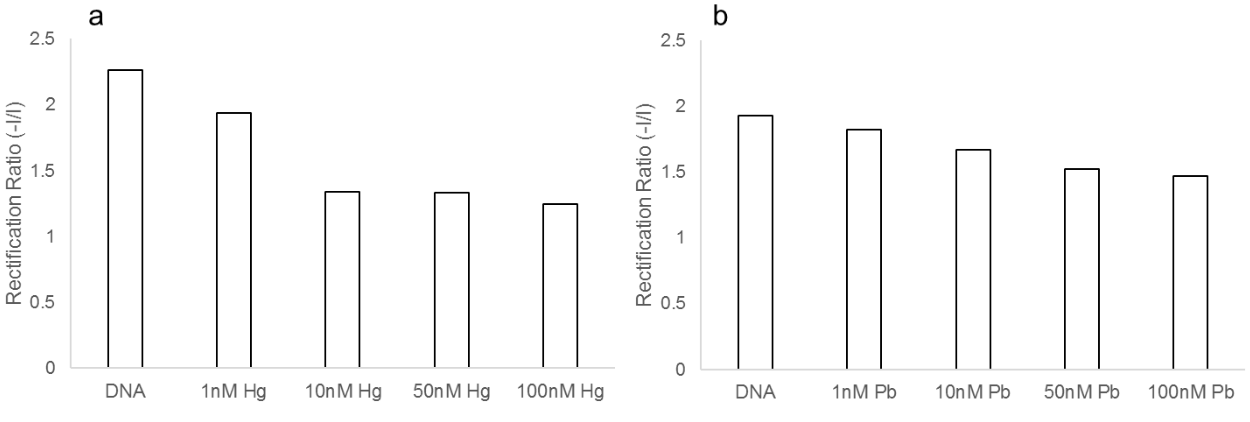

Figure 7.10 Rectification ratios of pores incubated with (a) mercury and (b) lead, n=1. Measured in 20 mM NaCl.

To show that the dual aptamer responds to both metals simultaneously, a pore was incubated with Hg^{2+} ions (10 nM) followed by Pb^{2+} ions (10 nM), Figure 7.11a. The current was recorded in between each metal ion. On a second pore Pb^{2+} ions were incubated first and then followed by Hg^{2+} ions, Figure 7.11b. Figure 7.11 shows that the rectification ratio of each pore is reduced when dosed with the two different metal ions. The separate binding sites on the DNA aptamer both give a change in current response.

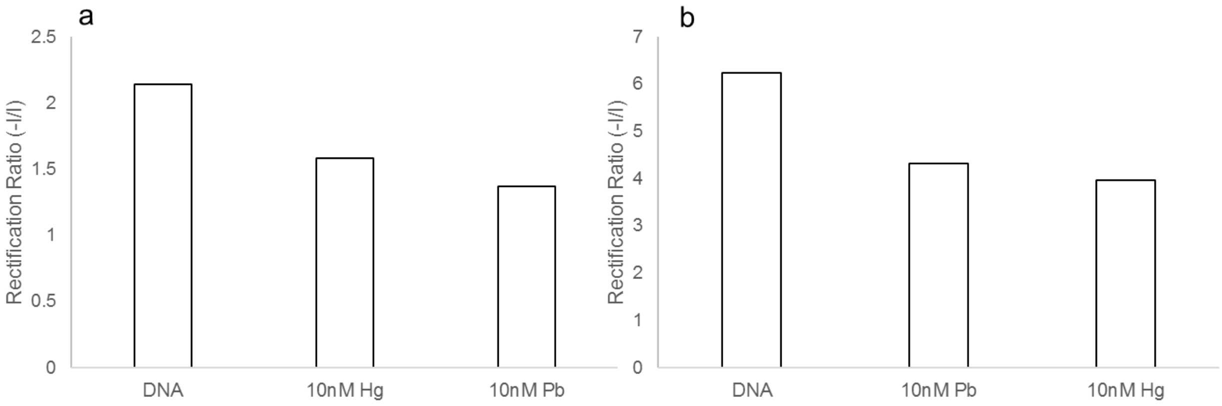

Figure 7.11 Rectification ratios of pores incubated with (a) mercury followed by lead and (b) lead followed by mercury, n=1. Measured in 20 mM NaCl.

A pore modified with the dual aptamer was incubated with increasing levels of metal ions. The pore was firstly dosed with 1 nM Pb^{2+}, followed by 1 nM Hg^{2+} and the process was repeated. In between each metal ion incubation, the rectification of the pore was measured. The rectification ratio of the pore decreased with each addition of metal ion, Figure 7.12.

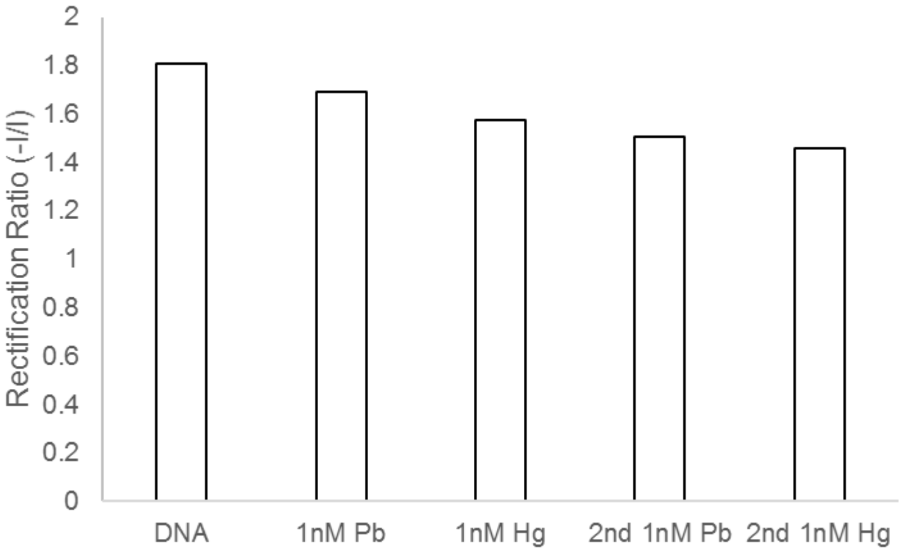

Figure 7.12 Rectification ratios of a pore incubated with increasing amounts of metal ions, n=1. Measured in 20 mM NaCl.

7.5 Conclusions

In summary, this chapter presents work on the dual detection of lead and mercury ions. An aptamer was designed by combining two aptamers and the dual aptamer could bind both lead and mercury. The work compares two different approaches to analyte detection using TRPS. One method utilises the traditional particle assay and the other uses the flow of ions through the nanopore. The experiments with particles modified with a dual aptamer suggest that the particles are sensitive only to ions that bind to the outer aptamer. This observation is both interesting and potentially harmful for RPS sensors, as it suggests that changes to the aptamer structure close to the beads surfaces maybe have little effect on the relative particle velocity. Modifying the pore with DNA resulted in a more sensitive response towards the metal ion binding to the inner aptamer. Further work would need to be carried out to ascertain if a pore-based approach could work when a particle-based assay does not. The reasons behind the differences between a particle and pore assay would need to be explored further by modelling the current flow through the modified pore.

Experiments presented here were performed with magnetic particles, so that in future the process can be automated, allowing the sample to be extracted and analysed with minimum user interaction. This work could lead to the development of new DNA based sensors using nanopores to detect multiple analytes simultaneously.

7.6 References

1. Sigel, R. K. O. & Sigel, H. A stability concept for metal ion coordination to single-stranded nucleic acids and affinities of individual sites. *Acc. Chem. Res.* **43,** 974–984 (2010).

2. Sigel, H. Interactions of Metal Ions with Nucleotides and Nucleic Acids and their Constituents. *Chem. Soc. Rev.* 255–267 (1993).

3. Sigel, H. & Griesser, R. Nucleoside 5′-triphosphates: self-association, acid–base, and metal ion-binding properties in solution. *Chem. Soc. Rev.* **34,** 875 (2005).

4. Navarro, J. a. R. & Lippert, B. Molecular architecture with metal ions, nucleobases and other heterocycles. *Coord. Chem. Rev.* **185–186,** 653–667 (1999).

5. Freisinger, E. & Sigel, R. K. O. From nucleotides to ribozymes-A comparison of their metal ion binding properties. *Coord. Chem. Rev.* **251,** 1834–1851 (2007).

6. Santoro, S. W., Joyce, G. F., Sakthivel, K., Gramatikova, S. & Barbas, C. F. RNA cleavage by a DNA enzyme with extended chemical functionality. *J. Am. Chem. Soc.* **122,** 2433–2439 (2000).

7. Ono, A. & Togashi, H. Highly selective oligonucleotide-based sensor for mercury(II) in aqueous solutions. *Angew. Chemie - Int. Ed.* **43,** 4300–4302 (2004).

8. Smirnov, I. V., Kotch, F. W., Pickering, I. J., Davis, J. T. & Shafer, R. H. Pb EXAFS studies on DNA quadruplexes: Identification of metal ion binding site. *Biochemistry* **41,** 12133–12139 (2002).

9. Blundell, E. L. C. J., Vogel, R. & Platt, M. Particle-by-Particle Charge Analysis of DNA-Modified Nanoparticles Using Tunable Resistive Pulse Sensing. *Langmuir* **32,** 1082–1090 (2016).

10. Miyake, Y. *et al.* Mercury(II)-mediated formation of thymine-Hg(II)-thymine base pairs in DNA duplexes. *J. Am. Chem. Soc.* **128,** 2172–2173 (2006).

11. Platt, M., Rowe, W., Knowles, J., Day, P. J. & Kell, D. B. Analysis of aptamer sequence activity relationships. *Integr. Biol.* **1,** 116–122 (2009).

12. Blundell, E. L. C. J., Mayne, L. J., Christie, S. D. R. & Platt, M. Protein Detection Using Tunable Pores: Resistive Pulses and Current Rectification. *Faraday Discuss.* **193,** 487–505 (2016).

8 Conclusions

The work presented in this thesis aims to provide new metal ion sensors using tunable resistive pulse sensing (TRPS). Several methods were developed to meet this aim using a combination of modified nanoparticles, tunable pores and modified pore surfaces with dual recognition built in. The particle translocation velocity is used to study the changes on the nanoparticle surface and was used successfully to detect metal ions using different ligands for different metals. The method was shown to work over a large range of ionic strengths and pH. The ability to multiplex the method has been presented in this thesis, which enabled more than one metal ion to be detected simultaneously.

Chapter 3 applies the double layer theory to measuring charge on the surface of a particles surface via particle velocity through the nanopore. The presented results show how ionic strength and pH can be tuned to alter the particle's velocity. Silica nanoparticles and carboxyl coated nanoparticles velocities were shown to increase by reducing the ionic strength. Upon having their surfaces modified the resulting particle velocities differed and this signal can be used to confirm a successful modification. The silica nanoparticles and APTES modified particles were easily distinguished due to the polarity in which the particles traversed the pore. Carboxyl and DNA modified particles were then distinguished by an increase in velocity upon DNA being attached to the particles surface. The particles in this chapter have functional groups, -COOH and $–NH_2$, that can be protonated/deprotonated. Understanding how the double layer changes with ionic strength and pH was an essential step in designing a metal ion sensor based on the velocity of the particle through the pore.

Chapter 4 builds on the work presented in Chapter 3 and applies the theory to detecting a metal ion on the surface of a nanoparticle. Copper (II) was chosen along with a complementary ligand that had been studied previously. Changes in particle velocity through the nanopore allows for detection of copper (II) as low as 1 ppm and at 10 ppm with competing metal ions present. Altering the ionic strength in which the particles were analysed, resulted in a change in waveshape. The biphasic pulse behaviour exhibited in low ionic strengths and this provided complimentary measurements to the particle velocity. At low ionic strengths, the magnitude of changes seen in particle velocity between samples with and without copper (II) was larger. However, running samples in low ionic strengths proved difficult. The baseline was often unstable and therefore difficult to get a suitable particle count within 5 minutes. The electrolyte concentration would need to be chosen to provide a suitable particle count but without compromising on the detection of the metal ion.

Chapter 5 differs from the previous chapters, a pore-based assay is presented using a protein as the analyte. Using ionic current rectification, the flow of current through the pore allows changes in charge on the nanopore to be detected. By modifying the pore wall with a DNA aptamer, the binding of the protein was detected. This method was later used for a metal ion assay. The method could be developed further by controlling the modification of the pore wall so specific binding sites could be incorporated for a variety of analytes. One downfall of using a pore-based assay is the pore to pore differences. Due to the production method for the pores, difference in size and shape can occur and this will give rise to different rectification properties. It is acknowledged that further studies are required to access the effects of the modification of the top surface of the pore has on the rectification mechanism.

Chapters 6 and 7, focus on the simultaneous detection of mercury (II) and lead (II). Often more than one contaminant are present in solution making multiplexed detection desirable. The chapters build of techniques using in Chapters 3, 4 and 5 and compare the use of a particle-based assay with a pore-based assay. Chapter 6 demonstrates the use of two different particle sizes, each modified with a different DNA aptamer to detect to two different metal ions. But a typical RPS device will have an upper limit to the number of particles that can be run simultaneously. This is dependent upon the pore size and ability to produce uniform beads within the pores sensing range. Another multiplex assay was explored and the DNA aptamers are combined into on single-stranded DNA aptamer containing two different binding sites. The chapter compares two different approaches to analyte detection using TRPS. One method utilises the traditional particle assay and the other uses the flow of ions through the nanopore. The experiments with particles modified with a dual aptamer suggest that the particles are sensitive only to ions that bind to the outer aptamer. This observation is both interesting and potentially harmful for RPS sensors, as it suggests that changes to the aptamer structure close to the beads surfaces maybe have little effect on the relative particle velocity. Modifying the pore with DNA resulted in a more sensitive response towards the metal ion binding to the inner aptamer.

The experiments presented in this thesis demonstrate how TRPS can be successfully used to detect changes in charge on a nanoparticles surface by studying the particles velocity through the pore. Several assays were performed using TRPS and different particle modifications to detect a variety of metal ions in solution and the work explored the differences between particle and pore-based assays. The method chosen can easily be applied to a variety of different metal ions by controlling the surface modification on the nanopore.

8.1 Future work

This work provides proof-of-concept that TRPS can be successfully used to detect metal ions in solution, however there is still work which would needed to be completed before any of the methods can be used in the field.

Materials and procedures need to be standardised to enable the expansion of this work. Within this thesis, a few different types of particles have been used, Chapters 3 and 4 uses silica nanoparticles while Chapters 6 and 7 use carboxyl coated magnetic particles. These differences lead to different modification procedures, each with different preparation steps. If the particles were to be used in environmental monitoring, reducing the number of preparation steps would be beneficial in reducing preparation time and cost. Further work would also need to be carried out when designing the particle modification which would be used to bind the metal ions in solution. Further considerations would need to be given to the ligands used, ensuring they are highly selective and specific to the chosen metal ion. Controlling the modification process could lead to lower limits of detection, the velocity of a particle may be more sensitive to changes if there was a lower coverage of binding sites on the particles surface.

Chapters 6 and 7 presented proof-of-concept work for multiplexed sensing. Detection of multiple metals simultaneously is favourable, often there is more than one analyte of interest present in a sample. Multiplexed detection will reduce the number of experiments which would need to be performed. A typical RPS device will have an upper limit to the number of particles that can be run simultaneously and work needs to be undertaken to determine how many analytes TRPS can detect simultaneously. This could be done by changing not only the size of the particle but exploring different shapes such as rods.

Perhaps the most fundamental challenge of this work is understanding the changes of surface charge density on the nanoparticles surface. The changes on the nanoparticle surface is the key to the detection of the metal ion, understanding these changes will help develop more sensitive methods for detection. Chapter 7 highlights differences between a pore-based and particle-based assay and further work would need to be carried out to ascertain if a pore-based approach could work when a particle-based assay does not. The reasons behind the differences between a particle and pore assay would need to be explored further by modelling the current flow through the modified pore.

A final consideration would need to be given to the sample matrix. Work in this thesis was carried out in simple electrolytes with little interferences. However, environmental and biological samples will contain a lot of competing metals ions, suspended solids and organic matter which could interfere with the sample measurement and potentially block the nanopore. A considerable amount of work would need to be undertaken to develop the method to detect analytes in environmental and biological samples which may involve more preparation steps to make the sample suitable to run on TRPS.